**Università degli Studi di Napoli Federico II**

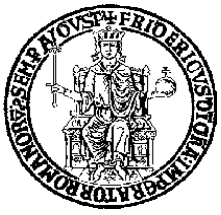

**Facoltà di Ingegneria**

TESI DI DOTTORATO IN INGEGNERIA DEI MATERIALI E DELLE STRUTTURE

XXVI CICLO

# *Toward the manipulation of multiphase materials for nanobiotechnology applications in touch-less modality: a pyrofluidic platform*


Coordinatore

Prof. Giuseppe Mensitieri

Candidata

Sara Coppola


ANNO ACCADEMICO 2013/2014

## **Contents**:

## Introduction

The work and the experiments reported in this thesis are related to the description of an unusual and smart way for the manipulation of liquid and polymeric materials. In fact, the term "pyro-fluidic platform" would express the ability of working on fluids (liquid and/or polymer) exploiting the pyro-electric effect activated onto a ferroelectric crystal. In the following chapters it is reported a detailed description of how is possible manipulate liquid and polymeric materials in non-contact mode through an electrode-free approach by simply using the pyro-electric effect. In every chapter the theoretical and experimental analysis are combined with the description of their technological applications.

In particular, in *chapter 1* it is described and characterized the no-contact self-assembling of liquids in plane (1D), using a micro engineered crystal and, additional studies regarding the fabrication of polymeric microlenses are added. Microlenses are key components for optical devices and are widely applied in several application fields, such as communications, three-dimensional displays, optical data storage and photodetectors, playing a fundamental role in many optical systems. Through the pyro-electric properties of the platform the microlenses fabrication appears to be very simple and direct. Furthermore, additional experiments of functionalization are proposed for the manipulation of Liquid Crystals (LCs) as a function of the pyro-electric field. The major attractive feature of LCs lies in the fact that their optical properties can be modulated by electric, optical, or magnetic fields and in the recent years they have experienced a rapid growth in many fields, ranging from display systems as well as in optics and photonics.

The possibility of handling liquid and dispensing smart material is addressed in *chapter 2*. Techniques for printing patterns with inorganic, organic and biological inks at high resolution represent one of the major point of interest in different fields of technology from experimental to industrial applications. In this chapter a new concept of droplet generation based on the pyroelectrohydrodynamic effect is described. The method is analyzed for the direct drawing and dispensing of small droplets from liquid drops or film reservoirs. For the smallest ink droplets, printing resolution down to 300 nm (corresponding to attolitre volumes) is achieved greatly exceeding the possibilities provided by conventional inkjet methods.

This technique does not require electrodes, high-voltage circuit connections or special capillary nozzles and could be applied also in case of high viscous materials such as polymers. In fact, the approach studied in *chapter 3* exploits instabilities and self-assembling of polymeric liquids for fabricating single or arrays of complex high aspect-ratio 3D microstructures. Liquid instabilities are first driven via electro-hydrodynamic pressure and then quickly cured to obtain

permanent 3D micro-structures, by the same thermal treatment, paving the way to a previously undescribed paradigm in the fabrication of 3D polymer microstructures. In the experiment reported in the chapter the fabrication of polymer micro-structures as stretchable tunable microresonator for detecting or sensing applications is reported. An additional description of potential use of polymer 'axicons' (conical structures with a needle tip at their apex) as elements for optical tweezers with a large depth of focus is also provided.

The two final chapters are focused on the application of the pyro-electric platform in case of biomaterials. In particular, in *chapter 4* a new method is described for processing biomaterials (biocompatible and biodegradable) in order to fabricate scaffold for tissue engineering application. In this specific field, the use of biopolymers is very useful because of their inherent biodegradability, biocompatibility and biofunctionality. In this chapter an unconventional but very simple approach based on the pyro-electric effect for fiber spinning is explained and experiments regarding the direct fabrication of 2D full-ordered patterns are described avoiding the typical spiraling effect of conventional electro-spinning. Moreover, an additional applications of the proposed technology for controlling cell adhesion and contact guidance is investigated.

In *chapter 5* it is studied and described an additional property of the pyro-platform as an electro-drawing approach for the fabrication of sharp, dissolving microneedles directly from a liquid polymer reservoir, in a moulding-free and contact-free modality. Model drugs can be embedded at room temperature in drop reservoirs, drawn to form microneedles at no more than 40 °C and successfully delivered via indentation into the skin. In principle, nanoparticles of hydrogel could be previously dispersed in the polymer solution thus creating hydrophilic compartments and controlling the microneedle biodegradation kinetics. Microneedle patches are formed directly onto a flexible, overcoming the technological limitations of both micro-casting and drawing lithography and opening new frontiers in the field of transdermal delivery. Along the following chapters the versatility and the wide variety of applications for the pyroelectric platform are described. The simplicity afforded by the absence of nozzles, electrodes or high-voltage power supplies, and the potential for smart material manipulation make the method very attractive for many applications in different fields ranging from photonics to biology.

# Chapter 1

## 1.1 Wettability patterning by pyroelectric effect

The wettability of lithium niobate crystals is patterned by inducing the pyroelectric effect onto domain engineered samples. Compared to conventional electro-wetting (EW) experiments, this technique allows one to obtain wettability patterning by an electrode-less configuration. In fact, the surface charges inducing the effect are generated pyroelectrically and spatially modulated by the domain grating. The wettability patterning of solid surfaces is important for different applications. Recently, efficient self-assembly and alignment of metallic nano-rods dispersed in water have been obtained by using surfaces with patterned wettability[1]. Moreover the development of integrated microfluidic and optofluidic systems points out the importance of liquid actuation[2-4]. Physical phenomena, such as dielectrophoresis[5] or electro-osmosis[6], were investigated to handle liquids at small scales. EW allows alteration of the wetting properties of a substrate by means of free electrical charges[7,8]. Wettability patterning induced by surface potential modification[9] or local wettability modification by nanolithography has been demonstrated[10]. In addition EW is a key technology for realizing liquid lenses[11,12]. Usually, the EW based experiments need complex electrode geometries to actuate and control surface wettability. Therefore, the possibility of patterning the wettability of solid surfaces by activating specific properties of the material without using external electrodes is desirable. In this section it is shown that by means of functionalization of LiNbO3 substrates it is possible to pattern and control its wettability. Activation of the pyroelectric effect[13,14] into periodically poled LN (PPLN) substrates allows one to pattern and control the surface wettability. The technique can generate an array of sessile droplets according to the reversed domain structure of the LN substrate.

LN is a rhombohedral crystal that shows pyroelectricity at room temperature. The spontaneous polarization $P_s$ changes according to $\Delta P_i = \xi_i \cdot \Delta T$ , where $\xi_i$ is the pyroelectric coefficient and $\Delta T$ is the temperature variation. At equilibrium, all $P_s$ in the crystal are fully screened by the external screening charge and no electric field exists[15]. The polarization change perturbs such equilibrium causing a lack or excess of surface charge, thus generating a high electric field[16]. The spontaneous polarization, ($Ps=78\ \mu C/cm^2$) of LN is inverted by photolithography and electric field poling[17,18] in order to obtain a periodic square array of hexagonal reversed domains.

PPLN fabrication is achieved at room temperature by an electric field poling process. A positive voltage pulse slightly exceeding the coercive field of LN (~21kV/mm) is applied on

the z+ patterned crystal face by using a liquid electrolyte consisting of LiCl in deionized water. The liquid electrode configuration has two electrolyte containing chambers which squeeze the sample between two O-ring gaskets, as shown schematically in **Figure 1.1**.

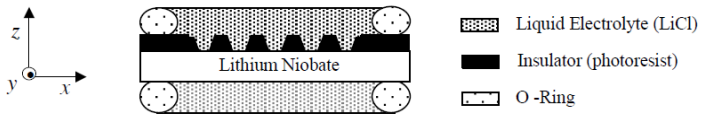


**Figure 1.1**: Cross-sectional view of the electrode configuration for electric field poling. The photoresist grating acts as an insulating barrier that lowers the electric field applied through the liquid electrolyte below the coercive field needed to reverse the spontaneous polarization.

**Figure 1.2** illustrates the external electrical circuit. A conventional Signal Generator (SG) drives an High Voltage Amplifier (HVA - 2000x), provided by Trek, Inc., with a series current limiting resistor, RS = 50MΩ , in order to get a 12kV positive voltage. A diode rectifier D is connected to the output of the HVA to prevent flowing of backswitch current in the circuit. It is well known[19] that, in LN, the reversed domains typically grow beyond the width of the electrodes as the result of the remaining fringing fields along the edges of the lithographic grating strips. The strategy for optimal domain patterning, with conventional electric field poling, is to stop the voltage pulse before poling progresses under the photoresist layer. An in situ method which can be used as a stopping criterion consists in watching for a drop in the poling current Ipol and a corresponding rise in the poling voltage Vpol, both effects indicating that the sample has completely poled under the electrodes and the domains are now laterally spreading under the insulating layer[19,20]. In fact, the conductivity of LN at room temperature is low enough that the poling current can be monitored readily by measuring the voltage drop across the resistance Rm = 10kΩ while a conventional High Voltage Probe (HVP) is used to measure the poling voltage Vpol across the sample. Both current and voltage waveforms are visualized on the oscilloscope Osc during the poling process.

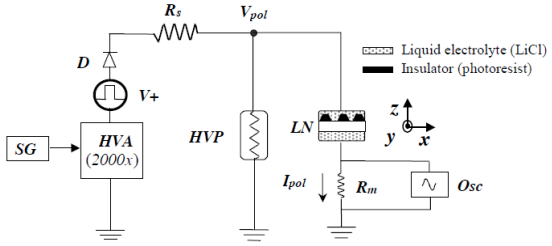


**Figure 1.2**: Electrical circuit used to pole LN samples. An High Voltage Amplifier (HVA - 2000x) with a series resistor RS = 50MΩ produces +12kV voltage by using a conventional Signal Generator (SG). A diode rectifier D was connected to the output of the HVA to prevent flowing of backswitch current.

In case of sample preparation for the experiment described in the following both sides polished and 500 μm thick LN crystals (from Crystal Technology, Inc.) were subject to standard electric field poling[18] in order to achieve a square array of hexagonal reversed domains. The samples were first resist patterned (photoresist Shipley S1813-J2, around 1.3 μm thick) by conventional mask lithography in order to achieve a square array of circular resist openings. The subsequent application of high voltage pulses, exceeding the coercive field of the material (around 21 kV/mm), allowed to fabricate the periodic domain reversed sample. The period of the structure was around 200 μm along both x and y crystal axis direction. **Figure 1.3** shows the optical microscope image of the PPLN samples fabricated by the electric field poling and used for the described experiments.

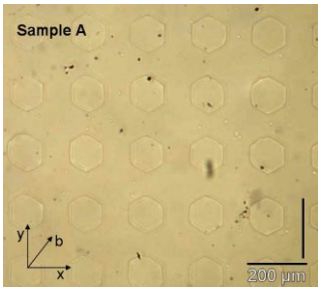


**Figure 1.3**: Optical microscope image of a PPLN sample with a square array of reversed domains. The period of the structures is around 200 μm.

When the PPLN crystal is subjected to a temperature variation, the change of the polarization of the crystal perturbs its equilibrium, causing a lack or excess of surface screening charge. Consequently, an electrostatic state appears and generates a high electric field at the crystal surface[16,21]. **Figure 1.4**(a)-(b) show the schematic view of the PPLN sample cross section with the charge distribution occurring at the equilibrium state and in case of heating/cooling treatment, respectively. The arrows indicate the orientation of the ferroelectric domains.

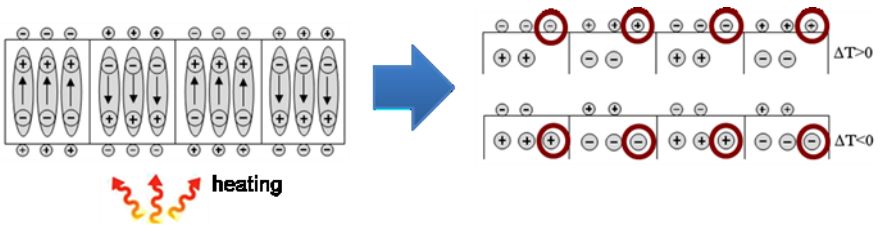


(a) (b)

**Figure 1.4**: Schematic view of the PPLN sample cross section with the charge distribution exhibited (a) at the equilibrium state; (b) in case of heating (top) and (bottom) cooling process.

According to the pyroelectric effect[15] the heating process makes the polarization magnitude to decrease, thus leaving surface screening charges uncompensated (see Figure 1.4(b) top). These generate a net electric charge distribution depending on the inverted domain structure, with positive and negative sign onto the reversed and un-reversed domain regions, respectively. Essentially, the wettability can be assumed as locally changed at the solid-liquid interface due to the presence of the electric forces. In case of a liquid deposited over the crystal the wave-like profile of the liquid is the result of the equilibrium condition between the surface tension and those electric forces. In fact, the presence of the net electric charge onto the crystal surface, generated pyroelectrically, makes the surface tension to decrease due to the repulsion between like charges, which tends to expand the surface area of the liquid[22]. Therefore, the work done by the charges produces a hydrostatic pressure towards hexagon centers thus leading to the formation of isolated droplets. In fact, the charges across the domain walls are opposite in sign and produce a severe interface tension which leads the liquid film to break into separate droplets.

## 1.2 The pyro-eletric effect onto a PPLN crystal

According to the pyroelectric effect the heating process makes the polarization magnitude decrease, thus leaving surface screening charges uncompensated (Figure 1.4(b) top). These generate a net electric charge distribution depending on the inverted domain structure, with positive and negative sign on the reversed and un-reversed domain regions, respectively. The screening charges in excess, continuously produced during the heating process, are no more attracted by the polarization charge and consequently are free to diffuse on the surface of the ferroelectric substrate LN. An electric field template arises following the geometry of the reversed domains.

Simulations of the electric field distribution generated pyroelectrically onto the surface of a PPLN crystal have been performed by finite element based calculations (COMSOL Multiphysics 4.3). Using the electrostatic model in a stationary condition and according to Gauss' law for the numerical simulation was adopted the charge conservation equation:

$$\nabla \cdot D = \rho_v(r)$$

where D is the PEF vector and $\rho_v$ is local volume charge density.

Under static conditions the electric potential E can be correlated to the electric potential V by the relationship:

$$E = \nabla \cdot V$$

The remnant electric displacement constitutive relation was selected to simulate the dielectric constant anisotropy and the pyroelectric behavior of LN:

$$D = \varepsilon_0 \varepsilon_r \cdot E + D_r$$

$$\varepsilon_r = \begin{bmatrix} \varepsilon_{xx} & 0 & 0 \\ 0 & \varepsilon_{yy} & 0 \\ 0 & 0 & \varepsilon_{zz} \end{bmatrix}$$

here $\varepsilon_0$ is the vacuum dielectric constant, $\varepsilon_r$ is the relative permittivity matrix, E is the electric field vector and $D_r$ is the residue electric displacement (RED). The electric field dependence from temperature is obtained thanks to the $D_r$ vector, expressed by the relation:

$$D_z = \begin{bmatrix} 0 \\ 0 \\ p_z \end{bmatrix} \quad \nabla T = \begin{bmatrix} 0 \\ 0 \\ p_z \end{bmatrix} \left(T - T_0\right)$$

$$p_z = -4 \times 10^{-5} \left[ \frac{C}{Km^2} \right]$$

where $p_z$ is the pyroelectric constant for LN, T is the local temperature of the material and $T_0$ is the zero polarization condition temperature.

In **Figure 1.5 (a)** is presented the geometry defined for the study. The geometry was shaped adopting a 3D model for the LN crystal ($\varepsilon_r$=84). The z-cut LN crystal showed a periodic pattern of hexagonal parallelepiped inverted domains. Regarding the boundary conditions, the bottom side of the system (LN) is maintained at 393 K and the top side (air) at 293 K. All of the other boundaries are thermally isolated. As electrical conditions all the boundaries of the system are considered as zero charged sides. The geometrical poling of the LN substrate is implemented in the simulation setting $p_z$ as a positive scalar in red zones and negative in blue zones. From this arise a +q and a -q volume charge density in the two different domains. Moreover, each pair of opposite side faces were imposed as continuity interfaces in periodic boundary conditions to simulate an infinite extension of the crystal. The results of the simulations are depicted in **Figure 1.5(b)–(d)** where the calculated electric field lines are shown. The electric field distribution is periodic and follows the geometry of the square array of hexagonal domains. Maximum values of the electric field were in proximity of the domain walls of the hexagons.

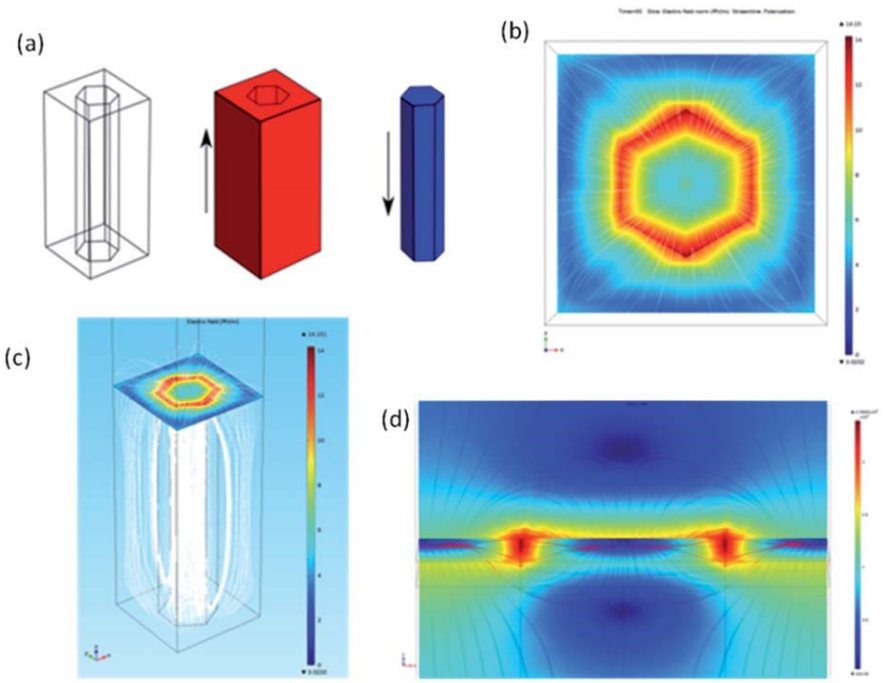


**Figure 1.5**: (a) Geometry of the hexagonal parallelepiped inverted domains; (b) plot of the pyroelectric potential (upper view); (c) plot ofnumerical electric field stream lines under the action of the pyroelectric field (lateral view) and (d) side view.

## 1.3 Manipulation of polymer materials for patterning micro lenses

Using the pyro-electric effect activated onto a PPLN crystal it would be possible to manipulate liquid and polymeric materials in non-contact mode through an electrode-free approach. In particular in this section the fabrication of polymeric microlenses is described and characterized.

Microlenses are key components for optical devices and are widely applied in several application fields, such as communications, three-dimensional displays, optical data storage and photodetectors, playing a fundamental role in many optical systems. Numerous classes of microlenses exist, depending on the embedding technology and the specific applications. At now, microlenses with variable focusing have been obtained by actuation of liquid crystals or other liquids through electro-wetting, electrophoresis or hydrodynamic pressure[23,24]. On the other hand, a large variety of fabrication processes have been developed for plastic/polymer based microlenses[25,26], such as embossing[27], soft-lithography[28], micro-molding[29], photolithography[30], electron beam lithography[31] reactive ion etching[32], laser assisted technique[28] and printing techniques[33,34]. In particular, these last techniques were advised as

direct methods for high-quality and high-precision processes making the fabrication short time-consuming and cost-effective. In this way, polymeric materials such as poly(methyl methacrylate) PMMA[35] or Polydimethylsiloxane PDMS[36] have been extensively investigated. PDMS is specifically suitable because of its good optical quality and the simplicity of the lense fabrication process known as 'soft lithography'. In soft lithography, it is only necessary to have a mould to obtain a negative replica of the structure[37-40]. It is important to note that lenses made with polymeric materials like PDMS can also be tuned thanks to the inherent elastic properties of the material. In fact, it has been demonstrated that a single PDMS microlens can be actuated and tuned thermically[41]. Furthermore, microlens arrays can change their focusing properties when subjected to lateral strain[42].

The ability to pattern PDMS reliably in the form of both thick substrates and thin membranes or films is critical to expanding the scope of its applications, especially in the fields of microfluidics and bioengineering. The PDMS material offers many advantages. It is optically transparent, electrically insulating, mechanically elastic, and gas permeable. PDMS is also biocompatible[43], thus finding application in the field of bioengineering where the position of cells on a substrate is important for different purposes. These include biosensor fabrication for drug toxicity and environmental monitoring[44], tissue engineering[45], patterning of active proteins[46] and basic biology studies where the role of cell adhesion, shape, proliferation, and differentiation are studied as a function of cell–cell and cell–extracellular matrix interactions[47]. In this section we propose a different approach for direct PDMS patterning. A lithography-based technique for realizing periodic patterning of thin-film PDMS structures onto lithium niobate (LN) substrates is presented and discussed. The PDMS film is microstructured according to the wettability variation of the LN substrate induced by the pyroelectric effect. The appropriate thermal treatment applied to the crystal induces the polymerization of the PDMS film, leading to a stable and reliable PDMS pattern. The wettability patterning and its periodicity is achieved by the exploitation of the periodic reversed domains fabricated in congruent z-cut LN wafers.

The screening charges in excess, continuously produced during the heating process, are no more attracted by the polarization charge and consequently are free to diffuse into the PDMS film.

The lens-like array topography exhibited by the PDMS film can be considered as the result of the equilibrium condition between the surface tensions and the electric forces related to the charge redistribution on the substrate. **Figure 1.6** shows schematically the process steps implemented for the direct patterning of PDMS films. A layer of PDMS prepolymer solution

(Dow Corning Sylgard 184, 10:1 mixing ratio base to curing agent) was spin coated over the original z- face of the PPLN substrate at 6000 RPM for 2 min. The PDMS coated sample was then placed onto an hot-plate at a temperature of 170°C for 30s, thus inducing a rapid heating of the sample.

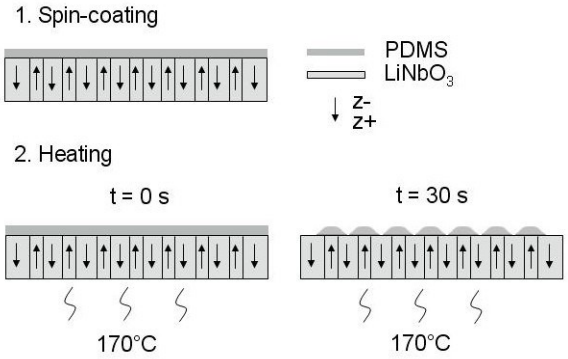


**Figure 1.6**: Schematic view of the process steps.

This self-patterning of PDMS by EW approach could be exploited in several different ways to produce polymeric microlens arrays with different focal lengths, depending on the parameters adopted in the process of functionalization of the substrate. In fact, through this effective lithography-based technique, we obtained PDMS microlens arrays made of thousand of lenses as shown in **Figure 1.7** having micrometric size (100mm of diameter) and focal length in the range of 300-1100 μm.

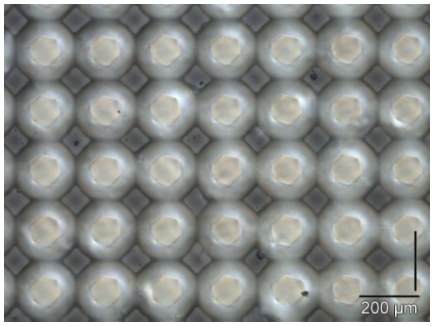


**Figure 1.7**: Optical microscope image of the PDMS microlens array.

Different surface-charge lithography experiments were performed by varying both the temperature and the time length of the thermal treatment and the values at 170°C and 30 s appeared to be the best settings for activating the pyroelectric effect, through the abrupt

temperature increase of the substrate, as well as to insure the cure of the PDMS layer with the modified profile. The PDMS layer assumes a wave-like profile as shown in the schematic 3D and profile views in **Figure 1.8**(a)-(b), as a result of the equilibrium condition between the surface tension and those electric forces.

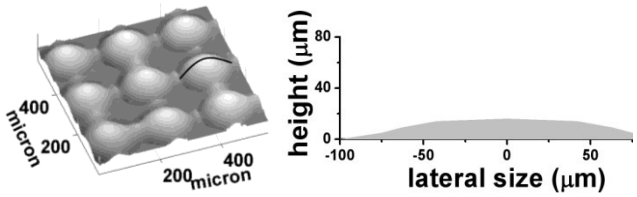


(a) (b)

**Figure 1.8**: Schematic view of (a) the micro-bump array and of (b) the profile along the black line in correspondence of a single micro-bump.

The lithography used for the fabrication appears to exhibit various differences and advantages compared to the conventional PDMS patterning techniques. This method can be considered cost-effective and relatively quick, since no sophisticated process steps, such as atmosphere and pressure control or UV treatment are required by the procedure. In fact, nowadays, standard PPLN crystals are routinely fabricated through relatively cheap processes, while PDMS coating and thermal treatments can be performed by conventional spin-coaters and hot-plates. The PDMS patterns obtained here could be used also as alternative moulds for non-conventional soft lithography applications. The extensive homogeneity of the PPLN crystals available nowadays, and the inherent flexibility in the choice of the desired geometries, makes this technique interesting for applications in the field of biology, such as for cell patterning, where high throughput screens into single integrated microfluidic devices are desirable and the additional chemical patterning of the substrate could be avoided. Moreover, the possibility to pattern PDMS layers directly onto LN substrates could open the way for a variety of applications in microfluidics and biology, where the chemical stability and the specific properties (piezoelectricity; electro-optics; pyroelectricity; nonlinearity; etc.) of the bare LN regions, could be exploited for innovative operational functions. Other possible applications of this technique include microlens arrays and liquid-filled microlens arrays for integrated optical devices. Periodic square arrays of PDMS micro-bumps, with intermediate wells, have been fabricated by an appropriate thermal treatment providing both surface modification and thermal curing of the PDMS layer. This lithographic technique could

be a quick and cheap alternative to the conventional PDMS patterning methods which generally use external forces, load/pressure or sophisticated surface treatments. Potential applications of the technique are in the field of biology and biomedicine for fabricating large areas adhesion/growth site arrays for cells analysis. The same physical principle exploited to fabricate PDMS microlenses on LN substrate could be used to generate an array of liquid micro-lenses. The fabrication of liquid lenses could be even more interesting considering the possibility of realizing tunable lenses. The shape, and thus the focal power of the microfluidic lens, can be changed by varying the hydrostatic pressure of the liquid volume[48,49].

### 1.4 Manipulating Liquid Crystal Droplets onto plymer microlenses

In recent years, liquid crystals (LCs) applications have experienced a rapid growth in many fields, ranging from display systems as well as in optics and photonics[50-54]. The major attractive feature of LCs lies in the fact that their optical properties can be modulated by electric, optical, or magnetic fields. At present, many issues are still open and further developments for manipulating and dynamically control LCs are highly demanding in many emerging fields of technology but also in fundamental research. For example LC tunable lenses have been extensively studied and many successful configurations have been designed and experimentally demonstrated[55-56]. LC based optical devices such as electro-optic switches and beam scanners have been proposed for application in managing radiation and imaging in THz region[57-58]. In many of these proposed devices, the delivering of liquid crystals is accomplished by ink-jet printing methods, but efficient alternatives could be the spatial self-assembly of LC drops. In this section a PPLN crystal coated with polymer microlenes is used for the manipulation of LC droplets. Essentially, a reversible uniform fragmentation of large LC drops has been observed. In fact, driven by the pyroelectric fields obtained by a thermal stimulus applied to the LN substrate, the fragmented drops are self-assembled on the substrate according to the underneath ferroelectric domain patterned structures into LN. Successive coalescence of the fragmented tiny drops is observed on a longer time scale. Reversible character of the whole process has been verified. The aforementioned phenomena are deeply investigated and results of many experiments are shown. When deposited on a hydrophobic (i.e. non-wetting) substrate, a liquid thin film undergoes instability phenomena, mainly driven by inter-molecular forces (e.g. hydrogen bonds or van der Waals forces) and by variations of the surface tension with temperature or liquid composition[59]. The conditions for which these instabilities produce dewetting are governed by the interaction potential of the film, which

describes the effective interaction between the solid-liquid interface and the liquid-air interface[60]. Starting from these assumptions, the behavior of a nematic liquid crystal in contact with a PDMS substrate, subject to a temperature variation has been tested. It has to be said that, due to the PDMS non-full wettability, it is difficult to obtain a LC homogeneous thin layer upon it. Vice versa, the LC arranges itself in drops, with a relatively large contact angle. Thanks to the applied thermal input, a dewetting-like phenomenon occurs. In particular, the thermodynamic instability produces a fragmentation of the big drops into smaller droplets, with the "daughter" drops surrounding the "mother" one.

Experimental measurements are described on four different samples, that we named A,B,C and D, and represented in **Figure 1.9** .

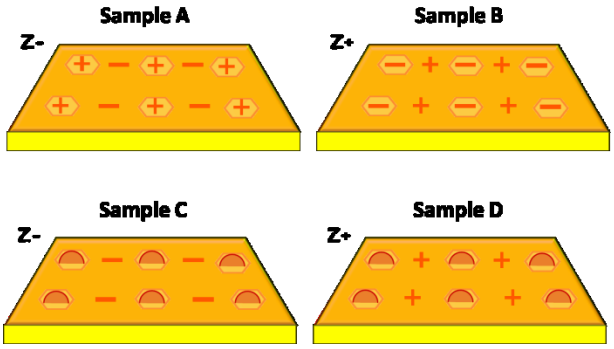


**Figure 1.9**: Sample A: PDMS flat film on PPLN Z- face; sample B: PDMS flat film on PPLN Z + face; Sample C: PDMS microlens array on PPLN Z- face; sample D: PDMS microlens array on PPLN Z + face. The plus and minus represent the signs of the electric charges.

Different samples have been prepared by covering the PPLN samples with thin layers of PDMS (10:1 mixing ratio base to curing agent), spin-coated at 6000 RPM for 2 minutes. Experiments are performed by using both sides of the PPLN samples, Z- and Z + . Samples were coated with thin and uniform layer of PDMS and micro patterned with PDMS microbumps structures, as described in the previous section.

As schematized in Figure 1.9, samples A and B consist of a homogeneous thin layer of PDMS spin-coated on the Z- (A) and Z + (B) face of the LN substrate, while samples C and D are placed onto a hotplate at a temperature of 170 °C for 30s, thus inducing the formation of PDMS microlenses (on Z- and Z + respectively), following the arrangement of the hexagonal domains.

In the following experiments a small quantity of nematic liquid crystal 1-( trans -4-Hexylcyclohexyl)-4-isothiocyanatobenzene[61-62], abbreviated 6CHBT (with phase sequence Cr 12.5 ° C N 43.2 ° C l), from Sigma Aldrich, is placed onto each sample. This LC has been

chosen for the polar structure of the molecule. The sample is, then heated on a hot plate at 90 ° C (above the nematic to isotropic transition temperature) for 30s and then placed at room temperature under an optical microscope in transmission configuration. In the case of a PDMS film spin-coated onto the Z- face of a PPLN substrate (sample A), the starting situation is that of many LC drops (with different dimensions) scattered all over the sample, as in **Figure 1.10**.

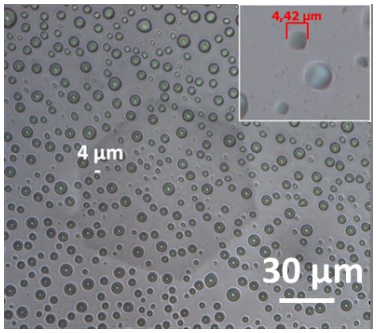


**Figure 1.10** : LC drops scattered on the sample without any geometry, before heating.

On heating the specimen, a quite uniform fragmentation of the LC drops occurs; a high density of smaller droplets covers the whole sample. The behavior of the liquid crystal drops during the cooling step requires some further analysis. Different images were recorded at the microscope during cooling (with a room temperature of 22 ° C) for two hours. **Figures 1.11 (a)-(b)** show two significant pictures from a dynamic recorded sequence, one at the beginning of the cooling process (a) and the second 2 hours later (b).

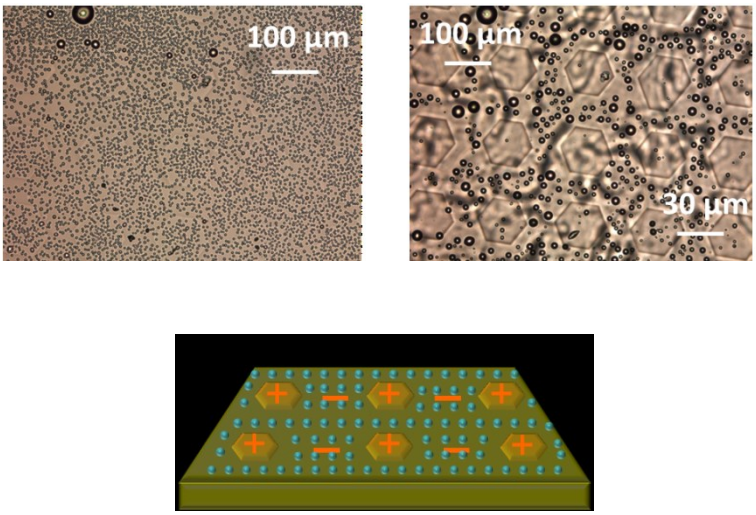


**Figure 1.11**: (a) First frame of fragmented LC droplets suddenly after heating at 90 ° C, much smaller than before heating. LN hexagonal domains are not well visible, covered by the droplets. (b) Frame 2 hours after beginning of cooling and (c) schematic representation.

The first evidence is that almost all of the LC drops move selectively in the areas around the hexagons. The further significant aspect is that the fragmented drops gradually coalesce. After two hours, in fact, the average size of the drops is substantially increased. This phenomenon could be probably ascribed to a reduction of the interfacial tension between nematic LC and PDMS with the decreasing of temperature. Moreover, the process is reversible in the sense that after a (almost long) lapse of time the drops relax and lose their gained self-assembled pattern. **Figure 1.12** shows an image after four days from the start of the cooling process, where the casual re-arrangement of LC drops can be observed. At this point, the sample is re-utilizable, meaning that a new heating would lead to a new fragmentation, a new droplets coalescence and so on.

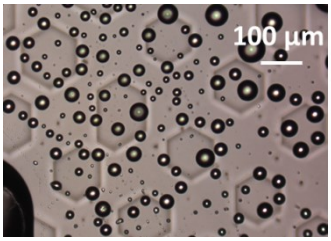


**Figure 1.12**: Coalesced LC drops on the sample after some days at room temperature: the configuration is almost random as before heating.

If the PDMS layer is deposited onto the Z + face of the PPLN crystal (sample B) an opposite behavior is obtained, demonstrating that the phenomena are driven by the sign of the pyroelectric charge. After the fragmentation process the tiny droplets will coalesce again but this time the resulting LC droplets move onto the hexagons and remain trapped there for some hours, as shown in **Figure 1.13**.

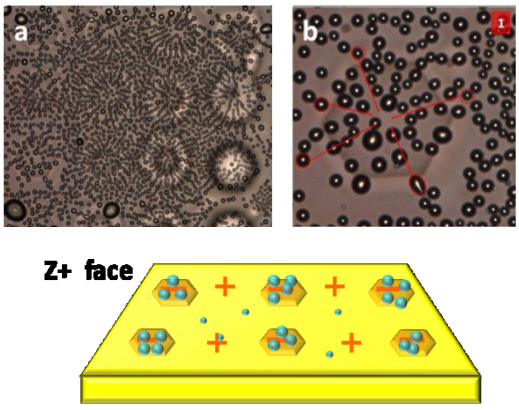


**Figure 1.13**: Experiment performed on sample B. (a) Starting frame when the sample is heated at 90 ° C and then cooled at room temperature for one hour. (b) frame regarding the study of the trajectory of five LC droplets during sample cooling. (c) Scheme of the experiment.

In this case the direction of the LN crystal dipoles is inverted into the hexagons, with respect to the case of sample A (see Figure 1.8 ).

The coalescence of small droplets into bigger ones, while migrating onto the centre of the hexagonal domain can be observed. 19 hours after the beginning of the cooling process, the situation is that of **Figure 1.14(a),** with the coalesced drops still present onto the hexagons. **Figure 1.14(b)** is taken under crossed polarizers, thus putting in evidence the birefringent nature of liquid crystals.

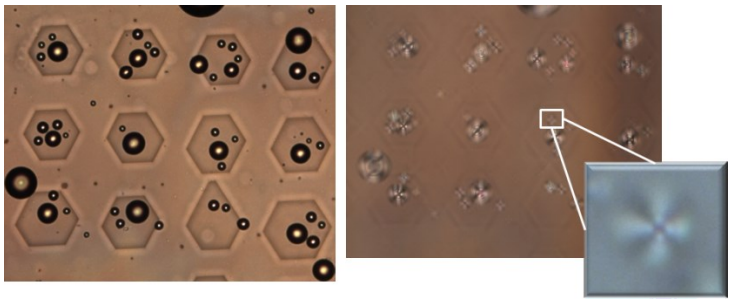

**Figure 1.14**: (a) The sample 19 hours later, at room temperature, and (b) under crossed polarizers: Maltese crosses are well visible.

The phenomenon at the basis of this experimental behavior is the well-known dielectrophoresis, widely described in literature[63-67].

In this case, however, the process is not induced by an external electric field, but it is due to a pyroelectric effect. The advantage of using liquid crystals, in this case, is the birefringent behavior of these materials and their well-known ability to change the polarization of the incident polarized light and, consequently, the huge technological impact they have. Start considering the Z- surface of the crystal and the case $\Delta T < 0$: a cooling situation. As observed before, in this case LC droplets are repulsed by inverted domains (hexagons) and place themselves among them, forming a sort of matrix, as schematized in Figure 11. The LC molecules are repulsed from a positive charged region. Vice versa, if the surface under consideration is Z + , LC droplets are attracted by hexagons (in this case negative regions), as depicted in Figure 1.13. This behavior has to be ascribed to the strong dipole moment of the 6CHBT liquid crystal molecule[61]. In fact, analysis of electrostatic potential distribution shows that the head of the molecule exhibits negative potential, while the edges of the aromatic ring have a positive potential. The potential of the rest of the hydrocarbon chain is roughly neutral[61].

The situation is analogous with samples C and D. As an example, **Figure 1.15** reports an image of sample C one hour after fragmentation (after heating). Sample D (PDMS microlenses on LN Z + face) exhibits a behavior similar to that of sample B, as expected.

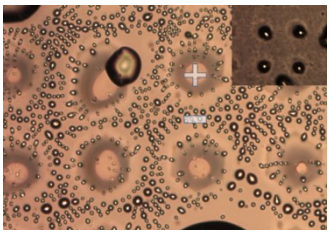

**Figure 1.15**: Microscope image of sample C cooled for 1 hour (in the LC's plane). The domains charges' signs are indicated (Z- face of the crystal). Inset: same image but in the lenses focus plane.

**Figure 1.16** (a)-(b) shows the fragmentation of LC drops after heating and their migration onto microbumps. After one hour, the situation is again similar to the previous experiment but this time the resulting effect is a single drop of LC on each microbump. In case, this latter phenomenon could be exploited to obtain self-arrangement of small LC lenses. In fact, the coalesced LC drop produces a lens effect (**Figure 1.16 (c)**), although smaller than that produced by the PDMS bump (**Figure 1.16(d)**). In the case of sample D, the droplets fragmented pattern occurring after heating is not randomly distributed, as it is for sample A (see Figure 1.11). In fact, as reported in Figures 1.16 (a)-(b), LC droplets are aligned along radial directions passing through the centre of each hexagonal domain.

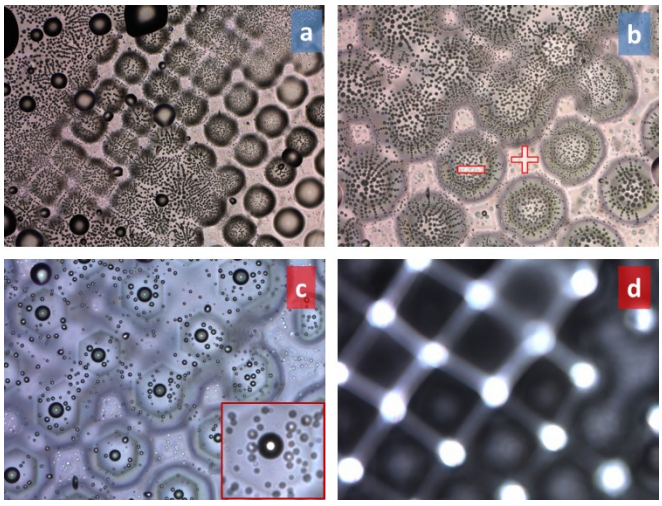


**Figure 1.16**: (a-b) Microscope images of sample D few instants after heating (Z + side of the crystal). The fragmented droplets are onto hexagonal domains (with negative charges), according to the previous measurements. (c-d) Images of the sample one hour later (i.e. after one hour of cooling): (c) in the LC's plane and (d) in the PDMS lenses focal plane. Inset of (c): image in the LC lens' focal plane.

The geometrical arrangement suggests the fragmented drops are aligned along the lines of the electric field components in the plane of the substrate, and travel onto the domain following these lines. **Figure 1.17 (a)-(b)** represents this situation, while **Figure 1.17 (c)-(d)** show a

close-up of Figures 1.16 (b)-(c), respectively, in order to appreciate the lines formed by the LC droplets and their successive migration to the centre of the domain.

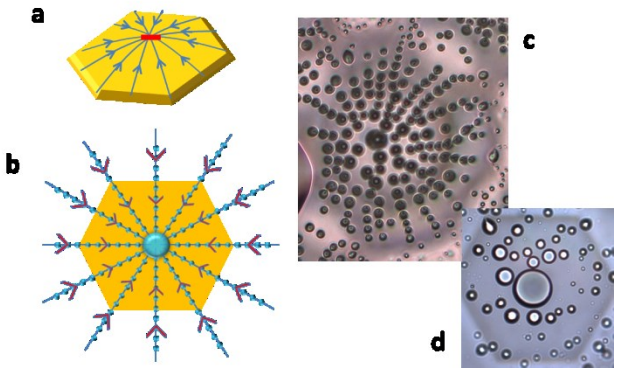


**Figure 1.17**: (a) Side and (b) top view of the electric field lines pyroelectrically generated, going from the positive charges (around hexagons) to the negative (onto hexagons). (c-d) Microscope images of one hexagonal domain of sample D (c) few seconds after heating and (d) one hour later.

In summary, this chapter a novel approach is presented for manipulating LCs by pyroelectric effect where the strong electric fields generated through a thermal stimulus allow the manipulation of liquids in 2D on a substrate. We observe fragmentation of droplets that migrate to different regions of the sample according to the geometry of the LN substrate and following the electric-field lines. The droplets then coalesce into bigger drops, at which point various effects can occur. For example, there is the possibility of new fragmentation (reversibility of the process), square-matrix arrangements, and lens effects (where LC droplets may focus the light passing through them), and alignment of the LC molecules with the electric field (resulting in the appearance of crosses, called Maltese crosses, when the LC is observed under a crossed polarizer).

**References**:


1) S. Liu, J.B.-H. Tok, J. Locklin, Z. Bao, *Small* 2, 1448 (2006).

2) B.S. Gallardo, V.K. Gupta, F.D. Eagerton, L.I. Jong, V.S. Craig, R.R. Shah, N.L. Abbott, *Science*, 283, 57 (1999).

3) F. Mugele, S. Herminghaus, *Appl. Phys. Lett.*, 81, 2303 (2002).

4) G. Beni G., A. Tenan, *J. Appl. Phys.*, 52, 6011 (1981).

5) T.B. Jones, M. Gunji, M. Washizu, M.J. Feldman, *J. Appl. Phys.*, 89, 1441 (2001).

6) R.B.M. Schasfoort, S. Schlautmann, J. Hendrikse, A. van den Berg, *Science*, 286, 942 (1999).

7) F. Mugele, J.-C. Baret, *J. Phys.: Condens. Matter*, 17, R705 (2005).

8) J. Zeng, T. Korsmeyer, *Lab Chip*, 4, 265 (2004).

9) D. Aronov, G. Rosenman, A. Karlov, A. Shashkin, *Appl. Phys. Lett.*, 88, 163902 (2006).

10) D.B. Wang, R. Szoszkiewicz, M. Lucas, E. Riedo, T. Okada, S.C. Jones, S.R. Marder, J. Lee, W.P. King, *Appl. Phy. Lett.*, 91, 243104 (2007).

11) R. Hayes, D.J. Feenstra, *Nature*, 425, 383 (2003).

12) S. Kuiper, B.H.W. Hendriks, *Appl. Phys. Lett.*, 85, 1128 (2004).

13) F. Laurell, M.G. Roelofs, W. Bindloss, H. Hsiung, A. Suna, J.D. Bierlein, *J. Appl. Phys.*, 71, 4664 (1992).

14) C.H. Bulmer, W.K. Burns, S.C. Hiser, *Appl. Phys. Lett.*, 48, 1036 (1986).

15) E.M. Bourim, C.-W. Moon, S.-W. Lee, I.K. Yoo, *Phys. B*, 383, 171 (2006).

16) G. Rosenman, D. Shur, Y.E. Krasik, A. Dunaevsky, *J. Appl. Phys.*, 88, 6109 (2000).

17) R.L. Byer, *IEEE J. Select. Topics Quantum Electron.*, 6, 911 (2000).

18) S. Grilli, M. Paturzo, L. Miccio and P. Ferraro, *Meas. Science and Tech.* 19, 074008 (2008).

19) M. Yamada, N. Nada, M. Saitoh, and K. Watanabe, *Appl. Phys. Lett.* 62, 435-436 (1993).

20) L.E. Myers, R.C. Eckardt, M.M. Fejer, R.L. Byer, W.R. Bosenberg, J.W. Pierce, *J. Opt. Soc. Am. B* 12, 2102-2116 (1995).

21) Rosenblum, B., Bräunlich, P., Carrico, J. P. *Appl. Phys. Lett.* 25 (1974).

22) I. A. Aksay, M. Trau, S. Manne, I. Honma, N. Yao, L. Zhou, P. Fenter, P. M. Eisenberger, and S. M. Gruner, *Science* 273, 892 (1996).

23) Xu, S., Lin, Y.-J., Wu, S.-T. *Opt. Express* 17 (2009).

24) Miccio, L., Finizio, A., Grilli, S., Vespini, V., Paturzo, M., De Nicola, S., *Opt. Express* 17 (2009).

25) Ottevaere, H., Volckaerts, B., Lamprecht, J., Schwider, J., Hermanne, A., Veretennicoff, I., Thienpont, H. *J. Opt. A: Pure Appl. Opt.* 4 (2002).

26) He, M., Yuan, X.-C., Ngo, N.Q., Bu, J., Tao, S.H. *J. Opt. A: Pure Appl. Opt.* 6 (2004).

27) Chang, C.Y., Yang, S.Y., Sheh, J.L. *Microsyst. Technol.* 12 (2006).

28) Shi, J., Stratton, Z., Lin, S-C. S., Huang, H., Huang, T.J. *Microfluid Nanofluid*, 9 (2010).

29) J.-h. Zhu, J.-xia Shi, Y. Wang, P.-sheng He, Chin. *J. Chem. Phys.* 19, 443 (2006).

30) Schilling, A., Merz, R., Ossmann, C., Herzig, H. P. *Opt. Eng.* 9 (2000).

31) Cheong, W., Yuan, L., Koudriachov, V., Yu, W. *Opt. Express* 10 (2002).

32) Monteiro, D.W.D., Akhzar-Mehr, O., Sarro, P.M., Vdovin, G. *Opt. Express* 11 (2003).

33) I. A. Grimaldi, A. De Girolamo Del Mauro, G. Nenna, F. Loffredo, C. Minarini, F. Villani, *J. App. Polymer Science* 122, (2011).

34) Kim, J.Y., Brauer, N.B., Fakhfouri, V., Boiko, D.L., Charbon, E., Grutzner, G., Brugger, *J. Opt. Mater. Expr.* 1 (2011).

35) Huang P.H., Huang T.C., Sun Y.T. and Yang S.Y. *Opt. Express* 16 3041 (2008).

36) Lin T. H., Yang H. and Chao C. K. DTIP of MEMS & MOEMS Stresa, Italy, 26–8 April (2006).

37) Chang S. and Yoon J. *Opt. Express* 12 6366 (2004).

38) Chang C Y, Yang S Y, Huang L S and Jeng T M. *J. Micromech. Microeng.* 16, 999 (2006).

39) Shih T K, Ho J R and Cheng J W J. *IEEE Photonics Technol. Lett.* 16 2078 (2004).

40) Shih, T. K. Chen, C. F., Ho J. R. and Chuang F.T. *Microelectron. Eng.* 83 2499 (2006).

41) Lee S Y, Tung H W, Chen W C and Fang W. *IEEE Photonics Technol. Lett.* 18, 2191 (2006).

42) Chandra D, Yanga S and Lin P C. *Appl. Phys. Lett.* 91 251912 (2007).

43) Peterson S.L., McDonald A., Gourley P.L., Sasaki D.Y., *J. Biomed. Mater. Res.* 72A (2005).

44) Morefield S.I., Keefer E.W., Chapman K.D., Gross G.W., *Biosensors & Bioelectronics* 15 (2000).

45) Andersson H., van den Berg A., *Lab on Chip* 4, (2004).
46) Atsuta K., Noji H., Takeuchi S., *Lab on Chip* 4 (2004).
47) Chen C.S., Mrksich M., Huang S., Whitesides G.M., Ingber D.E., *Science* 276 (1997).
48) Ferraro P., Grilli S., Miccio L., Vespini V., Appl. Phys. Lett. 92 (2008).
49) Miccio, L., Paturzo, M., Grilli, S., Vespini, V., Ferraro, P. *Opt. Lett.* 34 (2009).
50) G. Gibson, D. M. Carberry, G. Whyte, J. Leach, J. Courtial, J. C. Jackson, D. Robert, M. Miles, M. Padgett, *J. Opt. A: Pure Appl. Opt.* 10, 044009 (2008).
51) T. H. Kim, Y. W. Lee, I. W. Lee, S. C. Choi, *Appl. Opt.* 39 , 2054 (2000).
52) A. Fratalocchi, R. Asquini, G. Assanto, *Opt. Express* 13, 32 (2005).
53) J. A. Davis, G. H. Evans, K. Crabtree, I. Moreno, *Appl. Opt.* 43, 6235 (2004).
54) Y. J. Kim, M. R. Luo, W. Choe, H. S. Kim, S. O. Park, Y. Baek, P. Rhodes, S. Lee and C. Y. Kim, *J. Opt. Soc. Am. A* 25 , 2215 (2008).
55) H. T. Dai, Y. J. Liu, X. W. Sun, D. Luo, *Opt. Express* 17, 4317 (2009).
56) H. Ren , S.-T. Wu , *Opt. Express* 14 , 11292 (2006).
57) Z. Ghattan, T. Hasek, R. Wilk, M. Shahabadi, M. Koch, *Opt. Commun.* 281, 4623 (2008).
58) Y. Yuan, J. He, J. Liu, J. Yao, *J. Phys.: Conf. Series* 276 , 012228 (2011).
59) I. Viola, M. Mazzeo, A. Passabì, S. D'Amone, R. Cingolani, G. Gigli, *Adv. Mater.* 17 , 2935 (2005).
60) S. Herminghaus , K. Jacobs , K. Mecke , J. Bischof , A. Fery , M. Ibn-Elhaj, S. Schlagowski , *Science* 282 , 916 (1998).
61) M. Szaleniec , R. Tokarz-Sobieraj , W. Witko , *J. Mol. Model.* 15, 935 (2009).
62) R. B. Bogoslovov , C. M. Roland , J. Czub , S. Urban , *J. Phys. Chem. B* 112 , 16008 (2008).
63) P. Mokrý , M. Marvan , J. Fousek , J. *Appl. Phys.* 107, 094104 (2010).
64) S. Liu , J. B.-H. Tok , J. Locklin , Z. Bao , *Small* 2 , 1448 (2006).
65) T. Kimura , M. Yamato , A. Nara , *Langmuir* 20, 572 (2004).
66) R. Cicoria , Y. Sun , *Nanotech.* 19, 485303 (2008).
67) K.-L. Cheng , Y.-J. Sheng , S. Jiang , H.-K. Tsao , *J. Chem. Phys.*128, 101101 (2008).

# Chapter 2

## 2.1 Pyro-Electrohydrodynamic dispenser

Techniques for printing patterns with inorganic, organic and biological inks at high resolution represent one of the major point of interest in different fields of technology from experimental to industrial applications. Different printing methods have been developed in recent years: stationary liquid microjets dispense droplets by inducing fluid interface instabilities[1], whereas atomic force microscope probes dispense nanolitre droplets through an aperture in their apex[2,3]. Other approaches make use of electrohydrodynamic (EHD) jetting[4], which involves a tube with a meniscus bearing a Taylor cone profile spraying a fine jet. In fact, it is also possible to use electric fields to draw narrow jets of liquids from fine apertures[5] in a process that was first studied in experimental detail by Geoffrey Taylor[6] in 1964. When implemented with pens based on micro- or nanoscale glass capillaries, the EHD effects studied by Taylor enable printing with resolution approaching 100 nm using pigments and a variety of advanced materials, such as conducting polymers, single-walled carbon nanotubes, oligonucleotides and colloids[7-9]. On-demand droplets with sizes much smaller than that of the delivery nozzle have been obtained by pulsed EHD liquid jetting[10,11] or through the application of electrostatic fields[12]. Today one of the most prevalent form of the drop on demand is the desktop inkjet printer, in which localized heating leads to the controlled formation and ejection of small droplets of ink at rates of tens of thousands per second. This technology, which provides a resolution of several tens of micrometres, plays a major role in printing for the graphic arts. High resolution EHD jet printing (below the limit of commercial thermal or piezoelectric inkjet printers, which produce 10–20-pl droplets and line widths down to 50 mm) has been achieved using microcapillary nozzles[13]. The capabilities of the EHD-jet has created new opportunities for printing in areas of technology and manufacturing. For example, there is growing interest in the development of e-jet printing techniques for applications in electronics, optoelectronics and biotechnology, where high-resolution patterning of functional materials in liquid form has the potential to provide advantages in cost and capabilities over established methods such as photolithography. In fact, all the EHD techniques previous described, provide submicrometer droplets and have the flexibility to pattern fragile organics or biological materials that are, instead, incompatible with conventional methods such as photolithography. However, dispensing liquids for biochemical analysis or patterning requires the arrangement of appropriate electrodes and the use of high-voltage circuits between the liquid reservoir and the receiver substrate. Moreover, the capillary nozzles require

complicated fabrication procedures and may be subject to cross contamination. In this chapter a new concept of droplet generation based on the pyroelectrohydrodynamic effect is described. The method is analyzed for the direct drawing and dispensing of small droplets from liquid drops or film reservoirs. For the smallest ink droplets, printing resolution down to 300 nm (corresponding to attolitre volumes) was achieved. This approaches some of the best results reported using nanocapillary nozzles[7,8] and greatly exceeds the possibilities provided by conventional inkjet methods. This technique does not require electrodes, high-voltage circuit connections or special capillary nozzles. In fact, the electric fields are generated pyroelectrically using functionalized substrates of Lithium Niobate (LN) for transferring liquids between two substrates and manipulate the droplets three dimensionally. When the niobate substrate is placed near a second substrate that supports ink droplets or films of liquid, the pyroelectric effect in the LN substrate can initiate electrohydrodynamic responses. So that, when the electric fields exceed a critical magnitude, pulsating jets emerge, pulling the liquid in the form of a rapid succession of fine droplets. These pulsations continue until the fields dissipate on cooling of the pyroelectric material, and the ejection of the droplets can therefore be reversibly turned on and off in this manner. The heating creates a sort of 'virtual nozzle' through localized EHD effects, thereby omitting the need for actual nozzles. The simplicity of the technique suggests potential uses in a range of liquid manipulation fields, such as generating and dispensing daughter droplets, fragmenting microlitre drops and liquid printing. The versatility of the pyroelectric approach to EHD-jet printing, the simplicity afforded by the absence of nozzles, electrodes or high-voltage power supplies, and the potential for high-speed printing collectively make the method very attractive for many applications exploring advanced inks and exploiting the capabilities for applications in biology, printed electronics and related areas.

## 2.2 Pyro-Electrohydrodynamic dispenser: Set-up

Electric forces are activated pyroelectrically by scanning a heated-tip on a functionalized substrate and the pyroelectric functionality of a LN substrate is used for non-contact manipulation of liquids leading to the formation of a smart "dispenser". The technique presented here allows one to avoid the use of high-voltage power supplies and electrical circuits, and moreover there is no need to design and fabricate nanocapillary nozzles. The flexibility offered for manipulating the dispenser is intriguing, demonstrating that various

functionalities can be engineered for a smart manipulation of the liquid reservoir and of the dispensing process.

**Figure 2.1 (a)** shows the schematic view of the pyro-electrohydrodinamic system[14]. A liquid drop or a liquid film is deposited on a microscope glass slide, while the upper plate is a z-cut LN wafer. The experiment made use of a non-contact thermal stimulus applied through a IR source (CO2 laser) emitting at a wavelength of $\lambda$=10.6 μm but another possible heating source would be an hot tip source in direct contact with the LN crystal. The laser and the tip can be scanned over the crystal surface to induce point-wise thermal-stimuli. LN reacts to the thermal-stimuli by building-up an electric potential across the z-cut LN crystal's surfaces because of the pyroelectric effect, that consists in the spontaneous polarization change $\Delta$Ps following to a temperature variation $\Delta$T. At equilibrium, the crystal Ps is fully screened by the external screening charge and no electric field exists[15]. When the tip-source or the laser beam locally heats the crystal, a sudden surface charge density $\sigma$ immediately appears given by $\Delta\sigma = p\Delta T$ neglecting losses, where Pc is the material-specific pyroelectric coefficient (Pc= -8.3 x 10 -5C/°C/m2 for LN @ 25°C). The pyro-electric field induced by the temperature gradient exerts an attractive force on the liquid reservoir drop. The pyro-electric field is described through a multiphysics analysis using a finite-element method as described in *Annex* 1 and displayed in **Figure 2.1 (b)**. In the case of a sufficiently strong electric field, thin liquid jets can be released from conical tip structures (similar to Taylor's cone usual in electro-spray). For the experiment performed and described in this work the liquid is not conductive, consequently we are not exactly in the Taylor's cone regime[16].

When the liquid (either the sessile droplets or a film) starts to deform under the action of the electric field, two evolutions are possible. Case (I): if the liquid volume and the separation distance D between the two plates are appropriate then a stable liquid bridge can be formed, **Figure 2.1 (c)**. For a given volume, the critical distance below which a bridge can be established is expressed by [17]

$$Dc = (1 + \vartheta/4)\, V^{1/3} \qquad (1)$$

where $\theta$ is the contact angle and V is the volume.

Nevertheless the most relevant case for us is the Case (II): if the separation D is above the critical value, a stable liquid bridge cannot be established between the plates. We designed our experiments with the aim at using such instability for dosing and dispensing liquid drops.

The typical situation of liquid dispensing in case of two different liquids, almonds oil and polydimethylsiloxane (PDMS), are shown in **Figure 2.1(d)** and **Figure 2.1(e)** respectively.

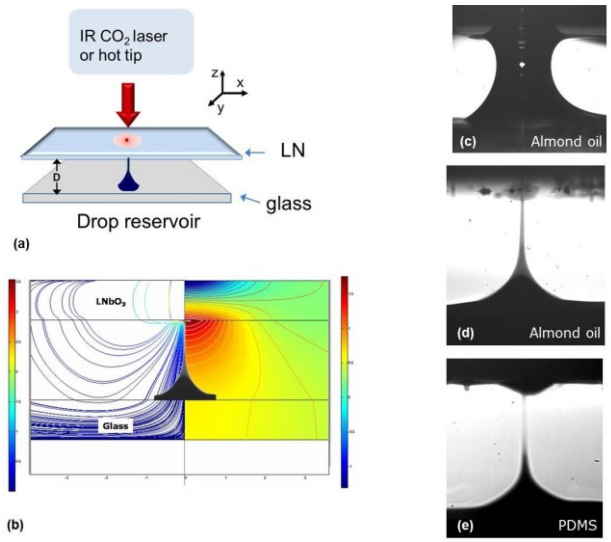


**Figure 2.1**: (a) Schematic diagram of the dispensing microfluidic system by using the IR laser (CO2) as a thermal-stimuli tool. A sessile drop or liquid film is deposited onto the bottom substrate (glass). (b) 3D axis-symmetric plot of the electric field lines (left) and electric potential (right) obtained by a finite element method simulation. The electric potential is generated by the pyroelectric effect induced onto the functionalized substrate through the thermal stimuli of the heated-tip. (c) Image of the typical liquid bridge obtained when D is shorter than the critical distance (see Eq.(1)). (d) Image of the typical liquid shooting effect during the dispensation of almond oil through the heated-tip thermal excitation. (e) Same as d, but in this case the liquid is PDMS. Due to the higher viscosity the blasting liquid cone is continuous.

**Figure 2.2** (a)-(b) shows two sequences of liquid dispensing in which nanolitre and picolitre almond oil droplets were dispensed from a liquid film and from a sessile drop reservoir stimulated by the hot tip and by infrared laser pulses (power, 10 W; length, 100 ms) respectively. The phenomena were captured by a CMOS-camera with a recording frame rate of 125 frame $s^{-1}$. The dynamic evolutions show that the reservoir first deforms into a conical tip, with a height that increases under the pyroelectrohydrodynamic force, and then behaves as a 'dispensing gun' that dispenses droplets periodically until the electric field vanishes. **Figure2.2**(c)-(d) shows the temporal height variation of the film and drop reservoirs (main plots), respectively, and the volume transfer rates (insets) corresponding to the sequences in Figure 2.2 (a)-(b). The film dispensed 160 nl after 5 shots with a period of 100 ms and a rate

of 30 nl per shot, whereas the drop dispensed 164 nl after 55 shots with a period of 200 ms and a rate of ~ 3 nl per shot. Figure 2.2(a) shows that the initial volume (180 nl) of the drop reservoir was reduced to ~ 16 nl after 55 shots (last frame of the sequence). The drop acts like a dispensing-gun with a repetition rate that depends on the liquid response to EHD force. The experiment clearly shows that, after the Taylor's cone has been established to allow the first shot, the dispensing-gun blasts liquid droplets periodically till the electric filed is on. The period of the shooting was of 50ms. The cycle is repeated many times during cooling. Further studies should address a deeper investigation on periodicity of the process and the volume regularity of the sequential shoot drops.

Figure 2.2(b) shows how the CO2 laser beam can be used to extract completely the liquid from the reservoir-drop, probably thanks to the higher heating efficiency. In particular, the irradiation of the substrate by five laser pulses (power of 10W and 100ms long) made the droplet reservoir to dispense up to 55 shots.

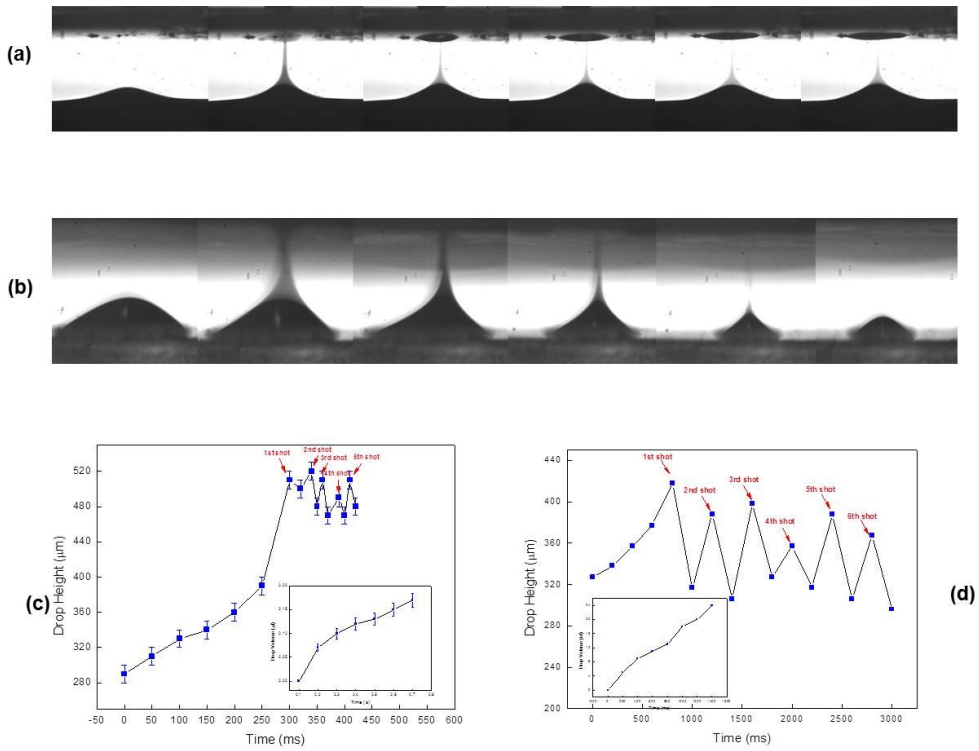


**Figure 2.2**: (a) Sequence of different dispensing shots in case of liquid film and thermal stimuli induced by the heated-tip. (b) Sequence of several dispensing shots in the case of a sessile droplet and thermal stimuli induced by the IR laser. (c) (main) Plot of the temporal height variation of the droplet in the case of Figure 2 (a) and (inset) plot of the corresponding volume transfer rate. The single shots are detectable. The period of the shooting cycle is 50 ms. (d) (main) Plot of the temporal height variation of the droplet in the case of Figure 2 (b) and

(inset) plot of the corresponding volume transfer rate. The single shots are detectable. The period of the shooting cycle is 200 ms.

## 2.3 Functionalities of the Pyro-Electrohydrodynamic dispenser

The flexibility of the pyro-dispenser is demonstrated by the following experiments where various functionalities have been proved. The movement of either the heated-tip or the laser beam allows for example one to change the dispensing direction of droplets in a wide solid angle as shown in **Figure 2.3(a)**. In fact, the electric field distribution can be changed rapidly (~2 seconds) by varying the heated-tip position, because the regions with highest electric field follow the tip's movement. The off-axis shooting angles reach values up to ~ 20° degree, thus giving the possibility for dispensing liquids on an area of ~ 23 $mm^2$ even though the droplet reservoir maintains a fixed position. In this way it is possible to deliver liquid in different locations along a line by the continuous shooting effect occurring during an appropriate movement of the dispenser while larger angles induce the displacements of the drop reservoir. **Figure 2.3** refers to two different experiments: sessile drop (**Figure 2.3(b)**) and a film layer (**Figure 2.3(c)**). In both cases the dispenser can be moved easily, just by moving the heated-tip. However in the first case the sessile droplet starts to move only at a critical angle. In fact the asymmetrical deformation experienced by the drop, under the action of no-axial electric force, creates the unbalance of the solid-liquid interface tensions with a net force resultant (Figure 2.3(b)) that pushes forward the drop. This unbalance causes the drops displacement in analogy with what happens for thermocapillarity where instead the thermal gradient causes the unbalance of the solid-liquid interface tensions. Figure 2.3(b) shows the possibility to dispense the liquid in three different locations along a single scanning line, by moving the drop. In the case of a liquid layer the movement could be easier because no solid-liquid interface tension prevents the movement of the blasting cone. A sequence of images show (Figure 2.3(c)) the lateral movement (x-axis) up to 1.6 mm with no interruption of dispensing action and 1 mm along the y-axis.

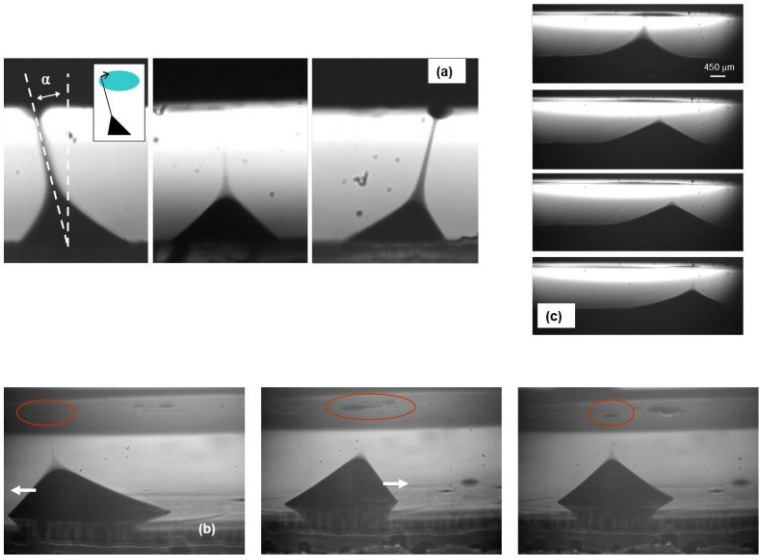


**Figure 2.3**: (a) Dispensing nL liquid droplets along angled directions (~20°) from a sessile drop reservoir. (b) Sessile droplet reservoir on PDMS coated glass. The activation and the successive lateral displacement of the "dispensing gun" allowed one to deliver liquid along relatively short liquid lines at different locations. (c) In case of the liquid film, the "dispensing gun" can be easily moved according to a 2D geometry.

One more fascinating function that can be engineered is the harmonic combination of the dispensing function synchronized with the transportation of droplets, while they are continuously formed shown in the sequence of **Figure 2.4** . The sequence of captured images shows clearly the formation and synchronized carrying of three distinct droplets in a row on right side. Such drops could be easily collected and managed into a microfluidic system. This function can be successfully implemented by choosing in an opportune way the position of the thermal stimuli (heated-tip in this case). The beauty of the physics is that the process seems to be self-organized based on two different physics effects: EHD and thermocapillarity but activated by a single external stimuli. The lateral displacement is driven by thermocapillarity that pushes the droplets in colder regions (in our case the right and left sides).

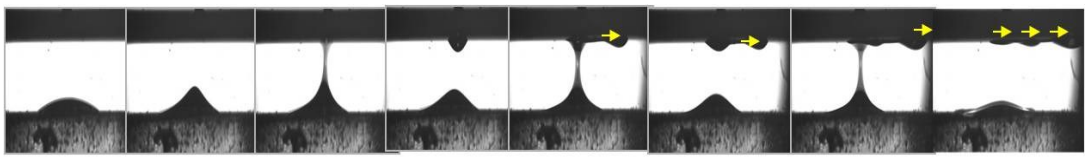

**Figure 2.4:** Combination of the dispensing function with the transportation of the droplets. The angle in this case is clearly visible in the picture and is ~ 11° with respect to the normal to the substrate.

It is important to note that the thermal stimulus generated by a laser provides different advantages. The thermal excitation can be addressed easily in different locations (i.e. in correspondence of the different sessile drop reservoirs) by the precise movement of the beam. The heating energy can be varied by modulating the beam power. The beam focusing by a lens allows to better restrict the area on which the thermal stimulus should be applied. As illustrated in **Figure 2.5(a)** the laser beam was addressed to the three different drop reservoirs deposited on the glass substrate as shown in the perspective view in **Figure 2.5(b)**. The drops were activated sequentially. High throughput dispensing is possible by splitting the laser beam to get parallel blasting from multiple reservoir droplets. Different sessile drops can be subjected to parallel laser dispensing by addressing the laser beam to different positions. In fact, the laser-induced process allows to extract small amounts of liquids or even to deliver all the volume of the liquid drop reservoir to a single or to multiple sites.

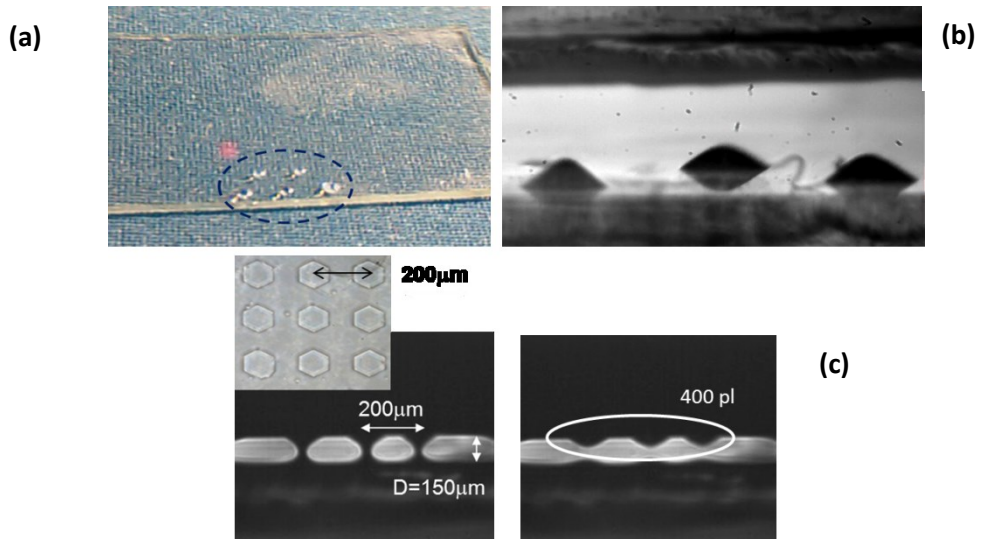


**Figure 2.5**: (a) Five sessile drop reservoirs on the PDMS coated glass. (b) Sessile drops activated in **c** for multiple dispensing. The liquid deposition from each sessile drop arranged according to a 2D geometry on the bottom glass substrate was possible by scanning the IR laser on the substrate in three different locations. (c) Since D was shorter than the critical distance, the breaking of the liquid bridges gave the possibility of dispensing 400 pL pendant droplets onto the functionalized substrate corresponding to the desired locations driven by the geometry of the PPLN sample.

## 2.4 Laser induced dispenser and visualization of the pyro-electric field lines

This laser-induced process has the attractive feature to be an optofluidic actuation that can be exploited for liquid delivering and patterning in remotely, non-contact way. The experiment represents at the same time an innovative methodology for the visualization in real time of electric field stream lines. Furthermore this approach could also be introduced as a new tool to measure the velocity field of femto-drops in lab-on-chip modality. Tracking the dispensed drops in real time, in terms of volume, velocity and spatial distribution, would be a powerful method for all EHD technologies. The results reported are in agreement with the theoretical calculations. The irradiation by an IR laser is the thermal stimulus used to activate the pyroelectric effect onto the polar dielectric substrate. The technique provides a very flexible system since it allows one to extract different liquids (oil and polymers) in a non-contact and remote way thus leading to novel fascinating optofluidic functionalities.

The laser-induced EHD reaches the values commonly adopted in standard EHD jet printing methods. With the experiments described in the following it is represented a novel visualization of the electric field lines induced by the pyroelectric effect driven by the CO2 laser irradiation. The LN substrate is essentially transparent in the range of 0.4–5.0 $\mu$m and with strong absorbance at longer wavelengths such as $\lambda$ = 10.6 $\mu$m. When the crystal is subjected to the thermal stimulus of a continuous wave CO2 laser emitting at a wavelength of $\lambda$ = 10.6 $\mu$m (power of 10 W, tunable through an external voltage) the pyroelectric surface charge distribution builds up quickly on both surfaces. Consequently, the electrical potential across the *z*-axis of the LN wafer drives, through the piezoelectric effect, high acceleration at the LN surfaces. If a thin liquid layer is present, the strong acceleration creates a spray emission of femto-litre or even smaller droplets. The droplets are ejected down by piezo-mechanical acceleration at the LN surface and then attracted again towards the LN substrate by the laser- pyroEHD. In **Figure 2.6** it is possible to observe clearly how the polarized femto-droplets traced the path of the electric field lines in very good agreement with the numerical calculation. In fact in Figure 2.6(*b*) the plot of the electric field lines coming from the simulation as described in the previous section is shown. Furthermore the presented results also demonstrate that by remote and non-contact action via an IR laser it is possible to generate liquid spray as an additional functionality to those reported in our previous paper[14].

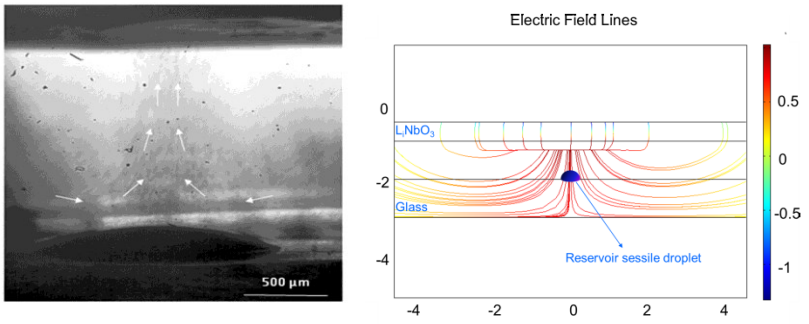


**Figure 2.6**: (a) Visualization of the electric field stream lines produced by the laser-induced EHD technique, femto-litre oil droplets following the electric stream field lines in agreement with the numerical calculation. (b) Plot of numerical electric field stream lines obtained by numerical simulation.

A different experiment was performed in order to demonstrate the possibility of dispensing nL droplets also in case of a polymer liquid. In fact, the CO2 laser beam can be easily used to extract liquid nanodroplets from a polymer film through an electrode-less configuration. In particular, we examined the milking process of polydimethylsiloxane (PDMS Dow Corning Sylgard 184, 10:1 mixing ratio base to curing agent) droplets drawn from a polymer film. A layer of PDMS polymer solution was spin coated onto a microscope glass slide at 4000 RPM for 1 min. That slide was used as the base of a tray of 300 $\mu$m height, above which was placed a polished LN *z*-cut crystal. Irradiating the crystal substrate by three consecutive laser pulses (power of 10 W and period 400 ms long) we can observe the activation of the milking process from the liquid film reservoir. The three laser pulses allow us to generate a process that immediately starts after the irradiation and is about 15 s long. The first liquid jet causes the initial transfer of a single droplet with an approximate volume of 250 pL and a diameter of 140 $\mu$m. Afterwards a set of smaller droplets are ejected by the liquid film reservoir. The final total volume transferred after 15 s was estimated to be 2.5 nL while the drop diameter appears to be 330 $\mu$m. Studying the process we can find a relationship between the frequency of dispensing droplets and the reservoir parameters as a function of the fluid properties. In fact, in the case of the oil reservoir the shooting period (200 ms) is exactly the same as that of the laser pulses. Using polymer materials, instead, we have to increase the period of the laser pulses up to 400 ms in order to overcome the intrinsic viscosity of the material, its surface tension and deform it into the Taylor cone. In conclusion, the use of a laser beam as heating source provides different advantages. The system provides high flexibility and the possibility of remote and rapid scanning of the energy source in non-contact mode favors a non-invasive and more efficient heat-transfer. In fact, we can finely regulate the beam waist and power,

thus controlling the amount of sample area to be excited and the corresponding temperature. Moreover, the non-contact heating prevents eventual damage to the sample.

### 2.5 Laser induced dispenser activated by plasmon resonace of gold Nanorods

Using the laser-assistant dispensing by CO2 lasers leads the possibility of working in a no-contact mode but sacrificing the compactness and making difficult the beam alignment due to invisibility to the naked eye. It would be of great interest for all the lab-on-chip application the possibility of using a laser in more simple and direct way. For this reason laser-assisted system for dispensing liquid micro-droplets by near infrared illumination of a pyroelectric crystal functionalized with gold nanorods embedded into polyvinyl alcohol was investigated. This laser-assisted electro-hydrodynamic technique may open the way to the development of more compact and non-invasive nano-dispensing devices. The non-invasive near infrared source resonates with the plasmon oscillations of the gold nanorods could provide a controlled thermal stimulus able to generate the pyroelectric effect. The resulting electric field interacts electro-hydrodynamically with a liquid reservoir leading to precise drawing of micro-litre droplets. All lab-on-a-chip systems are of great interest in biotechnological and chemical applications, thanks to their possibility of producing the desired products faster and in greater yield and purity compared to conventional techniques[18]. Basically two main classes of microfluidic approaches have been developed during the last decades. The continuous flow microsystems[19] usually consist of a network of micrometresized channels, thus suffering from various drawbacks, including large dead volumes and obstruction of channels. Moreover, they make use of valves and pumps, which increases complexity, cost and fragility of the system. On the other hand, the so-called “digital microfluidics” [20] confine the reactions into single droplets, even with high monodispersivity[21]. A significant advantage of droplet-based systems is that they are compatible with wall-free structures, so that the operations can conveniently performed on the surface of a planar substrate. Surface microfluidics are simpler to fabricate and assemble and, lacking fixed microchannels, they can be reconfigured more easily. Starting from the successful combination of a near infrared (NIR) source with the plasmon resonance of gold nanorods (GNRs) they were patterned onto the surface of a LN crystal. This system exhibits additional advantages compared to the electrode-and nozzle-free pyro-EHD configuration developed previously described. The stimulation of the pyro-EHD effect is performed optically by a compact lasers source launched in fibre. Such fibre-based setup favours the integrability and makes the light addressing easier thanks to its visibility to the

naked eye when the light hits the target. In this context, a portable system could be fabricated for biosensing applications where on site drawing of very little amounts of liquids is needed. Moreover versatile dispensing modes (serial and multiple) are possible by simply modulating the distance between fibre and crystal and therefore by lens-free manipulation of the beam expansion. Furthermore, additional versatility and precision are provided here by the possibility of patterning the heat source onto the pyroelectric crystal. In fact, the thermal gradient is ensured by the efficient photothermal conversion of the GNRs during the plasmon resonance induced by laser illumination, so that the pyroelectric effect can be generated with high precision and selectivity by near field excitation through an appropriately addressed small beam or alternatively by a largely expanded beam illuminating a pattern of GNRs. The selectivity offered by the patterning approach reduces the stress induced to the crystal and provides, at the same time, better control over the excitation process. In addition, the use of NIR light minimizes undesirable absorption from solvents and reagents, which occurs usually in case of visible and IR frequencies, thus producing undesirable signals. Moreover, compared to the far IR output of a CO2 laser, with a 20-fold smaller wavelength, NIR light may be focused to smaller spots on the crystal, thus improving the spatial resolution and therefore the control of the dispensing process. The thermal gradient can be induced with relatively high accuracy by modulating the laser power with high spatial selectivity[22]. Gold particles are dispersed into a viscous aqueous solution containing bromide and 6% (w/w) polyvinyl alcohol (PVA) [23]. Droplets of this suspension with volumes of about 2 µl are casted onto LN after cleansing with acetone and ethanol in an ultrasound bath and left to dry at room temperature overnight under a hood creating a sort of patterning over the crystal surface. The GNR-LN device can be activated by NIR light to provide a cascade of photothermal and pyroelectric conversions. **Figure** 2.7 shows the top view of the GNR-LN device used in this work, where an array of 3x3 films with 2mm diameters was patterned.

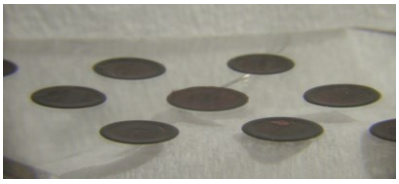

**Figure 2.7**: Top view of an exemplary GNR-LN wafer used in this work. Nine PVA films containing a dispersion of GNRs are deposited onto a LN crystal wafer. The diameter size of the films is about 2mm while the thickness ranges between 20 and 50 mm.

The versatility and the reliability of the laser assisted EHD technique were investigated under three main configurations, as shown schematically in **Figure 2.8**. Basically, three parallel and horizontal plates made the set-up: the base glass slide with the liquid reservoir; the target glass slide facing the base (at a distance of about 2mm) and receiving the drawn droplets; the driving GNR-LN plate back-illuminated by the NIR source. Specifically, the light source consisted of a AlGaAs diode laser (Mod. WELD 800 El.En. S.p.A., Italy) emitting at 810 nm and launched into a 300 lm core diameter optical fibre. The GNR films absorbed the impinging light almost totally, leaving less than 10% reflected. The electric field induced by the thermal treatment was able to exert a significant hydrodynamic pressure onto the underlying reservoir, thus leading to the dispensing of small droplets from the base plate to the target plate or even the formation of a bridge between the two plates[24]. A IR thermocamera (ThermoVisionTM A20 M by FLIR Systems, Inc) revealed that temperature of the GNR in PVA film can reach up to 100 °C; at this temperature of the PVA patterned film, the target slide, on which the LN crystal is placed, is about 50 °C. colder. However, thanks to the versatility of the technique that allows one to use lower power laser and/or shorter illumination, such temperatures may be reduced further. Since the droplets dispensing is driven by the generated electric field, the laser assisted EHD technique works well when target plate and LN wafer are closed but not in contact; for instance, when they are at a distance of 100 mm, the target plate remains at room temperature and the experimental sequence is perfectly reliable. The configurations displayed in Figs. 8(a) and 8(b) had both a separate distribution of the reservoir and of the GNRs on the LN crystal, with drops on the base and an array of (3x3) GNR on the driving plate. However, a single expanded beam excited simultaneously the GNR films in case (a), while a scanning small sized beam was used in (b) for single spot excitation. Therefore, in case (a) a multiple dispensing effect was obtained where sub-microliter droplets were drawn from the base selectively and, simultaneously, in correspondence of the patterned GNR spots. In case (b) the droplets were drawn separately from the base drops, thus obtaining a serial dispensing effect. Conversely, the configuration in (c) consisted of an extensive distribution of both the reservoir and the GNRs, with a free surface water reservoir as base (around 1 ml volume) and a homogeneous layer of GNRs (area around 1 cm2) on the driving plate, excited locally by a scanning laser beam.

In this way a serial dispensing effect was demonstrated also in case of large reservoir. The laser incident power depends on experimental parameters such as the volume of the reservoir drop and the distance between the two plates. From the experimental point of view 0.2W is

the minimum laser radiation incident power needed to trigger a stream of droplets from the reservoir. The PVA+GNR layer reflects less than 10% of this incident light energy and it extinguishes more than 95% of this energy light which is converted into heat by more than 90% [25]. The electric field appearing after a temperature change of the pyroelectric LN crystal relaxes mainly due to the screening of the polarization surface charges by charged particles adsorbed form the surrounding medium[26]. As the thermal mass of the absorber determine its response time in temperature, the minimum laser power can be lowered and the efficiency of the mechanism can be improved by using a thinner crystal (of the order of 10 mm) that could be difficult to handle and could change dramatically the geometry of the experiment.

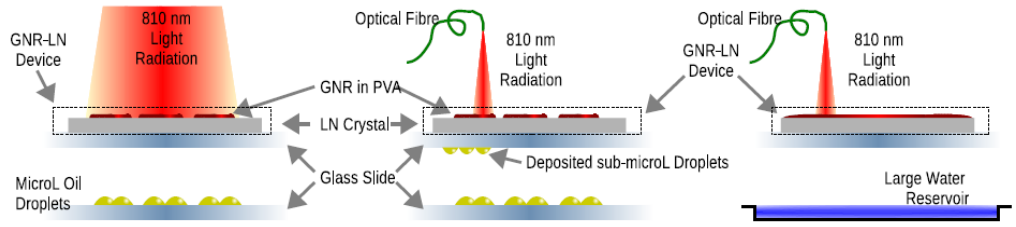


**Figure 2.8**: Side view of the setup for the three experimental configurations used in this work. For all three schemes two microscope slides are mounted in parallel and horizontal. The GNR-patterned LN wafer is positioned on the upper slide with the GNR films on top. The lower slide hosts a set of drop or a macroscopic liquid reservoir. The distance between the GNR-LN device and liquid reservoir is about 2 mm. Laser radiation from an AlGaAs diode laser at 810 nm is launched into a 300 lm core diameter optical fiber which is used to excite the GNR-LN device. (a) An entire pattern of films is illuminated at the same time, diameter of each film is about 2 mm. (b) Individual films are illuminated one at the time. (c) A large film (size 10 mm) is heated pointwise by light from a fiber tip and can activate dispensing from a large free surface reservoir.

In summary in this section an alternative way of activation of the pyro-electric effect is presented. In fact, the resonance activated through the GNRs via a laser assisted technique enables the direct activation of the pyroelectric effect into a LN crystal through a compact, versatile, and light source. Moreover, thanks to the availability on one side of a laser exiting an optical fiber and, on the other side, of activation sites of the pyroelectric effect patterned directly onto the driving crystal, the dispensing is highly versatile and resolved. Both serial and multiple dispensing were demonstrated by playing with the degree of expansion of the beam, namely, by modulating simply the distance between the fiber and the GNR device. In addition, the fiber-based activation enables the stimulation of jetting cones with high fidelity and resolution, even in case of free surface reservoirs. The method has been applied to different kinds of liquids, including oil and water with a rather fast response. The possibility

of using NIR laser for stimulating the EHD force opens the way for compact, cost-effective, and integrated systems with minimal interference with the solvents and reagents constituting the liquid droplets.

### 2.6 Dispenser for liquid printing and patterning at high resolution

The Pyro-dispenser was implemented under a different configuration in order to improve its performance. All of the above experiments clearly show the possibility of drawing and dispensing liquid samples from a drop or film reservoir onto a functionalized substrate such as LN through intriguing functionalities. Anyway some drawbacks exist that prevent the application of the technique for developing a reliable tool for dispensing liquid droplets or lines with stable and defined volumes. In fact, the deposition of the droplets directly onto the warm LN wafer causes the spreading of the liquid due to the electro wetting effect. In other words, the uncompensated charges generated pyroelectrically on the crystal surface reduce the surface tension of the dispensed droplets, causing spreading. Moreover the deposition of droplets onto chips of interest which are different from the LN plate would be desirable. In order to overcome these disadvantages the set-up was improved introducing a dielectric substrate between the base and the crystal. The new configuration allows one to avoid the spreading of the dispensed droplets, and gives the possibility of dispensing the liquid droplets according to specific geometries, such as aligned separate droplets or continuous lines. It is well known that, in the general case of a droplet on a surface, the surface tensions at the solid-liquid $\gamma_{sl}$, solid-gas $\gamma_{sg}$, and liquid gas $\gamma_{lg}$ interfaces are described by the one-dimensional Young equation:

$$\gamma_{sl} + \gamma_{lg} \cos\theta = \gamma_{sg} \qquad (2)$$

where $\theta$ corresponds to the contact angle of the droplet. **Figure 2.9** shows the schematic view of the pendant droplet shot onto the LN crystal when subject to the thermal stimuli and on the resist coated glass slide.

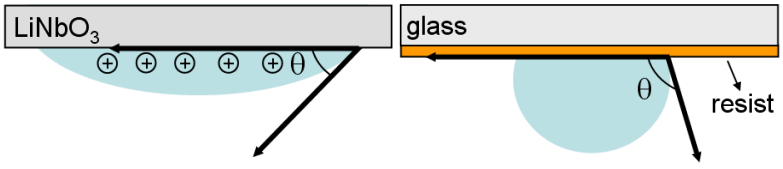


**Figure 2.9**: Schematic view of the pendant droplet shot onto (a) the LN crystal and (b) the resist coated glass slide.

In case of LN, the pyroelectric effect generates uncompensated charges on the crystal surface, thus reducing the surface tension $\gamma_{sl}$ at the solid-liquid interface according to the Lippman equation[27]:

$$\gamma_{sl}(V) = \gamma_{sl0} - \frac{1}{2} c V^2 \qquad (3)$$

where $\gamma_{sl0}$ corresponds to zero charge condition and $c$ is the capacitance per unit area assuming that the charge layer can be modeled as a symmetric Helmholtz capacitor[28]. The voltage $V$ is related to the electric field generated by the pyroelectric charges. Even though in the present work the surface was not a metal and the liquid was not an electrolyte, as assumed by the double charge model[29-31], a similar model still describes the effect in the case of dielectric surfaces[29]. Therefore, the contact angle $\theta$ of the droplet is clearly reduced in case of the LN substrate compared to that occurring in case of the glass substrate. This is due to the surface charges generated pyroelectrically at the solid-liquid interface, thus leading to the spreading of the droplet clearly observed experimentally. The improved set-up used in this work is based on the scheme of Figure 2.9 where the spreading of the droplet is clearly avoided thanks to the absence of surface charges.

A liquid drop was deposited onto a glass slide over which a z-cut LN wafer was positioned at a changeable distance. A photoresist coated cover glass was inserted in between and mounted onto a computer controlled x-y translation stage. A hot tip was locally in contact with the LN crystal and induced a point-wise thermal-stimulus to dispense separate droplets or lines in case of shorter distance between the reservoir and the resist coated substrate, as shown in **Figure 2.10**.

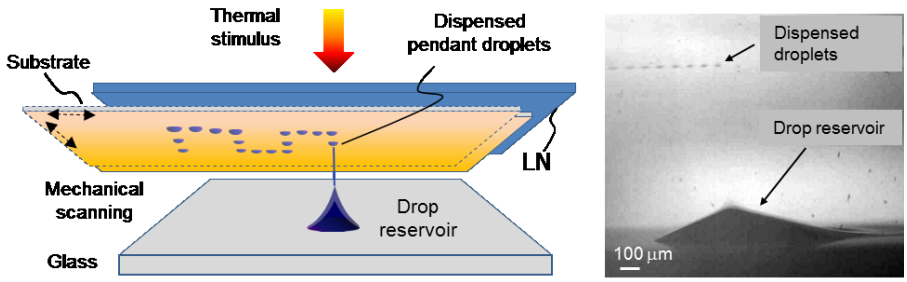


**Figure 2.10**: (a) Arrangement for liquid dispensing onto a dielectric substrate. A photoresist spin coated cover glass is inserted in between the LN upper substrate and the glass plate in order to avoid the droplet spreading and to dispense droplets on different substrates. (b) Side view of the droplet dispensing onto the moving substrate.

The control of translation direction and speed of the substrate permits to obtain droplets aligned along straight lines or desired patterns. Moreover the volume variation of the drop reservoir allows one to dose the printed droplets with different volumes and sizes**, Figure 2.11**.

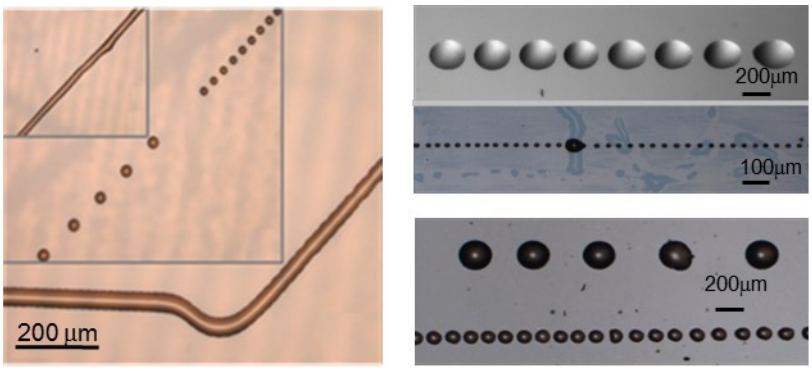


**Figure 2.11**: (a) Simple liquid patterns consisting of periodic separate droplets (diameters around 40 µm) and continuous straight line (width around 40 µm). (b) Separate droplets of different size and periods.

More complex patterns have been printed by mineral oil **Figure 2.12**, including a continuous and dotted Greek fret, a Greek fret with combined continuous and dotted lines, a dotted staircase including a non-orthogonal angle, a dotted staircase with smaller droplets (diameter, ~25 mm), in which the larger vertices were obtained by stopping the substrate during dispensing, and a dotted staircase with further droplets and small vertices (droplet diameter, ~30 mm).

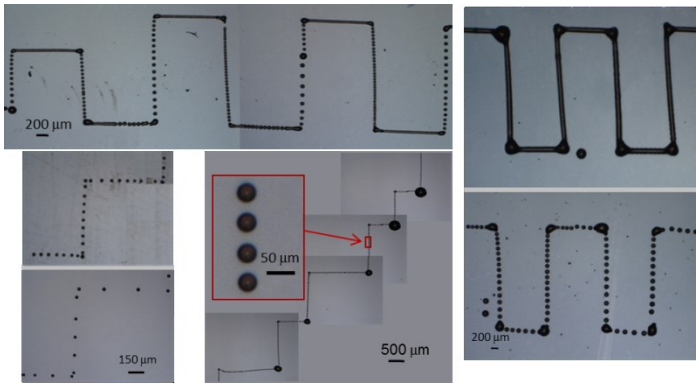


**Figure 2.12**: Examples of complex patterning applications: continuous and dotted patterned Greek fret printed by mineral oil; Staircase with smaller droplets (25 mm) printed with large vertices and dotted staircase with small vertices (droplet diameter, 30 mm).

It is important to point out that the technique is able to print droplets with much reduced dimensions by decreasing the volume of the drop reservoir (for example, after a certain number of shots). **Figure 2.13 (a)** presents optical microscope images of tiny droplets of oleic

acid dispensed from drop reservoirs of various volumes and dimensions (**Figure 2.13(b)**). The smallest dispensed droplets have volumes as low as ~3.6 al and radii of ~300 nm. The pyroelectrohydrodynamic dispenser presented here may find applications in the field of biochemical assays, because it can break up parent drops containing special materials dispersed into an oil phase. In fact, the compartmentalization of individual samples in droplets dispersed in an oil phase is becoming a powerful method for high-throughput assays in chemistry and biology[32,33]. For example, **Figure 2.14(a)** shows dispensed daughter droplets of carbon nanotubes dispersed in mineral oil, and **Figure 2.14 (b)** shows the daughter droplets of a sample of cell cultivation medium mixed with carboxyl oil. Additional experiments were performed to characterize the most relevant key attributes of the approach for different fluids (*Annex 2*). The revolutionary feature of the pyroelectrohydrodynamic dispenser would be to avoid the use of the drawing and delivery instruments traditionally used in biochemical protocols (that is, syringes, nozzels), thus making the assay procedures much easier and faster. In fact, the pyroelectrohydrodynamic dispenser would be used as a tool for breaking up parent drops that are standing on a surface into daughter droplets to be delivered directly to the desired substrate, where the droplets could be used as reaction confinements for biochemical assays and also for single-cell analysis[34,35].

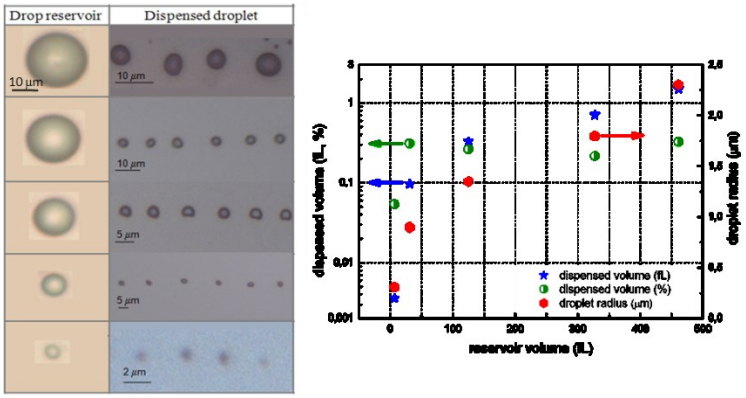


**Figure 2.13** : (a) Optical microscope images of different drop reservoirs and corresponding dispensed tiny nanoscale droplets of oleic acid. (b) Corresponding volume and radius values of the dispensed droplets versus those of the reservoir (the left y-scale is logarithmic).

This innovative technology reported here could open a new route in microfluidics and nanofluidics where manipulation, dispensing and dosage of nano-pico droplets is in high-demand in different fields of science and technology such as biotechnology, combinatory chemistry, pharmacology, deposition of inorganic, organic and biological matter. Different methods of pyro-EHD dispensing and patterning of nL-pL droplets can be performed by a

completely new approach without nozzles and electrodes but with much higher versatility to be integrated in microdevices and can be used for lab-on-a-fibre applications.

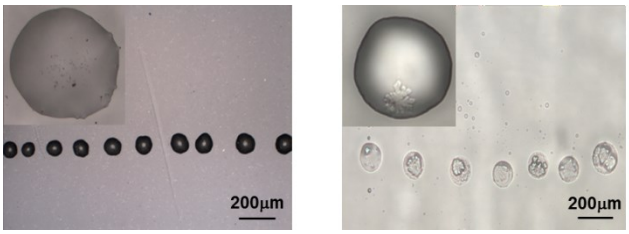


**Figure 2.14**: Daughter droplets of specific suspensions: optical microscope images of dispensed droplets containing carbon nanotubes dispersed in mineral oil (a) and cell cultivation medium mixed with oleic acid, where typical salt crystallization is visible (b).

## 2.7 Multi jets for the pyro-EHD dispenser

The ink-jet techniques have been explored for printing electrical and optical devices especially where organic components are involved or for producing arrays of proteins or nucleic acids[36]. Another class of inkjet liquid dispenser systems are based on EHD or electrospray. In the EHD approach a high voltage is applied between the dispensing nozzle and the receiving substrate[37]. The pyro-EHD ink-jet printing, if compared with standard EHD, has the advantages of being electrode-less and nozzle-less, and furthermore, as described in the previous sections, using this method liquid printing with attolitre drops resolution has been demonstrated. In the recent past many attempts have been made for developing liquid multi-jetting systems for highthroughput dispensing. Multiplexing of electrospray has been reached, in the planar mode, by fabricating an array of nozzles by laser etching[38] or by micro-machining of a hole-array[39]. However some problems arise for liquid multi-jets configurations in EHD systems due to the electric field edge-effects. Edge effects are caused by the mutual interaction between adjacent channels. Many efforts were spent to design and realize multi-jets for avoiding the electric field edges-effects[40,41]. The pyro-EHD dispenser could be used to overcome the aforesaid limitation, in fact it offers the ability to generate multi-jets from thin liquid films. Such an approach can be exploited for high throughput transfer of liquid nanodrops. In this section it is described how it is possible to create simultaneously multiple liquid jets avoiding the problem of the fabrication of multiple channels as occurs in classical EHD inkjet systems[40,41]. In fact, the method is able, under controlled conditions, to activate self-assembled multiple dispensing jets arranged in a spatially periodic array. It is well known that sufficiently strong field gradients can produce forces that overcome the surface tension in thin liquid films of dielectric media by inducing a specific instability[42]. Different experiments

can be found in the literature where such instability is exploited for fabricating ordered lateral structures from thin polymer films[43,44]. The mentioned techniques have been used as nano-lithography methods for patterning polymeric nanostructures with challenging achievements. However the activation of instabilities in the liquid film was obtained at very short distances (i.e. the upper electrode was very close to the liquid film) when compared to the liquid film thickness. If $t$ is the film thickness and $d$ the air gap between the film and the upper electrode, thus in all previous EHD lithography approaches the liquid instabilities were generated for very low values of the filling ratio $f = t/d$. In fact, the typical air gap values reported in previous works are in the range of 100 nm to 1000 nm[43]. In this section the same principle of liquid film instability is applied to higher air gap values (i.e. 240 mm to 360 mm) in order to induce the film instability for generating liquid multijets for high-throughput liquid dispensing.

The multi-jets system is relatively easy to accomplish: the set-up is very similar to those reported for the experiment of pyro-dispensing and is shown schematically in **Figure 2.15**. The pyro-EHD process is activated through the thermal stimulus and applied to a substrate spin coated with a viscous solution of PDMS. Various spinning speeds were adopted for characterizing the behavior of the multi-jets for different values of the filling ratio $f$, namely the ratio between the film thickness t and the air gap d. The multi-jets are visualized in situ by an optical set-up shown schematically in Figure 2.15. The light of a conventional blue collimated led (wavelength of 470 nm and beam power around 400 mW) illuminates the cross section of the multi-jets system while a high-speed digital CMOS video camera (pixel size 12x12 $\mu m^2$; frame rate of 500 frames $s^{-1}$ with 1280(H) x 1024(V) spatial resolution) is used for recording the process. A 5x microscope objective is adopted to image the multi-jets on the CMOS sensor.

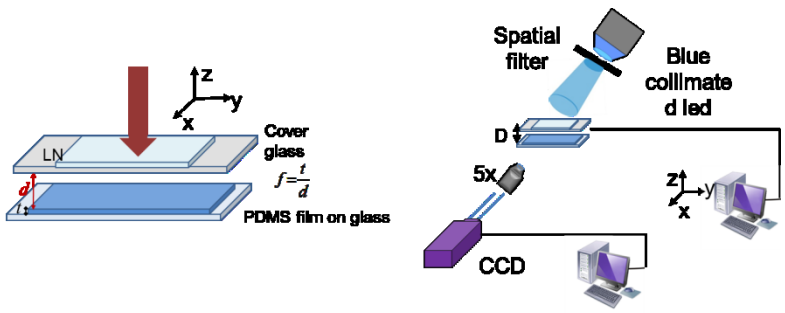


**Figure 2.15**: Schematic view of (a) the multi-jets system and (b) the visualization set-up.

Once generated the pyro-EHD effect the base-substrate is approached to the receiver-substrate until the beginning of the EHD process takes place, at a distance $d_a$ (activation distance). When the activation distance $d_a$ is reached, a liquid vertical instability of the reservoir layer is obtained and the liquid is ejected toward the receiver substrate. In fact, the pyro-EHD field is able to induce the surface film instability leading to the multiple jetting operation. A line of simultaneous liquid multi-jets develops on the edge of the base-substrate, dispensing continuously small amounts of liquid onto the receiver-substrate. The effect may be deactivated by increasing the base-receiver distance.

If the electric field is lowered, the EHD pressure is not sufficient to sustain the unstable process of the multiple and pulsed liquid jets cones. Nevertheless, it is interesting to note that the process is self-quenching since when the delivered liquid amount makes the film thinner the activation distance is above the threshold value of $d_a$, and consequentially the process inevitably stops. Thus, the unstable self-assembled liquid multi-jets cones pattern collapses.

### 2.8 Pyro-EHD process and instability of liquid film

The pyroelectric field generated by the LN plate induces two main instabilities into the PDMS dielectric layer.

First of all, an EHD-like surface instability arises inducing a sinusoidal surface undulation with a characteristic dominant wavelength[43,44] $\lambda$ that results basically from the competition between the destabilizing pyroelectric force and the surface tension of the polymer. The wavelength $\lambda$ is given by equation 4:

$$\lambda = 2\pi \sqrt{\frac{\gamma U}{\varepsilon_0 \varepsilon_p (\varepsilon_p - 1)^2}} E_p^{-\frac{3}{2}} \qquad (4)$$

with the dielectric permittivity of vacuum $\varepsilon_0$, the dielectric constant of the polymer $\varepsilon_p$, and the surface tension $\gamma$. For an applied voltage U, the electric field in the polymer layer is $E_p$. In fact, at sufficient high electric fields, the electrostatic stress overcomes the capillary surface tension. In this way the polymeric liquid film deforms, thus leading to the formation of multijets arranged periodically with period $\lambda$. By measuring the period of the self-assembled multi-jets, and using eq.4 it is possible to evaluate the electric field generated by the pyroelectric effect. The value of the resulting electric field is in agreement, with the typical electric field reported in the literature (Epyro = $10^7$ V $m^{-1}$) for the pyroelectric effect.

Moreover the above value is also in agreement with the value calculated numerically for pyro-EHD,10 i.e. $(2.7 < E_{pyro} < 5.5) \times 10^7$ V $m^{-1}$.

The polymer cones dispense liquid periodically till the electric field is active and the separation distance between the base and

receiver substrates is less than the activation distance. As shown in the experiments reported in the following the multiple-jetting system is studied in different configurations and exploited for parallel dispensing of polymer droplets, including multiphase materials.

## 2.9 Polymer multi jetting

In **Figure 2.16** are shown pictures of the self-assembled liquid jet cones corresponding to different film thickness t. The results clearly show that jets are aligned along the edge of the glass slide as a consequence of the typical accumulation of the polymer due to the spin-coating process. In fact the distance of activation is achieved firstly on the border. With the aim to fully characterize the multi-jets system different spinning speeds are used, thus forming liquid films with different thicknesses. The multiple jetting behavior was investigated for different spin speeds. The dynamic evolutions of the liquid pyro-EHD instabilities were analyzed.

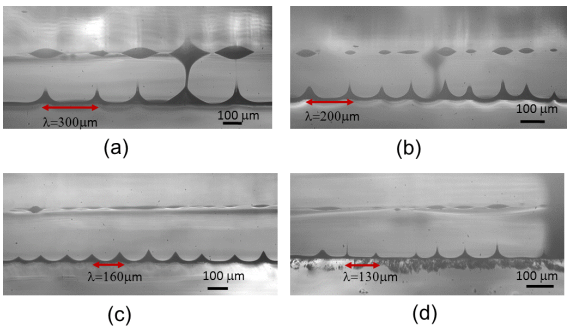


**Figure 2.16**: Different self-assembled liquid multi-jets obtained for various PDMS polymeric liquid films. (a) Film obtained at 3000 RPM (t = 9.8 mm); (b) at 4000 RPM (t = 7.5 mm); (c) at 5000 RPM (t = 6.2 mm); (d) at 6000 RPM (t = 4.8 mm). Changing the film thickness produces different spatial periods λ in the self-assembling arrangement.

The periodicity in the liquid film instability, the frequency of jetting dispensing and the volume of dispensed drops were measured for each thickness. In **Figure 2.17** are reported the experimental plots with data that allows to characterize the process. As we can observe, in the

first plot in **Figure 2.17 (a)** the activation distance $d_a$ and the film thickness t, are related each other. In fact the distance da changes as a function of the distance between the two plates (i.e. the air gap d). In **Fig. 17b** is shown the plot of the periodicity λ of the self-assembled multi-jets for the various experiments as a function of the filling ratio *f*. As expected the value of λ increases if the ratio between the film thickness and the air gap is increased too. That means that more dispensing jetting channels are obtained per unit length as the filling ratio decreases. On the contrary, the frequency rate of the liquid jetting process decreases when the filling ratio f increases as clearly reported in **Fig. 17c**.

It is important to point out that the technique would be able to deliver droplets with large size/volume by increasing the filling ratio. Such results can be inferred from the measurements reported in **Fig. 17d** where the estimated volumes of the dispensed drops are reported as a function of the filling ratio f. From the measurements it is also possible to estimate another interesting parameter that characterizes the process. In fact it is possible to dispense liquids with a time rate of from 400 pl $s^{-1}$ up to 4000 pl $s^{-1}$ for a unit length of 2 mm. Moreover, the process starts with a single jet cone and before the multi-jets configuration is reached some time is required. We believe the delay time for establishing the multijets is due to different reasons such as, non-uniformity of the electric field, variation of the film thickness and local variation in film viscosity.

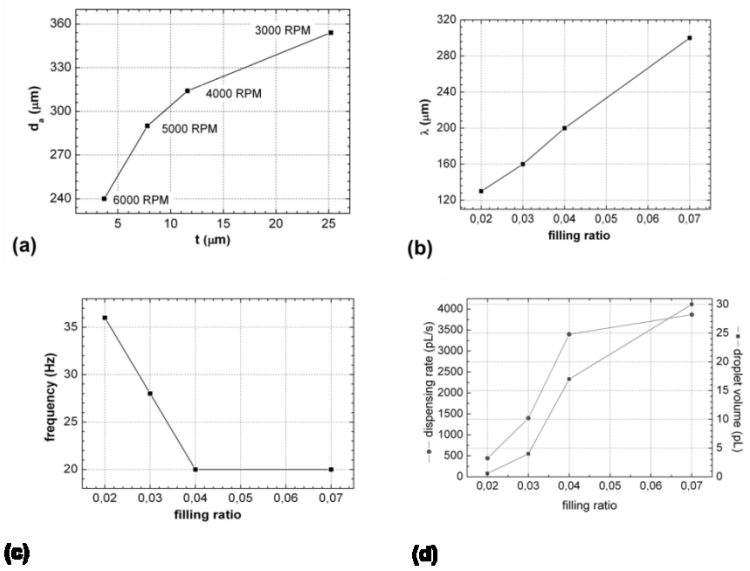


**Figure 2.17**: (a) The activation distance $d_a$ changes as a function of the film thicknesses t (the error for the horizontal axis is $\Delta t = 0.03$ μm while for the vertical axis is $\Delta d_a = \pm 5$ μm); (b) how the wavelength λ of the self-assembled multi-jets increases as the filling ratio increases; (c) the jetting frequency of the liquid multi-jetting process decreases by increasing the filling ratio and the droplet volume; (d) the dispensing rate as a function of the filling ratio.

## 2.10 Liquid delivering

Some results are shown here where the self-assembled multi-jets have been adopted for high-throughput delivering of polymer droplets from a liquid film. **Figure 2.18** shows the optical microscope image of liquid patterns printed with PDMS. Separate droplets and lines of different sizes were obtained on a cover glass mounted on a computer controlled x axis translation stage. The liquid has been dispensed simultaneously along many rows. The dispensed drops have sizes ranging between 30–70 μm. Along some of the rows the jet frequency is different thus explaining why along some channels the system prints lines instead of dots. The bad uniformity in the patterning is mainly due to some limitations of the experimental apparatus. In fact, if some experimental parameters, perfect parallelism between the plates and uniformity of the film thickness, would be fixed with more accuracy better results can be obtained.

Additional experiments were performed with a PDMS film reservoir mixed with multiwall carbon nanotubes (MWCNTs) (diameter 110–170 nm, length 5–9 μm, AldrichChemistry). The results clearly demonstrate that the system is able also to transfer the material dispersed into the film reservoir onto the receiving substrate. Anyway the results demonstrate that multiple channels can be activated and adopted for high-throughput liquid dispensing avoiding multiple nozzles configurations. The advantages of the proposed method, if compared to traditional EHD printing systems, are clear. The system developed represents a development of the previous pyro-nanodispenser extending the operation with multi-jets. The system exploits the polymer film EHD instabilities to this aim. In fact, the possibility of using the EHD instability for multiple jetting has never been explored up to now. In other words the system described represents the conjugation of the nano-dispenser with the EHD film instability giving rise to a novel multiple dispenser for high viscous polymers, like PDMS where nozzles cannot be adopted. The formation of multi-drops by a single liquid layer is possible. Even though the drops do not have exactly the same sizes it is very easy to collect drops simultaneously in a fast and high-throughput mode. Moreover it is possible to pattern dispersed multiphase materials with liquid multi-jets. The method is conveniently controlled and can be exploited for producing arrays of linear colloidal crystals[45], for personalized medicine[46] and for highthroughput liquid delivering in multiple channels by EHD inkjet avoiding the need for design and fabrication of the multiple channels.

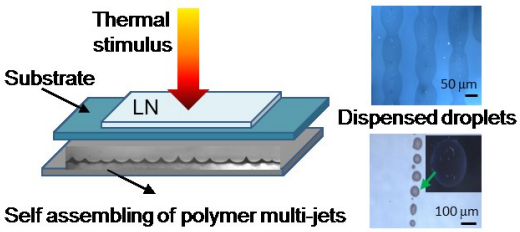


**Figure 2.18**: Optical microscope image of the activated polymer layer for multi-jetting applications. Dispensed printing lines of liquid PDMS with dispersed MWCNTs. The inset in the array of printed PDMS liquid nanodrops with dispersed MWCNTs shows a magnified image in dark-field of a single drop in which aggregates of CNTs are clearly distinguishable.

## 2.11 Fabrication of optical microlenses through the pyro-Dispenser

Microlenses are key components for optical devices and are widely applied in several application fields, such as communications, three-dimensional displays, optical data storage and photodetectors, playing a fundamental role in many optical systems. Numerous classes of microlenses exist, depending on the embedding technology and the specific applications. A large variety of fabrication processes have been developed for plastic/polymer based microlenses[47,48], such as embossing[49], soft-lithography[50], micro-molding[51], photolithography[52], electron beam lithography[53], laser assisted technique[48] and printing techniques[54]. In particular, these last techniques were advised as direct methods for high-quality and high-precision processes making the fabrication short time-consuming and cost-effective. Among the different printing technologies, the inkjet printing is attracting an increasing interest as single-step process with wide versatility in the definition of patterns, employable substrates and its capability for the rapid prototyping of optical structures[55]. The restrictions of this technology related to the ejection of high viscosity materials and the clogging troubles can be overcome by nozzle-free processes. Being nozzle-free, it can be applied also for high viscosity liquids greatly extending the fabrication capabilities of the conventional inkjet printing processes. In this section the fabrication of polymeric microlenses through the pyro-EHD approach is described. The pyro-electric field, as described in the previous section, is able to exert a hydrodynamic pressure onto the reservoir liquid, leading to the formation of a bridge or a conical tip. It is possible to define a critical distance D between the two plates of the set-up so that for distances $d < D$ a stable liquid bridge can be formed while for $d > D$ the dispensing process is activated. In this study, the formation of microlenses is investigated by the spontaneous breakdown of an unstable polymer liquid bridge created through the pyro-EHD effect, as illustrated in **Figure 2.19**. The set-up used for the experiment

consists of a microscope glass slide above which is placed the polymer drop reservoir, while a plate of LN crystal faces the base slide and drives the process. A computer controlled the translation of the target substrate, which is inserted between the facing plates and used to collect the microlenses produced in this nozzle-free process as previously described for the printing at high resolution. For this experiment polymer microlenses of poly(methyl methacrylate) (PMMA) were realized directly onto the target substrate. PMMA was chosen as polymeric material for its good optical and mechanical properties. The substrates were coated with a hydrophobic tetra-ethyl orthosilicate/1H,1H,2H,2H-perfluorodecyl-triethoxysilane (TEOS/PFTEOS) film which was spin-coated from a sol-gel solution. This layer induces a strong pinning of the printed droplets so minimizing their spreading on the substrates and reducing the solvent evaporation rate. The inks were prepared by dissolving 200 mg/mL of PMMA in pure NMethyl- 2-pyrrolidone (NMP) and different mixtures of toluene (TOL) and NMP (volume mixing ratios 7:3 and 6:4). Both the solvents are suitable to dissolve PMMA and have right volatility and surface tension properties for pyro-EHD processing (TOL: Tb = 110.6 °C, γ = 28.53 mN/m; NMP: Tb = 202 °C, γ = 40 mN/m).

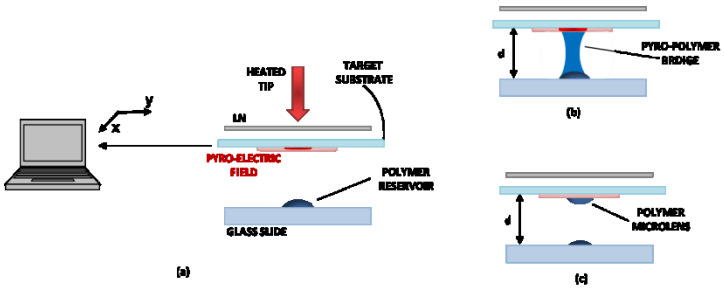


**Figure 2.19**: (a) Scheme of the printing system consisting of the LN plate, a heat source and a drop reservoir. Formation of the pyro-polymer bridge (b) and of the polymer microlens on the translating target substrate (c).

In **Figure 2.20**, 3-D plots of the optical microstructures obtained by microprofilometer analysis (Tencor P10, vertical resolution 10) with PMMA inks at different NMP:TOL mixing ratios (10:0, 7:3, 6:4) are reported. The focal length of this structures was estimated by using the following equation:

$$f = \frac{R}{n-1} \qquad (5)$$

with

$$R = \frac{h_L}{2} + \frac{r^2}{2h_L} \qquad (6)$$

where n is the refractive index of PMMA, $h_L$ is the height of the microlens and r is the base radius. The structures showed that the ink chemico-physical parameters, such as boiling point and surface tension, have a key role in the definition of the microstructure shape. In particular, as the toluene content increases (from 0% to 40%) the base diameter of the microstructure also increases (from 500 μm to 700 μm) while the height decreases (from 88 μm to 45 μm). As consequence, the focal properties are affected by those parameters. This effect can be explained in terms of the wetting properties of the ink-substrate system. In detail, the measured surface energy (SE) of the TEOS/PFTEOS substrate is about 17.08±0.17 mN/m while the surface tension (ST) of the inks are 37.99±0.24 mN/m, 33.53±0.14 mN/m and 32.45±0.13 mN/m for solvent mixing ratios 10:0, 7:3, 6:4, respectively. Since the wetting increases when the SE > ST, by increasing the content of toluene the surface tension decreases so increasing the splashing of the ink on the target substrate. This last effect is observable in the printed droplet shape whose diameter increases as the TOL content increases.

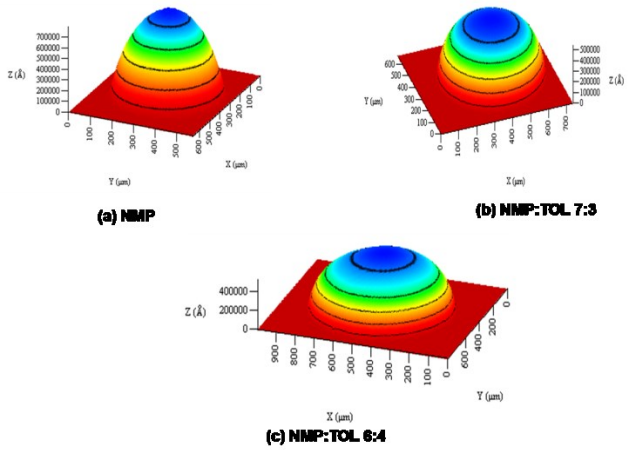


**Figure 2.20**: 3-D image of the microlens obtained printing PMMA dissolved in (a) pure NMP, (b) NMP:TOL 7:3 and (c) NNMP:TOL 6:4.

The microlenses were also analyzed by means of the Digital Holography (DH) set-up in transmission mode. This interferometer is schematically shown in **Figure 2.21**. Through the numerical managing of complex wavefronts it is possible to compute the amplitude and phase of the light transmitted by the sample.

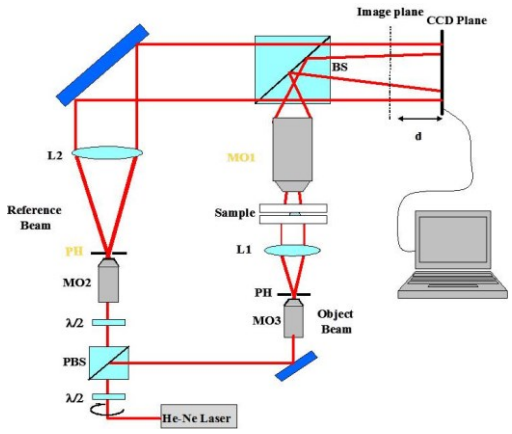


**Figure 2.21:** Set-up of the Digital Holographic Microscope (DHM).

As example, the digital hologram of the microlens obtained by employing PMMA dissolved in NMP:TOL 7:3 is showed in **Figure 2.22 (a)**. Intensity and phase maps of the object wavefront can be numerically reconstructed by the hologram. **Figure 2.22 (b)** shows the wrapped phase map modulus 2π, while **Figure 2.22 (c)** reports the corresponding unwrapped phase map that allows to calculate the wavefront curvature of the microlens. Moreover, the focal length can be estimated by fitting the unwrapped phase map Δφ(x,y) with a 2nd order polynomial function according to equation 7:

$$\Delta\Phi(x,y)=\frac{\pi}{\lambda}\left(\frac{x^2+y^2}{f}\right) \qquad (7)$$

The measurement gave a focal length value of about 1.6 mm, which is in according with the typical value obtained for the polymer structures from 7:3 NMP:TOL mixture by profilometric analysis.

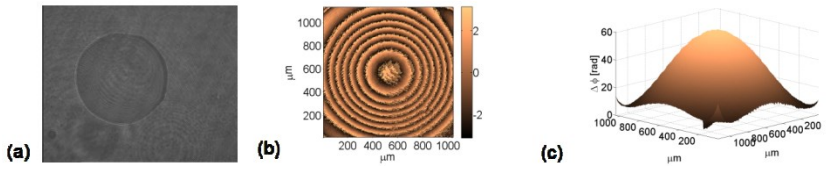


**Figure 2.22**: (a) Hologram, (b) wrapped phase map and (c) unwrapped phase map of the PMMA droplet prepared with volume mixing ratio 7:3.

The technology limits strongly depend on the viscosity of the polymeric material. Higher is the viscosity, higher is the diameter of the lenses. The distance between two contiguous lenses can be easily varied controlling the high precision scanning/translation stage of the target substrate.

A further investigation on the using of the Pyro-EHD approach for producing gradient-size microlens arrays was studied. In particular, the variation of the drop reservoir volume during the printing process allows the realization of microlenses with different size and focal length. This gradient-size microlens array, whose geometrical parameters are strictly correlated to the printed microlens number, were optically characterized. Arrays of microlenses were realized by using the Pyro-EHD process by applying a train of thermal pulses to the reservoir drop in a fixed position and controlling the receiving substrate. This technique represents a new route for an easy fabrication process of lens microarrays with decreasing focal length, which could find suitable application in optical communication or biomedicine. The schematic image of the printing process is reported in **Figure 2.23**. Controlling the experimental parameters and, in particular, the volume of the drop reservoir, microlens arrays could be simply produced over large areas reducing the cost of the fabrication line. In fact, it is possible to manufacture different polymeric microlenses with descending dimensions due to the reduction of the reservoir drop volume during the process. Once applied a thermal pulse the polymer drop reservoir forms a polymer bridge between the glass base and the target substrate. The subsequent breakdown of the liquid bridge leads to the fabrication of a polymer microlens onto the target substrate and in the same time collapsing the pyro-EHD bridge the reservoir drop is reduced in volume. Therefore applying a second thermal stimulus and varying the distance (d) as a function of the volume (V) the second polymer drop produced onto the target decreases in volume. Controlling the speed of the high precision scanning/translation stage the distance between two contiguous lenses can be easily controlled. Furthermore programming the heating source starting from a single polymer drop is possible to produce multiple microlenses along a single scanning line with different geometrical parameters having diminishing volume and focal length.

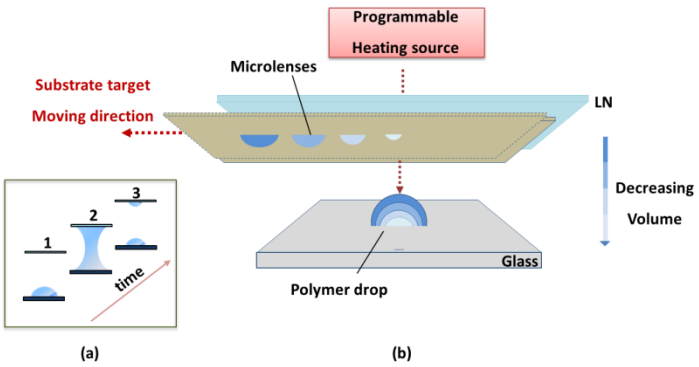


**Figure 2.23**: (a) Scheme of temporal evolution, formation of polymer lens through the breakdown of the Pyro-EHD bridge. (b) Experimental set-up for the fabrication of polymer microlenses having diminishing volume and focal length.

By using more polymer reservoir sources **Figure 2.24 (a)** this process would be useful for the contemporary production of nearby rows of a printed microlenses matrix **Figure 2.24 (b)** reducing the fabrication time.

The method described could represent a new route for mass production of microlenses matrix and, in order to prove the applicability of this polymer microstructures as optical lenses. The realized microstructures were analyzed by means of a mechanical profilometer to evaluate the dependence of the microstructure geometry from the chemico-physical parameters (boiling point, surface tension) of the constituent solvents of the ink.


**Figure 2.24**: (a) Multiple drop reservoirs to allow the parallel production of the rows of the matrix on the target substrate (b).

The results previously described in case of fabrication of single microlens show that all the realized microlenses have good optical quality and, in particular, that realized by employing NMP:TOL 7:3 solvent mixture have higher optical quality than respect to the others. Therefore, the choice of the right solvent mixture could improve the quality of the realized microlenses.

At a fixed drop reservoir volume, the possibility to realize microlenses with different focal length by considering the microlenses obtained by continuing the printing sequence and without varying the solvent mixture was investigated. Specifically using the same polymer solution from a single drop it is possible to fabricate a graded-size microlens array with different volumes and, as direct consequence, different structural profiles. The reduction of the base drop induces a reduction of the printed material on the target substrate. As a consequence, a reduction of the height and diameter and, hence, of the focal properties of the microlenses was obtained.

A statistical analysis, performed on ten arrays of microlenses, of both diameter and height of the microlenses as functions of the number of printed microlenses was summarized in **figure 2.25 (a)**. The analysis shows a reduction of about 60% of the diameter from the first and the tenth drop and a reduction of 70% for the corresponding heights. The detected variability of about 10% from one array to another could be ascribed to the solvent concentration of the

base drop. In **Figure 2.25 (b)** the relation between the corresponding height and diameter was reported. The founded relation between them was almost cubic with good agreement for all the solvent mixtures. The volume of these structures was estimated by approximating the microlens with spherical-cup shape by using the following equation:

$$V = \pi h^2 (a - \frac{h}{3})$$

$$a = \frac{h^2 + r^2}{2h}$$

where h is the height, r is the radius of the microlenses. The volume dependence as function of the printed structures is summarized in **Figure 2.26**. The relation between the volume and the number of microlenses is approximately cubic with a continuous variability of the geometrical parameters.

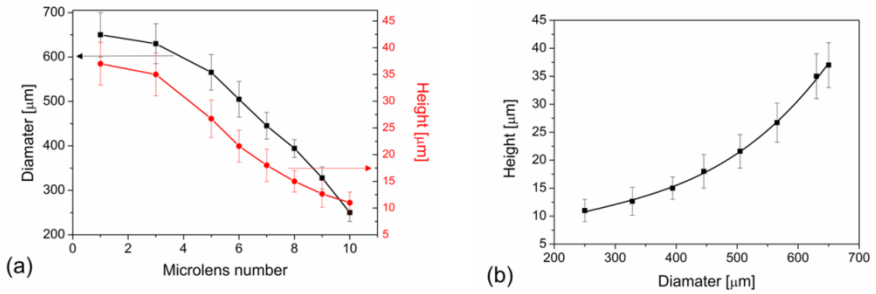


**Figure 2.25**: (a) Diameter and height as function of microlens number and (b) height as function of diameter of the printed microlenses.

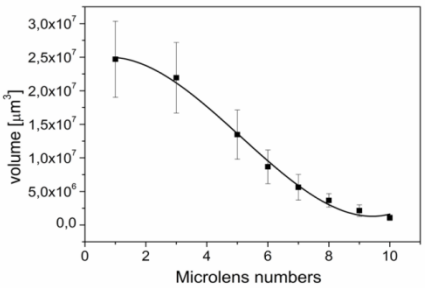


**Figure 2.26**: Volume as function of the number of printed microlenses.

In case of a microlenses array the first six microlenses characterized by a higher polymeric volume show a focal length that is almost constant. The subsequent four microlenses, characterized by a drop volume lower than $1x10^7 \mu m^3$, show a focal length decreasing of about 1.5 mm from the seventh to the last one, **Figure 2.27**. This effect can be explained in term of both the reservoir volume and the architecture of the printing system. A microlens sequence was realized starting from a unique drop reservoir, so each microlens was generated from

different base drop volumes. Higher base drop volume generates microlenses with higher volumes. Moreover, considering the printing schema, these structures were realized by keeping the substrate above the base drop so printing the microlenses upside down. Therefore, the microlens shape is a result of the balancing of three forces: substrate surface energy, ink surface tension and weight force. These forces act in different way for higher and lower volume drops, so inducing the different observed focal properties. As considering lower volumes microlens, the balancing of these forces produce a clear variation of the focal lengths which enables the realization of graded array of lenses.

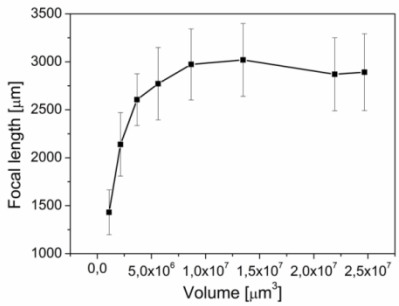


**Figure 2.27**: Focal length as function of the volume of printed microlenses.

As a result of the study conducted onto the microlenes fabrication it is possible to resume that the microstructure shape could be controlled by employing a pure solvent and solvent mixtures at different mixing ratios. It is clear how the chemicophysical parameters of the ink (boiling point, surface tension) properly combined with the surface energy of the substrate allow to modify the wetting of the printed droplet and, hence, the structure profile. Specifically, by varying the content of the solvents in the mixture it is possible to vary easily the geometrical parameters and the focal properties of the microstructures.

**References**


1) Casner, A. & Delville, J.-P.. *Phys. Rev. Lett.* 90, 144503 (2003).
2) de Heij, B. et al. *Anal Bioanal Chem.* 378, 119–122 (2004).
3) Ondarcuhu, T. et al. *Eur. Phys. J. Special Topics* 166, 15–20 (2009).
4) Cherney, L. T. *J. Fluid Mech.* 378, 167–196 (1999).
5) Collins, R. T. et al. *Nature Phys.* 4, 149–154 (2008).
6) Taylor, G. I. *Proc. R. Soc. Lond. A* 280, 383–397 (1964).
7) Park, J-U. et al. *Nature Mater.* 6, 782–789 (2007).
8) Park, J-U. et al. *Nano Lett.* 8, 4210–4216 (2008).
9) Poon, H. F., Saville, D. A. & Aksay, I. A. *Appl. Phys. Lett.*93, 133114 (2008).
10) Chen, C.-H., Saville, D. A. & Aksay, I. A. *Appl. Phys. Lett.* 89, 124103 (2006).
11) Chen, A. U. & Basaran, O. A. *Phys. Fluids* 14, L1–L4 (2002).
12) Miccio, L. et al. *Opt. Lett.* 34, 1075–1077 (2009).
13) Ahmed, R. & Jones, T. B. *J. Micromech. Microeng.* 17, 1052–1058 (2007).
14) Ferraro et al. *Nat. Nanotech.* 5, 429-435 (2010).
15) Rosenblum, B., Bräunlich, P., Carrico, J. P. *Appl. Phys. Lett.* 25 (1974).
16) Gañán-Calvo, A. M. *Phys. Rev. Lett.* 98 (2007).
17) Maeda, N.; Israelachvili, J.N.; Kohonen, M.M. *PNAS* 100 (2003).
18) Whitesides, G. M. *Nature* 442, 368 (2006).
19) Köhler J. M. & Henkel, T. *Appl. Microbiol. Biotechnol.* 69, 113 (2005).
20) Huebner, A. et al. *Lab Chip* 8, 1244 (2008).
21) Sessoms, D. A. et al. *Phys. Rev. E* 80, 016317 (2009).
22) Matteini, P. et al. *J. Mater. Chem. B* 1, 1096 (2013).
23) Ratto, F. et al. *Proc. SPIE* 7910, 5954853 (2011).
24) Notz, P. K. & Basaran, O. A. *J. Colloid Interface Sci.* 213, 218 (1999).
25) Mercatelli, R. et al. *Appl. Phys. Lett.* 99, 131113 (2011).
26) Butenko, A. V. *J. Appl. Phys.* 108, 044106 (2010).
27) Lippmann, M.G. *Ann. Chim. Phys.* 5, 494 (1875).
28) Colgate E. & Matsumoto, H. *J. Vac. Sci. Technol. A* 8, 3625 (1990).
29) Mugele, F. & Baret, J.-C. *J. Phys.: Condens. Matter* 17, R705 (2005).
30) Beunis, F. et al. *Appl. Phys. Lett.* 91, 182911 (2007).
31) Moon, H. et al. *J. Appl. Phys.* 92, 4080 (2002).
32) Taly, V., Kelly, B. T. & Griffiths, A. D. *ChemBioChem* 8, 263–272 (2007).
33) Griffiths, A. D. & Tawfik, D. S. *Trends Biotechnol.* 24, 9 (2006).

34) Basaran, O. *AICHE J.* 48, 9 (2002).
35) Song, H., Chen, D. L. and Ismagilov, F*Angew. Chem. Int. Ed.* 45, 7336–7356 (2006).
36) Calvert, P. *Chem. Mater.* 13, 3299–3305 (2001).
37) Kuil, M. E. et al. Marijnissen, *Biotechnol. J.* 1, 969–975 (2006).
38) Deng, W. et al. *J. Aerosol Sci.* 40, 907–918 (2009).
39) Bocanegra, R. *J. Aerosol Sci.* 36, 1387–1399 (2005).
40) Tran, S. B. Q. et al. *J. Electrost.* 68, 138–144 (2010).
41) Kelly, R. T. et al. *Anal. Chem.* 80, 5660–5665 (2008).
42) Landau, L. D. et al. Electrodynamics of Continuous Media, Pergamon, Oxford, (1984).
43) Scaffer, E. et al. *Nature*, 403, 874–877 (2000).
44) Voicu, N. E., Harkema S. and Steiner, U. *Adv. Funct. Mater.* 16, 926 (2006).
45) Poon, H. F. et al. *Appl. Phys. Lett.* 93, 133114 (2008).
46) Elele, E., Shen Y. and Khusid, B. *Appl. Phys. Lett.* 97, 233501 (2010).
47) Ottevaere, H. et al. *J. Opt. A: Pure Appl. Opt.* 4, S22-S28 (2002).
48) He, M. et al. *J.Opt. A: Pure Appl. Opt.* 6, 94 -97 (2004).
49) Chang, C.Y., Yang, S.Y., Sheh, J.L. *Microsyst Technol.* 12, 754-759 (2006).
50) Shi, J. et al. *Microfluid Nanofluid* 9, 313–318 (2010).
51) Zhu, J.-h., Shi, J.-xia, Wang, Y., He, P.-sheng. *Chin. J. Chem. Phys.* 19, 443-446 (2006).
52) Schilling, A., Merz, R., Ossmann, C., Herzig, H. P. *Opt Eng* 9, 2171–6 (2000).
53) Cheong, W., Yuan, L., Koudriachov, V., Yu, W. *Opt. Express* 10, 586-590 (2002).
54) Grimaldi, I.A. *Journal of Applied Polymer Science* 122, 3637-3643 (2011).
55) Villani, F. Opt. Lett. 35, 3333-3335 (2010).

# Chapter 3

## 3.1 Pyro-electrohydrodynamic (EHD) lithography for fabrication of polymer 3D microstructures

The capacity of soft materials to self-organize into regular patterns has been long recognized[1-3] and a lot of the existing procedures identify the precedence of nature, which uses the same parsimonious principles to make elaborate micropatterns such as exoskeletons[4] and photonic crystals[5,6].

Not all of the rich patterns generated spontaneously by physical forces are long-lived, however, which may limit opportunities for exploiting them in technologies. Fluids are particularly apt to display transient patterned instabilities that are gone in an instant. A wide variety of lithographic techniques have been developed for fabricating complex three-dimensional (3D) structures[7-9] starting from a fluid polymer, such as soft lithography[10] or capillary-force lithography[11]. In the first case soft lithography allows one to develop lab-on-chip devices with applications ranging from organic light emitting diode to biology and biochemistry[12] while capillary-force lithography is able to nicely pattern polymers at nano-/microscale, but with a very low aspect ratio, in a single step and avoiding the use of external forces. Other approaches generate self-patterned structures by using destabilizing forces produced by electric fields, namely electrohydrodynamic (EHD) lithography[13]. In EHD lithography, amazing polymeric patterns have been reported, demonstrating the possibility of controlling the process with high accuracy. This method appears suitable only for a few types of periodic patterns having a relatively low aspect ratio (i.e., pillars, dots, and lines). The EHD lithography is usually performed at temperatures above the glass transition of the polymer film [typically polystyrene or poly (methyl methacrylate)], obtaining permanent microstructures by slow annealing and successive cooling, taking hours[14]. In general, the hydrodynamic techniques produce steady-state structures resulting from the equilibrium state of a specific fluidic effect preventing the achievement of the expected final steady state.

In this chapter a new approach consisting in “rapid-curing” temporary structures, which evolve continuously under specific fluidic instabilities, by a fast heating procedure, is presented. The interesting aspect of this approach is that it gives access to very intriguing fluid shapes, occurring in unsteady fluid physics at nanoscale, which could be very useful in modern science. In fact, as investigated recently, the breakup of viscoelastic filaments passes through the formation of temporary pearls interconnected by a thin thread, the so-called beads-on-a-string (BOAS) structures[15,16]. In the studies and the experiments reported in the

following is furnished a detailed description of how is possible to mimic nature and produce in a controlled way liquid instabilities, stopping their "evolution history". Controlling liquid evolution in time could led to "freeze" nanofluidic instabilities in polymers as occurs for the iced fountain's jets or the waterfalls in a cold winter.

The approach studied exploits instabilities and self-assembling of polymeric liquids for fabricating single or arrays of complex high aspect-ratio 3D microstructures[17]. Liquid instabilities are first driven via EHD pressure and then quickly cured to obtain permanent 3D micro-structures, by the same thermal treatment, paving the way to a previously undescribed paradigm in fabrication of 3D polymer microstructures. In the experiment reported in the chapter' sections the fabrication of polymer wires, needles, pillars, cones, or microspheres is reported. The polymer structure functionalization through nanoparticles and fluorochrome is also shown, and practical proofs of its use in photonics are presented. These micro-structures can be used as, for example, one-dimensional arrays of optical resonators, with optical properties tunable by mixing fluorescent particles into the liquid polymer. Other 'frozen' instabilities that may be created this way include 'axicons': conical structures with a needle tip at their apex, which might be used as elements for optical tweezers with a large depth of focus, or as the tips of near-field optical microscopes[18], or a stretchable tunable microresonator for detecting or sensing applications[19].

### 3.2 Design and Working Principle of the Technique

The polymer used in the experiments is the polydimethylsiloxane (PDMS), a polymer that can commonly be adopted in EHD lithography or in the electro-spinning processes[20-22]. It is important to note that EHD or electrospinning has never been used for building up 3D microstructures such as those reported here, having high aspect ratios compared to those obtained through EHD or capillary-force lithography[11,13]. Overall as a difference with all the conventional experiment based on the EHD effect this new concept of lithography is driven by the pyro-electric approach in a non-contact and highly flexible modality.

In the method investigated in the following, the air–liquid interface is subjected to an EHD field able to increase the dominant instability, among the natural spectrum of capillary surface waves, at room temperature, without a preliminary annealing process[13]. The polymeric permanent structures fabricated are generated by rapid cross- linking. This method allows to reduce the overall process duration from hours, required for the glass transition, down to seconds. Furthermore the combination of high viscosity[15] and rapid cross-linking of PDMS

allows us to fabricate structures with aspect ratios extraordinary higher, up to three orders of magnitude, compared to those reported in literature[11-14,23]. In fact, the typical aspect-ratio values reported in previous works are in the range of 0.29–0.83, whereas up to 186 is reached through this approach.

The experimental configuration adopted for the experiments is very similar to those reported in chapter 2. In fact, it consists basically of a glass slide supporting a sessile nanodrop as liquid reservoir, facing a lithium niobate (LN) substrate at distance D. The pyro-electric field, generated by a temperature gradient, is able to exert an EHD force on the liquid PDMS creating a liquid bridge across the two substrates, as shown in **Figure 3.1**. The bridge drains to a very narrow column that then bunches into 'beads on a string'. A hot-air jet cures the structure within seconds, before it can fragment. The result is a string of linked, transparent, spherical or lenticular beads just a few or a few tens of micrometres across. In this way the EHD pressure and fluid dynamics cause liquid depletion from the bridge with the consequent formation of various temporary liquid silhouettes[15] having the inevitable fate toward the collapsing point.

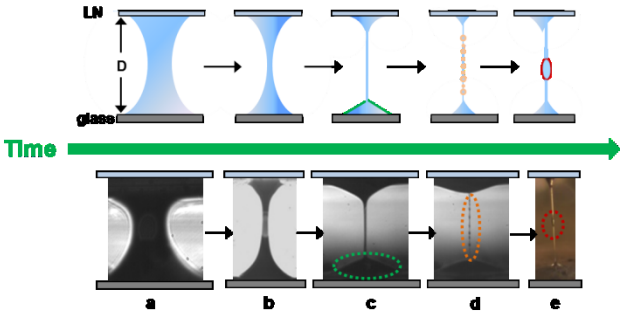


**Figure 3.1**: Evolution in time of liquid depletion, the polymer bridge of frame (a) drains in time to a very narrow column (b-c) that then bunches into beads on a string (d), this beads could coalesce one each other in order to get a single polymer bead (e)

### 3.3 Experimental procedure of fabrication by pyro-EHD

The dynamic evolutions were observed by a high-speed complementary metal oxide semiconductor (CMOS) camera. The illumination equipment consisted of a conventional blue collimated led (wavelength of 470 nm and beam power around 400 mW) equipped with a neutral density filter. A 5× microscope objective was used for visualizing the PDMS instabilities onto the CMOS camera. The liquid instability generated by the pyro-electric effect may reveal different evolutions and scenarios that were possible to draw and understand by means of a systematic experimental investigation. In particular, depending on some

relevant parameters, such as the amount of liquid (i.e. volume of the patterned reservoir or film thickness), the liquid viscosity, the electric field strength and the *d* value, three main *scenarios*, corresponding to the early stages of the pyro-EHD process, may occur, as illustrated in **Tab.1**.

| Scenario type | Conditions | Kinetics |
|---|---|---|
| Scenario (1) | • $d = d_c$ | Stable liquid bridge |
| Scenario (2) | • $d = d_{act}$<br>• rich reservoir | Average instability |
| Scenario (3) | • $d = d_{act}$<br>• poor reservoir | High instability |

**Tab.1**: List of scenarios developing during the pyro-EHD instability.

To this aim two characteristic values are defined here for the distance *d* between the base and the receiver: the "activation distance" $d_{act}$, corresponding to the maximum distance at which a pyro-EHD interaction establishes and over which such interaction is negligible, and the "critical distance" $d_c$, corresponding to the formation of a stable liquid bridge[24], where $d_c < d_{act}$. When $d_c \leq d \leq d_{act}$ and the LN wafer is stimulated thermally, the pyro-EHD forces interact with the liquid reservoir by attracting the liquid, according to the well known EHD effect[25]. When the liquid reservoir is a thin layer or a distribution of tiny strips, an amplification of the surface waves occurs under the action of the pyroelectric field, an effect that is widely used for the EHD lithography applications, as mentioned previously[13,26]. In scenario (1) $d = d_c$ and a stationary liquid configuration builds up, corresponding to the direct formation of stable liquid bridges with symmetric and homogenous morphology. The scenario (2) corresponds to a transient state of elongated liquid jets with intermittent formation of thin bridges, due to the relatively high amount of material in the reservoir (large volume or thick film). Shortening the distance *d* leads to the formation of stable liquid bridges. The scenario (3) consists of a more unstable and transient configuration where high frequency shooting liquid jets are generated. This phenomenon occurs for quite thin layers of liquid (film of PDMS spinned @ 6000 RPM with thickness around 250 μm). In this configuration stable liquid bridges establish for a shorter distance *d*, down to values approaching the critical one $d_c$. It is important to note that the early stages of both scenarios (2) and (3) are characterized

by the typical periodic deformation of the liquid layer, that we call here *horizontal instability*, with a characteristic dominant wavelength $\lambda$ [13] given by

$$\lambda = 2\pi \sqrt{\frac{2\gamma}{-\frac{\partial p}{\partial h}}} \qquad (1)$$

This results from the competition between the destabilizing force and the surface tension. $\gamma$ is the liquid surface tension, $p$ is the destabilizing pressure which scales with the square of the electric field in the polymer layer[26] and $h$ is the film thickness.

Another interesting configuration, that we call here sub-scenario (4), can evolve from scenarios (2) or (3), when the material dispensed by the jets accumulates on the substrate and the PDMS is partially cured due to the thermal source applied during the evolving process that increases the PDMS viscoelasticity. Such conditions favour the formation of unstable bridges, as a result of the wave maxima pinning the top surface, which tend to grow thinner and eventually collapse when the electric field diminishes or vanishes, according to what we call here *vertical instability* and that we exploit to obtain the photonics structures. It is noteworthy that even the stable bridge corresponding to scenario (1) may evolve into the sub-scenario (4) as soon as it becomes unstable due to the variation of specific parameters such as the distance $d$ or the temperature gradient. In this way the initially thick bridge grows thinner due to the depletion (drainage) of the liquid towards the base and the substrate according to the capillary forces which favour the liquid to slide towards regions with lower radius of curvature, namely the flat area of the substrate[27]. The liquid sliding is also driven by the well known thermocapillary forces generated by thermal gradients[28], and by the pyroelectric field that continuously drags the liquid from the reservoir. During the liquid depletion the bridge diameter reduces down to a dimension that favours the formation of the typical BOAS structure[29].

### 3.4 High aspect ratio micron-sized structures formation

The experiment performed and reported in the following section demonstrate how is possible to freeze the BOAS and other microstructures by a rapid-curing approach avoiding the final collapsing and breaking of the nanofluidic silhouette. Different experimental configurations were adopted; The micro-sized structures of **Figures 3.2(a-c)** are high aspect ratio structures

fabricated with the "packaged" configuration. The packaged configuration had the base and the receiver joined together at a fixed distance *d* ranging from 300 to 500 μm through appropriate thin spacers. For the fabrication of this structures PDMS strips of about 10 μm thickness are confined onto the edge of the base spin coating the sample @ 3000 RPM for 1 min and successive appropriate accumulation on the edge of the glass slide. The LN wafer, lid of the package, was stimulated thermally by the hot-air-jet for 15 s @ 150 °C and successively the package was turned around to put the LN wafer in contact with a cold surface in order to induce a rapid temperature gradient. The package was then observed by an optical microscope. While the nanofluidic instability took place with continuous formation of BOAS, the same hot-air-jet was used for curing such structures (typically in about 60 s @ 200 °C). This is a typical case where the same thermal source was used for stimulating the pyroelectric effect as well as for the rapid curing of the structures. In this case the structures were formed by the combination of the horizontal and vertical pyro-EHD instabilities. The partial curing sustained by the PDMS during the first hot-air-jet (used as pyroelectric stimulus) appears to favour the formation of BOAS within the subscenario (4). One more interesting aspect is the possibility of regulating the position of the beads along the wire prior to the rapid curing of the structure, by modulating appropriately the pyroelectric field.

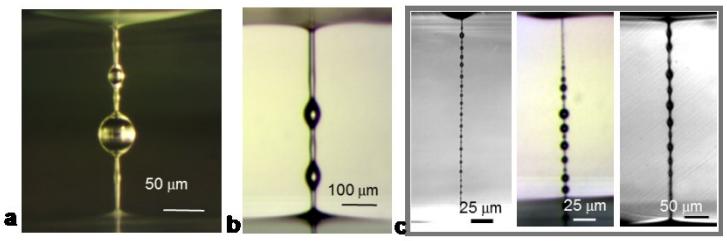


**Figure 3.2**: High aspect ratio polymer microstructures

The “package” was then observed by an optical microscope. Although the nanofluidic instability took place with continuous formation of BOAS, the same hot-air jet was used for curing such structures. In this case the structures were formed by the combination of what we named the horizontal and vertical pyro-EHD instabilities. The partial curing sustained by the PDMS during the first hot-air jet (used as pyroelectric stimulus) appears to favour the formation of BOAS within subscenario (4).

The formation and the successive curing process can be monitored in real time. In fact, it can be clearly visible that, by activating the cure process during the formation of the BOAS, it is possible to fix the structure, avoiding their collapse. In this case the activation of the processes leading to the formation of the microstructures and its subsequent fast curing was obtained

using the spotlight of a 150-W halogen lamp focused onto the microstructures by a parabolic mirror. The temperature of the curing process was about 130 °C.

With the aim to assure that the curing process was fully accomplished, some tests were performed. As shown in **Figure 3.3 (a)** a wire with beads can be elongated up to about 100% of its length. A further example is shown in **Figure. 3.5 (b)** where a cured wire with multiple beads is also elongated and then compressed to demonstrate the complete curing of the structure without breaking.

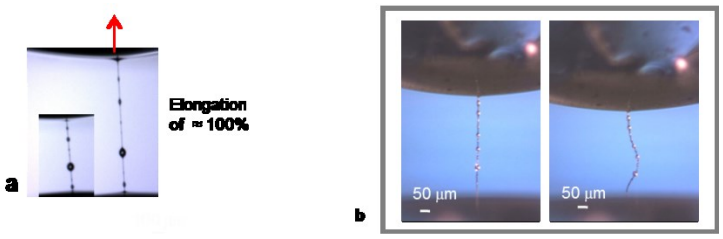


**Figure 3.3**: Curing test applied to polymer microstructures, (a) elongation of 100% and (b) compression of cured polymer beads on a string.

In **Figure. 3.4 (a-b)** the schematic view of the PDMS patterns (dots and strips) used as reservoirs are shown. **Figure 3.4 (c-d)** shows the top and side microscope images of permanent symmetric bridges. The microsized structures displayed in **Figure 3.4 (c,d-h)** are formed using the packaged configuration with d ranging from 150 to 500 µm and printed separate drops of PDMS as reservoirs. The figures present the top and the side microscope images of permanent symmetric bridges with different aspect ratios, obtained through the rapid curing of the stationary state corresponding to scenario (1). The sample having the LN above the package and in direct contact with the thermal source was heated onto a hot plate at 150 °C for 120 s, activating the pyro-EHD effect and realizing the rapid curing. Two-dimensional arrays of wired structures, where the PDMS included dispersed multiwalled carbon nanotubes (MWCNTs), are reported in **Figure 3.4 (e)**. PDMS, diluted with hexane (mixing ratio 3∶1) and with dispersed carbon nanotubes (multiwalled, diameter 110–170 nm, length 5–9 µm, Aldrich Chemistry), was patterned as an array of separate drops. In this case the hot-air jet was used for triggering the nanofluidic pyro-EHD instability as well as for the rapid curing of the structures, in the same conditions described in **Figure. 1**. The use of MWCNTs makes the curing process faster when compared to the rapid cross-linking using just pure PDMS. The experimental characterization of the curing speed shows an increase of about 25%. This improvement was estimated by testing a sequence of drops with and without dispersed carbon nanotubes. The drops were placed on a glass side and were heated by the hot-air jet for a specific time untill the curing stage was checked. In this case a hot-air jet was

used for triggering the nanofluidic pyro-EHD instability as well as for the rapid curing of the structures. Conical structures with needle tips, obtained by rapid curing of the Taylor's cone, are shown in **Figure 3.4 (f)**. Essentially such structures consist of two facing cones with different apex angles connected by a thin wire. **Figure 3.4 (f)** shows the conical structures (Taylor's cone) with and without the needle tip formed onto the receiving substrate obtained by unwrapping the package configuration of Figure 3.4 (e).

Moreover **Figure 3.4 (g)** reports a typical multiple, self-arranged, jetting effect in a liquid film, from which multiple periodic structures can be fabricated, such as the 2D array of columns. **Figure 3.4 (h-j)** show a linear array of cured BOAS and wired structures, respectively. **Figure 3.4 (j)** shows well-ordered high aspect-ratio structures fabricated with the separate configuration, in which the base and the receiver were mounted onto two separate vertical translation stages in order to change finely the distance d. The separate configuration provides higher flexibility and thus enables the implementation of a wider variety of test experiments, whereas the packaged one is more compact. The LN wafer was stimulated by the hot tip and, after about 3 s, the typical multiple jetting of PDMS began and was rapid-cured by the hot-air jet applied at 200 °C for 60 s.

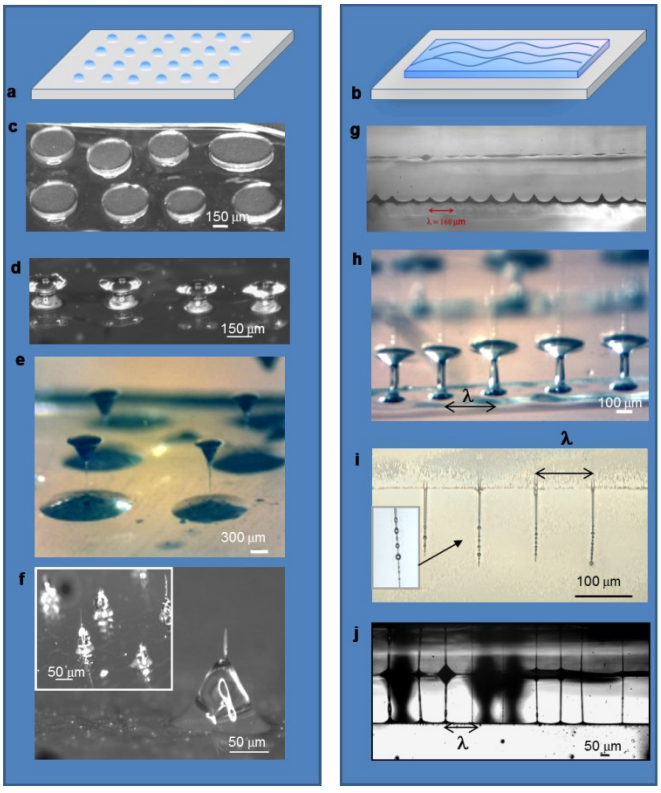


**Figure 3.4**: Schematic of polymeric array microstructures obtained starting from separate polymer drops (left column) or from a polymer film (right column).

It is important to note that, compared to electrospinning studies[22] where BOAS are generated and controlled, the pyro-EHD approach is based onto a process evolving under the Rayleigh instability but with a nonconstant Deborah number due to variation of the viscoelastic properties of the PDMS during the process. In fact, differently from other electrospinning methods, our approach uses a thermal load that changes the liquid properties during the process, thus leading to different shapes of the liquid jet from simple uniform wires to BOAS structures.

The wires could be used as potential optical waveguides similar to optical fibers for collecting or distributing light signals in lab-on-a-chip optofluidic devices or also as optical tips able to deliver or collect light in scanning probe microscopes.

## 3.5 Applications of Rapid Cured PDMS Microstructures

### 3.5.1 Micro –axicons as optical tweezers by Bessel beams

The cone of **Figure 3.5** is a valuable optical lens, named *axicon*. A layer of PDMS polymer diluted with hexane (mixing ratio3:1PDMS/hexane) was spin coated on a microscope slide at 3000 RPM for 1minute. Thin spacers of 100 μm were glued on the edges of the base to superimpose the LN plate at a fixed distance. The sample with the film of PDMS is then placed on a hot-plate at a temperature of 115 °C for 10 min, generating a series of PDMS cones. By heating the sample, was developed the film instability and the rapid curing process of the polymer has generated the formation of microaxicon structure. The lid of LN is then removed, leaving the microaxicon deposited on glass.

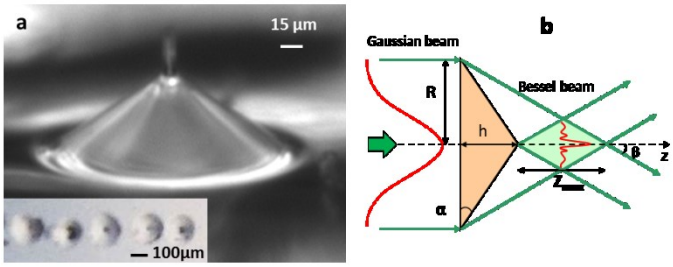


**Figure 3.5**: Side view of polymeric micro-axicon (a) obtained by pyro-EHD effect onto a glass substrate and schematic of the Bessel beam produced by the lens.

An axicon is able to produce Bessel beams having high depth of focus when compared to focused Gaussian beams obtained by high numerical aperture microscope objectives with high

efficiency. This micro-optics can be made from refractive, reflective or diffractive elements. The angle $\beta$ between the refracted ray and the normal to the axicon base is given by:

$$\beta = \arcsin(n\sin\alpha) - \alpha \qquad (2)$$

where n=1.43 in case of the PDMS axicons fabricated in this work. The corresponding depth of focus $Z_{max}$ is given by[30]:

$$Z_{\max} = R(\cot\beta - \tan\alpha) = 240\mu m \qquad (3)$$

According to the axicon properties, the beam profile of the incoming Gaussian beam becomes Besselian at least within the range of $Z_{max}$[31-33]. In case $z \leq Z_{max}$ the radius $r_0$ of the Bessel beam core, defined as the radial distance from the core to the first intensity minimum, is given by[36]:

$$r_0 = \frac{2.405}{k\sin\beta} \qquad (4)$$

where the factor 2.405 is derived from the first root of the zeroth-order Bessel function and $k=2\pi/\lambda$ is the wave number. Moreover, the distance $\Delta\rho$ between two neighboring Bessel rings (the *ring spacing*) is[34]:

$$\Delta\rho = \frac{\lambda}{2\sin\beta} \qquad (5)$$

The base diameter of the PDMS axicon used here is about 200 μm (R≈100μm) while the base angle is α=33°, $Z_{max}$=240 μm and $r_0$ is about 0.6 μm. Table 2 summarizes the characteristics of the PDMS microaxicon used in the experiments reported in the following.

| | |
|---|---|
| Base diameter (μm) | 200 |
| Base angle α (°) | 33 |
| Refractive index | 1.43 |
| Height (μm) | 65 |

| | |
|---|---|
| Refraction angle β (°) | 18 |
| Depth of focus (μm) | 240 |
| Bessel core diameter (μm) | 1.26 |
| Bessel ring spacing (μm) | 0.83 |

**Tab. 2**: Characteristics of the polymer micro-axicon

The properties of the Bessel beam furnish a clear advantage for optical trapping (i.e., for particles trapping by the light forces) compared to the use of microscope objectives. In fact, an axicon is very useful as optical tweezer for trapping and sorting micro-particles or biological cells. Small dimensions of axicons could make these elements suitable for embedding them into lab-on-a chip devices, to image or to trap microobjects in microfluidic channels, unrealizable things with cumbersome microscope objectives having limited depth of field. In this section is reported an optical tweezers experiment demonstrating application of the rapid cured PDMS axicons for single particle trapping and for high depth-of-focus simultaneous multiple trapping in different planes along the z direction of six 10-μm-sized latex particles. **Figure 3.6** displays the intensity profile of the beam in (*a*) along both *x* (*b*) and *y* (*c*) transverse directions in a plane at about 800 μm from the apex of the axicon. The profiles clearly follow a Bessel function of the type sin2*x*/*x*2, with a full width at half maximum of 1.9 μm along both *x* and *y*. The reconstructed intensity map is displayed as inset. The central maximum, i.e. the 'core' of the beam, has a measured diameter of about 3 $\mu$m and the resulting ring spacing (the distance between two maxima) is a couple of microns, in agreement with the theoretical values.

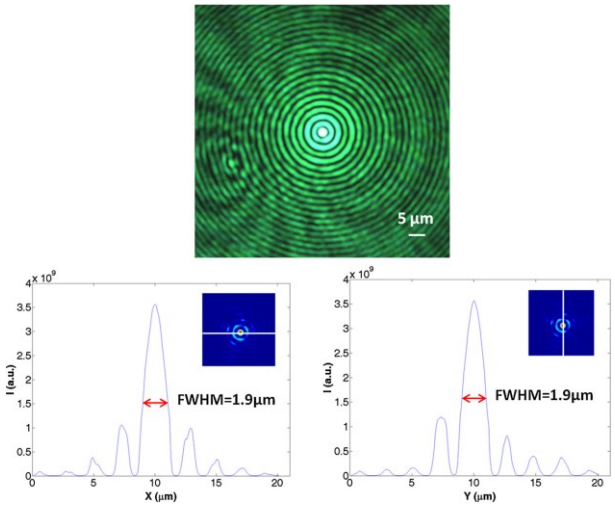


**Figure 3.6**: (a) Bessel beam in a plane at about 800 µm from the axicon apex. (b), (c) Transverse intensity profile of the beam along (b) x and (c) y axes, following a sin2x/x2 Bessel function. Inset: reconstructed intensity map of the beam.

A digital holography (DH) technique[35], based on the use of a Mac-Zehnder interferometer, was used for characterizing the PDMS axicon. The experimental set-up consists of a Mach-Zehnder interferometer arranged in a transmission configuration, as depicted in **Figure 3.7** below. The source is a continuous-wave solid state laser emitting at □=532 nm. The laser beam is divided in two by a polarizing cube beam splitter. The object beam traverses the PDMS microaxicon and is imaged by a 5× microscope objective onto a CCD camera. The reference beam, opportunely expanded and with the same polarization of the object one, is recombined with it thanks to a non-polarizing cube beam splitter. The resulting interference pattern, namely the hologram, is recorded and thus digitized by the CCD camera (square pixels with 4.4 µm lateral dimension), placed at a distance *d* from the image plane according to the holographic technique. The intensity and the phase of the complex wavefield traversing the PDMS sample are numerically calculated starting from these digitally recorded holograms. The DH reconstruction process is based on the theory of scalar diffraction, the complex wavefield in the image plane being obtained by means of the Fresnel transformation method[36]. It is a very flexible technique since it allows to reconstruct wavefields in different image planes without changing the set-up, i.e. without moving the sample or eventual lens elements.

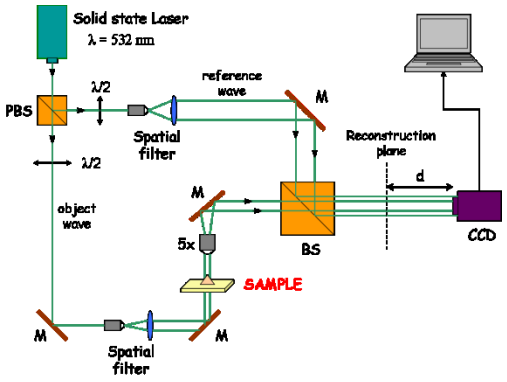


**Figure 3.7**: Experimental set-up used for the optical characterization of the PDMS microaxicon.

One of the main advantages of a Bessel beam with respect to a Gaussian one is its great depth of focus. This feature has been widely used for applications in optical trapping of small objects, exploiting the core (or even the nearest rings) of the Bessel beam as optical tweezers. In the case described in this section we have fabricated axicons that produce a Bessel beam with a core of a few μm and a depth of focus of about 240 μm for sample about 2.9 mm: the corresponding Gaussian beams, with waists of 0.6 μm, would have a Rayleigh length of 2.4 μm, that is 100 times shorter than the depth of focus of polymer sample. This is a clear advantage of optical trapping by axicons in respect for instance to the use of a 100× microscope objective. Moreover, the small dimensions of the axicons (hundreds or tens of microns) could make these elements suitable for 'on chip' applications, obviously unrealizable with large microscope objectives. In the experiment described the microaxicons was used in order to trap and move micrometric objects. An argon ion laser provides sufficient power (about 1 W @ 514 nm at the exit) to the beam that impinges on the axicon. The light focused by the axicon represents the optical trap; it can be moved inside the sample and has a 'useful distance of application' of about 240 $\mu$m along the $z$ axis (that is the depth of focus of the Bessel beam).

The beam is then imaged by a 10× microscope objective. A white lamp is used to illuminate the sample and a CCD camera (1600 × 1200 pixels) records the images. The object mainly consists of latex microspheres of diameter 10 μm dispersed in water, contained in a cell. A drawing of the trapping system[18] is displayed in **Figure 3.8 (*a*)**.

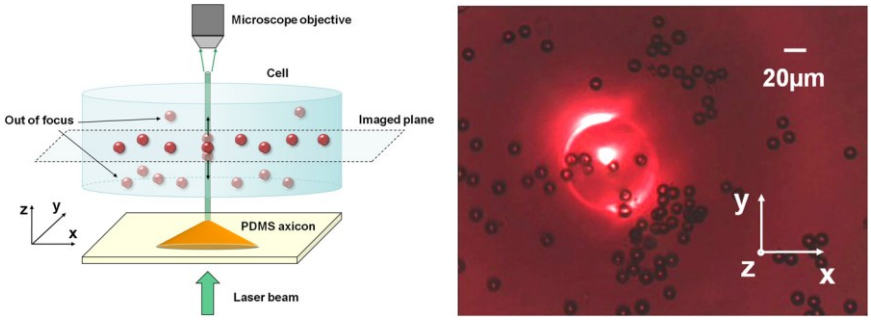


**Figure 3.8**: (*a*) Drawing of the trapping system. (*b*) First frame of the experiment showing the trapped particle confined in the *x*–*y* plane by the axicon, but free to move along the axicon's line of focus (i.e. for more than 200 µm along the *z* direction). The red circle represents the axicon's base, and is due to the white bulb illuminating the system.

The Bessel beam generated by the axicon passes through the cell. Both the axicon and the cell can be moved independently. Exploiting the large depth of focus of the beam, the particle was moved along the *z* direction. When the particle changes plane it goes out of focus; this can be recovered by adjusting the imaging microscope objective (and consequently the plane imaged by the CCD). Thanks to the great depth of focus of the axicon, the sphere which moved in different *z*-positions is still trapped in the cone of light produced by the axicon and can be dragged in the *x*–*y* plane by shifting the axicon (i.e. the glass substrate). This possibility is very amazing because the cone of light can form a sort of 'light guide' for the trapped object. **Figure 3.8 (*b*)** represents a moment of this experiment; the particle, trapped in the imaged plane, is guided along *z*, going out of focus, and moved along *x* and *y* axes, being still trapped by the beam.

In summary in this section, for one axicon producing a Bessel beam with depth of focus of 240$\mu$m, the real path of the beam exiting from the axicon up to 1 mm away has been reconstructed, starting from a single acquired image and varying the reconstruction distance in the numerical algorithm. The result shows how is possible to use the depth of focus of the Bessel beam generated through a polymer microaxicon for trapping application as optical tweezers. In particular, a 10 µm sized latex particle is trapped and moved first along the *x*–*y* plane, then also along the *z* axis, remaining confined inside the line of focus of the beam. This application could be very interesting in biology, where the (simultaneous) manipulation of biological samples in different planes could be of great importance.

### 3.5.2 Whispering Gallery Mode (WGM) Microresonators

Microspheres may be used as resonators where the resonance modes, known as WGMs, arise from the confinement of light by total internal reflection. Refractive index changes can induce a resonance shift that is used for label-free detection of a single molecule or virus[37,38]. Recently, structures with local light sources have been proposed as microresonators remotely excitable, i.e., as active microstructures, by dye[39] or quantum dots (QDs) [40,41], thus avoiding intimate contact between the resonator and the evanescent wave source for coupling light. The BOAS described in the previous chapter may be used for sensing applications[42] and, as depicted in the outlook in **Figure 3.9**, either as passive or active resonators, because PDMS has demonstrated quality factors of 106[43]. Such microresonators do not require complex fabrication processes and the smooth surfaces are spontaneously given by the surface tension. As active elements, we successfully embedded CdSe/Zns core/ shell QDs.

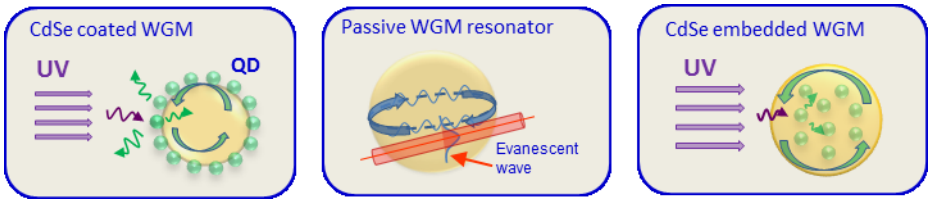


**Figure 3.9**: Outlook of the various potential micro-resonator applications: classical evanescent field coupling ; WGMs from QD-infused structures; WGMs from QD-embedded structures.

Samples of degassed PDMS with CdSe QD nanocrystals were prepared by mixing 3 mL of PDMS with 300 µL of Lumidots CdSe 590 nm (5 mg⁄mL concentration in toluene, fluorescence emission maxima spanning the visible spectrum, Sigma-Aldrich). The mixtures were obtained by vacuum-stirring in order to vaporize the solvent (toluene), making easier the curing process. A mixture droplet was placed on a glass slide and the auxiliary LN plate was mounted on independent vertical translation stages (separate configuration) to control the distance D while PDMS wire-structures were in progress. The curing process was obtained by a lamp. The fabricated 3D arranged beads can be remotely excitable without requiring distributed Bragg reflectors, as in case of the recent QD-embedded hemispherical structures in ref. 42. **Figure 3.10 (a-c)** shows the top and the side view, respectively, of the typical fluorescence effect induced into a QD-embedded frozen PDMS bridge, excited by a continuous-wave laser emitting at 325 nm. Bright rings along the rim of the bridge correspond to the formation of a preferential WGM due to the axial symmetry of the structure[42]. The QD-embedded microsphere in **Figure 3.10** exhibits homogeneous photoluminescence.

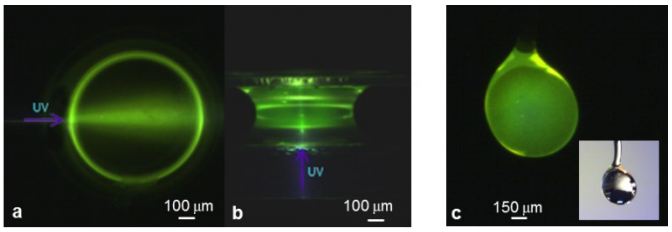


**Figure 3.10**: Top and side views of the fluorescence image generated by a QD-embedded PDMS bridge. The arrows indicate the direction of the UV signal (c) Fluorescence image of a PDMS microsphere and the corresponding white light picture (Inset). The nearly homogeneous green emission is due to the isotropic signal of the dispersed QDs combined with the spherical symmetry of the structure.

The brighter regions in the periphery are attributed to resonant modes corresponding to different wavelength emissions. Moreover, the well-known softness of PDMS would provide additional tuning functionality. In fact, as already demonstrated the cured microstructures can be mechanically stretched thus causing a change of the spherical shape. This is an important feature when WGM optical microresonators are applied for sensing purposes.

The fabrication process is easier to accomplish than other methods, where QDs are embedded into the periphery of polymer microspheres through complicated chemical procedures[40], enabling the inclusion of the QDs into deeper regions of the structures.

The ability to fabricate fibers with BOAS and diameter on the micrometer scale could give the opportunity to engineer optically actvie scaffolds at microscale. Once the scaffold is created, using the rapid-curing process reported here, its surface could be useful for tissue engineering or drug delivery by functionalizing it[44], thus avoiding problems related to the high temperature required for during the fabrication process.

### 3.5.3 TeraHz tuning of whispering gallery modes in a PDMS microsphere

Tuning the whispering gallery modes (WGMs) of an optical microcavity is a key requirement for many applications, for example, biological sensing[45], chemical sensing[46] or quantum optics[47,48]. While tuning is a desirable feature of optical microcavities it can be difficult to implement in a compact and integrated way. Different tuning techniques exist but each of these has its own advantages and disadvantages, moreover the implementation of any particular method will depend on the size, material and geometry of the microcavity under investigation. Stress/strain tuning is usually realized by applying a mechanical force (compressive or stretching) to the microcavity. The applied force deforms the cavity shape and changes the refractive index by the elasto-optic effect[47,49,50]. The resonance wavelengths

of the WGMs in polymeric microspheres, for example, are shown to have high sensitivity to mechanical forces[49].

In this section is reported a method on tuning WGMs over 15 nm (1.9 THz) in a stand-alone, stretchable, polymeric, spherical microresonator fabricated through the pyro-EHD effect **Figure 3.11**. The microsphere is directly shaped during the fabrication process, with double stems on opposite sides that can be used as tie-rods. Such tie-rods facilitate easy stretching of the microsphere without the need for any interaction or contact of mechanical tools with the resonator, hence the term "stand-alone". For this experiment the process was performed between two glass capillaries so the sphere can be easily handled. The shape of PDMS material, which has a low Young's modulus compared to glass and silica, can be changed by means of an applied force[49-51]. A 37 μm diameter PDMS microsphere is used to study the WGM shift due to stretching.

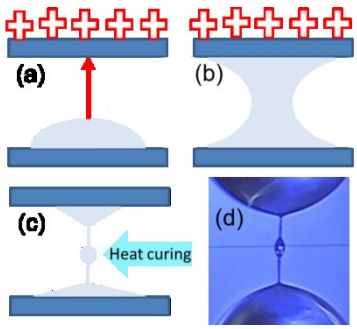


**Figure 3.11**: (a-c) Schematic of microsphere formation by pyro-EHD effect and heat curing. (d) Image of a 37 μm solid oblate PDMS sphere on a string of length, L ~ 237 μm, the stem radii are ~ 6 μm. The coupling tapered optical fiber is also visible.

The microsphere was directly fabricated onto a mechanical fiberglass frame composed of two arms to permit stretching. One arm of the frame was held in a fixed position while the other arm was free to pivot around a fixed point, see **Figure 3.12**. The free end of the movable arm was pushed or pulled by a stepper motor driven translation stage (step size 2 μm). This gives an angular displacement to the associated capillary and, hence, a continuous stretching of the PDMS microsphere was possible. For submicron stretching a piezo stack with a 4 μm range was included between the frame and the stepper motor arm. Light was coupled into the microsphere via a tapered optical fiber with a diameter ~ 1 μm. The tapered fiber was in contact with the sphere throughout the experiment and some slack was allowed in the fiber. To determine the tuning range, a typical WGM was selected. The observed Q factor of the sphere was ~$10^4$. The tension of the sphere was more or less arbitrary, though it was slightly pretensioned. When the sphere was stretched the WGM was blue-shifted and this was observed as a change in the position of the WGM on a 30 GHz laser scan window on the oscilloscope. The laser wavelength was adjusted to bring the WGM back to its initial position

in the scan window, and the wavelength shift was noted using an optical spectrum analyzer (OSA).

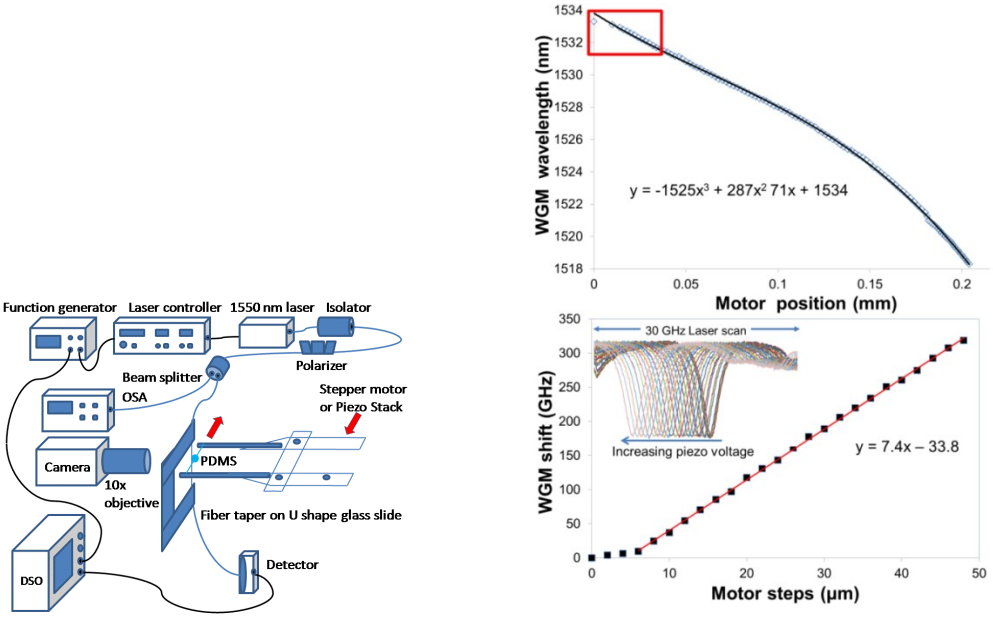


(a) (b)

**Figure 3.12**: (a) The transmitted WGM spectra are detected by a photodiode and recorded on a digital storage oscilloscope (DSO). A stepper-motor-driven translation stage, with a 1 μm resolution, is used to push the mount and stretch the PDMS sphere. The arrows indicate the direction of the motion during stretching. (b) WGM shift for increased stretching. Top: WGM wavelength shift versus motor position. The total shift is over 1 FSR (~15 nm). The solid line is a third order polynomial fit. The region highlighted by the box is shown in the lower plot. Bottom: The WGM frequency shift versus motor position. The inset shows the fine tuning of the WGM using the piezo actuator. The piezo is rated for 4.0 ± 1.5 μm displacement for 150 V.

It was possible to follow a single WGM in this way while tuning over a large blue shift (~10 nm), although sometimes the coupling of the mode became too weak and another mode had to be selected. Care was taken to ensure modes with similar shift rates were used. The summation of these mode shifts is plotted in **Figure 3.12 (b-top)** for a 200 μm movement of the motorized translation stage. The actual elongation, $\Delta L$, of the PDMS string was approximately 106 μm, determined from images taken with the CCD camera. The total recorded blue shift was larger than 15 nm. Between 10 μm and 130 μm the shift rate is linear at 0.059 nm (7.5 GHz)/μm, after 130 μm the shift rate increases nonlinearly to 0.14 nm (18 GHz)/μm. The area in the box in the top plot in **Figure 3.12 (b)** is shown again in the bottom plot of Fig. 3. In this region the shift rate is quite low due to the low tension on the sphere. Thereafter the tension reaches a threshold and the shifting rate increases sharply to a slope of 7.5 GHz/μm. The inset in **Figure 3.12 (b-bottom)** is an image of the WGM shift achieved using the the piezo to stretch the sphere.

In summary, a large WGM tuning range in a stand-alone PDMS sphere on a string was measured and a nonlinear threshold was observed. Although some drift of the WGMs was seen under high tension, the WGM shift sensitivity was quite high in the linear region. The study of the WGMs could be used to infer mechanical properties of the PDMS. Moreover potential applications exist in chemical and biological sensing if the microspheres are appropriately functionalized. Previous work in this area focused on the pressure applied to the spheres via flat surfaces or by uniform aerostatic pressure. Since the force distribution, and the resulting change in the sphere's diameter in the structure reported on here are different, changing under high strain, further study on these relationships is warranted.

**References**


[1] Hyde, S. *et al. The Language of Shape* (Elsevier, 1996).

[2] Fredrickson, G. H. & Bates, F. S. *Annu. Rev. Mater. Sci.* 26, 501–550 (1996).

[3] Kresge, C. T., Leonowicz, M. E., Roth, W. J., Vartuli, J. C. & Beck, J. S. *Nature* 359, 710–712 (1992).

[4] Cheng, J. Y., Mayes, A. M. & Ross, C. A. *Nature Mater.* 3, 823–828 (2004).

[5] Park, S. *et al. Science* 323, 1030–1033 (2009).

[6] Lin, Y. *et al. Nature* 434, 55–59 (2005).

[7] Bowden N, Brittain S, Evans AG, Hutchinson JW, Whitesides GM, *Nature* 393:146–149 (1998).

[8] Thangawng AL, Swartz MA, Glucksberg MR, Ruoff RS. *Small* 3:132–138 (2007).

[9] Stellacci F. *Adv Funct Mater* 16:15–16 (2006).

[10] Xia Y, Whitesides G.M. *Annu Rev Mater Sci* 28:153–184 (1998).

[11] Bruinink CM, et al. *Adv Funct Mater* 16:1555–1565 (2006).

[12] Park S, Huh YS, Craighead HG, Erickson D. *Proc Natl Acad Soc* USA 106:15549–15554 (2009).

[13] Scaffer E, Thurn-Albrecht T, Russel TP, Steiner U. *Nature* 403:874–877 (2000).

[14] Verma R, Ashutosh Sharma A, Kargupta K, Bhaumik J. *Langmuir* 21:3710–3721 (2005).

[15] Bhat P, et al. *Nat Phys* 6:625–631 (2010).

[16] Oliveira MSN, McKinley GH. *Phys Fluids* 17:071704 (2005).

[17] S. Grilli, S. Coppola, V. Vespini, F. Merola, A. Finizio and P. Ferraro *PNAS* 37, 15106-15111 (2011).

[18] Merola F., Coppola S., Vespini V., Grilli S., Ferraro P. *Meas. Sci. Technol.* **23** 065204 (2012).

[19] Madugani R., Yang Y., Ward JM., Riordan JD., Coppola S., Vespini V., Grilli S., Finizio A., Ferraro P., Chormaic SN. *Opt. Lett. 37, 22, 4762-4764* (2012).

[20] Park JU, et al. *Nat Mater* 6:782–789 (2007).

[21] Collins RT, Jones JJ, Harris MT, Basaran OA. *Nat Phys* 4:149–154 (2008).

[22] Yu JH, Fridrikh SV, Rutledge GC. *Polymer* 47:4789–4797 (2006).

[23] Dickey MD, et al. *Langmuir* 22:4315–4318 (2006).

[24] Maeda, N., Israelachvili, J. N. & Kohonen, M. M. *Proc. Natl Acad. Sci.* USA **100**, 803–808 (2003).

[25] Ferraro, P., Coppola, S., Grilli, S., Paturzo, M. and Vespini, V. *Nature nanotechnology* **5**, 429-435 (2010).

[26] Voicu, N.E. *Pattern Morphologies in Thin Liquid Films* Ch. 4 (2009).

[27] Zheng, Y., et al. *Nature* **463**, 640-643 (2010).

[28] Ting, T.H. et al. *App. Phys. Lett*. **89**, 234101 (2006).

[29] Mugele F. & Baret, J-C *J. Phys: Condens Matter* **17,** R705–R774 (2005).

[30] Arimoto, R., Saloma, C., Takuo Tanaka, T.& Kawata, S. *Applied Optics* **31**, (1992).

[31] Arlt, J., Chavez, V.G., Sibbett, W. & Dholakia, K. *Opt. Comm.* **197**, 239 (2001).

[32] Cheong, W.C. et al. *Appl. Phys. Lett*. **87**, 024104 (2005).

[33] Lei, M. & Yao, B. *Opt. Comm*. **239**, 367–372 (2004).

[34] Milne, G., Jeffries, G.D.M. & Chiu, D.T. *Appl. Phys. Lett.* **92**, 261101 (2008).

[35] P. Ferraro, S. De Nicola, and G. Coppola, "Digital holography: recent advancements and prospective improvements for applications in microscopy" Optical Imaging Sensors and Systems for Homeland Security Applications, vol. 2 of Advanced Sciences and Technologies for Security Applications series B. Javidi ed., (Springer, 2005), pp. 47-84.

[36] S. Grilli, P. Ferraro, S. De Nicola, A. Finizio, G. Pierattini and R. Meucci, *Opt. Express* **9**, 294 (2001).

[37] Armani AM, et al. *Science* 317:783–787 (2007).

[38] Vollmer F, Arnold S, Keng D. *Proc Natl Acad Sci* USA 105:20701–20704 (2008).

[39] Francois A, Himmelhaus M. *Appl Phys Lett* 94:031101 (2009).

[40] Beier HT, Cotè GL, Meissner KE. *Ann Biomed Eng* 37:1974–1983 (2009).

[41] Haase J, et al. *Appl Phys Lett* 97:211101 (2010).

[42] Dong CH, et al. *Appl Phys Lett* 94:231119 (2009).

[43] Ioppolo T, Ayaz U, ÖtügenMW. *Opt Express* 17:16465–16479 (2009).

[44] Sill TJ, von Recum HA. *Biomaterials* 29:1989–2006 (2008).

[45] Frank Vollmer & Stephen Arnold, *Nature Methods* 5, No. 7 Page 591-596 (2008).

[46] Andrea M. Armani, Rajan P. Kulkarni, Scott E. Fraser, Richard C. Flagan, Kerry J. Vahala, Label-Free, *Science* 317, Page 783-787 (2007).

[47] Wolf von Klitzing, Romain Long, Vladimir S Ilchenko, Jean Hare and Valérie Lefèvre-Seguin, *New Journal of Physics* 3, Page 14.1-14.14 (2001).

[48] Y. Louyer, D. Meschede, and A. Rauschenbeutel, *Physical Review. A* 72, Page 031801 (2005).

[49] T. Ioppolo, U. K. Ayaz, and M. V. Ötügen, *Journal of Applied Physics* 105, Page 013535 (2009).

[50] Rico Henze, Tom Seifert, Jonathan Ward, and Oliver Benson, *Optics Letters* 36, No. 23, Page 4536-4538 (2011).
[51] Khodadad N. Dinyari, Russell J. Barbour, D. Andrew Golter, and Hailin Wang, *Optics Express* 19, No. 19, Page 17966-17972 (2011).

# Chapter 4

## 4.1 Introduction to the high precision patterning of biomaterials

In this chapter a new method is described for processing biomaterials in order to fabricate scaffold for tissue engineering application using the properties of the pyro-electric platform. Starting from the studies developed about the manipulation of polymer for the fabrication of three-dimensional structures, such as microlenses, microresonators and microaxicon, in the following sections a new approach is described in case of polymer biocompatible and biodegradable. In fact, the design and fabrication of micro and nanostructures is of crucia[1] importance in different areas of tissue engineering1. In this specific field, the use of biopolymers is very useful because of their inherent biodegradability, biocompatibility and biofunctionality. These materials are generally electro-spun in the form of fibers. This peculiar material assembly provides the surface with special advantages and properties in terms of cytocompatibilty, cell adhesion and proliferation[2-4]. Through the years, a substantial exploitation of the conventional electrospinning (ES) within the biomedical sector has led to the production of scaffolds for tissue engineering applications, including blood vessels[5], bone regeneration[6], muscles[7], skin[8] and neuronal tissues[9]. Nevertheless, to the organization of polymeric biomaterials fibers into precise and ordered scaffolds that mimic the anisotropy of the hierarchical structure of the extracellular matrix, might improve the scaffold bioactivity in terms of cell attachment, spreading and polarization. Complex patterns of biomaterials could support or inhibit cell adhesion and growth[10], instructing cells through micro-engineered of ordered fibers[11]. Moreover, morphological and topographical features often affect cell differentiation and migration, therefore, biophysical cues might be utilized to manipulate and control cell fate[12-13]. Well-defined arrays or highly ordered 3D structures are desirable as potent tools for device fabrication with various functionalities and applications in photonics and electronics[14-17]. Patterning active organics with high spatial control by soft printing methods, without using high-energy beams or heating procedures causing irreversible degradation of active molecules, allows a wide range of functional, lightweight and low-cost components and arrays to be realized[18,20], including electro-optic devices, flexible transistors and polymeric miniaturized waveguides[20-22]. Furthermore, oriented polymer microfibers are also suitable as sub-micron scale light-sources for lab-on-chip devices[14] and find relevant applications in bio-nanophotonics and nanoscale sensing elements[15]. All these systems can be ultimately integrated in the human body for generating or transporting optical or electronic signals from and to cells, and for constituting integrated arrays of sensors[23-25]. So far is of

great interest the possibility of spinning fibers directly in well-ordered patterns both for engineering cell-scaffolds or even for realizing novel optoelectronic microstructures[26]. However, as reported in literature the full-control in the fabrication of ordered fiber patterns by ES is very hard to achieve. In fact, typically, the ES-based fibers are deposited onto the collector as nonwoven mats according to the bending instabilities associated with the spinning jet[27]. The main efforts performed for arranging fibers into ordered geometries make use of different means such as rotating collectors[28,29], patterned electrodes[30], magnetic fields[31,32], thus leading to severe limitations to the types of usable substrates, patterned areas and achievable topographies. Additional electrodes have been also used with the aim at controlling the orientation of fibers during spinning[33]. However, the presence of conductive patterns on the final device is not always desirable. Piezo-inkjet techniques have been proposed for overcoming the electrode-dependent limitations, but with poor results in terms of spatial resolution (hundreds of microns)[34], and with additional drawbacks related to nozzle clogging in case of highly viscous fluids. Also the melt-ES process has been demonstrated reliable for fabricating nanofibers mats with high geometric fidelity[35], but this technique is limited in the microscale resolution and the heating involved in the process might cause irreversible degradation of active molecules. Recently, near-field ES (NFES) was proposed for depositing isolated nanofibers on micropillars or complex microstructures, but without full-control of the single fiber that is affected clearly by bending instabilities[36,37]. An additional cylindrical side-wall electrode was adopted by Lee et al.38 in order to focus the ES jet toward a sharp-pin electrode, but again at cost of a more complex set-up.

In this chapter an unconventional but very simple approach based on the pyro-electric effect for fiber spinning is explained and experiments regarding the direct fabrication of 2D full-ordered patterns are described. The pyroelectric effect is used here for defining a stable working condition able to print well-ordered polymer fibers, avoiding the typical spiraling effect of conventional ES. Moreover, an additional applications of the proposed technology for controlling cell adhesion and contact guidance is investigated.

## 4.2 Experimental set-up and pyro-electric spinning characterization

The set-up used in conventional ES is usually quite complicated and requires at least four major components: a biased spinneret, a syringe pump, an external power supply and a collector surface. Conversely the system proposed in this work, for accomplishing high precision printing is electrode-free, as illustrated in **Figure 4.1**. The drop reservoir is placed directly onto a plane substrate (base) while an electric field, induced by the pyroelectric effect

activated onto a Lithium Niobate (LN) crystal[38], exerts an attractive force on the polymer drop deforming it into a Taylor's cone and therefore generating liquid jet emission. The fibers are printed directly onto the target substrate (collector) facing the base at a distance d, that is mounted onto a computer-controlled x,y axes translation stage, with translation speed of 0.7 mm/s.

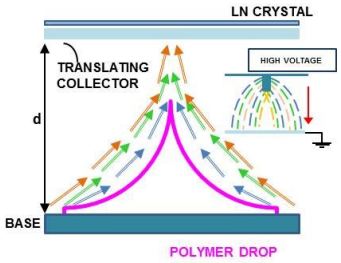


**Figure 4.1**: Set-up and schematic of sharp-cone electric field lines (colored arrows) compared with conventional ES field (inset) deforming the polymer drop into a Taylor cone.

Controlling the distance d, the elongated tip of the Taylors' cone is put in direct contact with the collector, **Figure 4.2**. This contact has two effects. First, the adhesion allows to fix the fiber emerging from the Taylor's cone on the collector substrate, thus avoiding the onset of bending instabilities and tethering continuous liquid flow (Q) to the collector. If the collector is displaced, the fiber is forced to follow it and in this way the fiber flowing out from the elongated Taylor's cone could be deposited directly on it. The above forces act as a tether thus achieving the full-control of the spinning process switching between a random-coated fiber deposition to a linear and ordered path. In fact, in the case of the pyro-electric condition of spinning the emission of the polymer jet is finely controlled in space thus defining a stable condition for patterning the polymer and suppressing the bending instabilities occurring during the ES process[39-42].

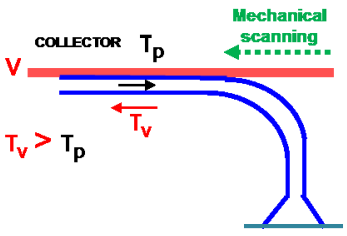


**Figure 4.2**: Stretching and straightening the polymer fiber.

The pyro-electrodynamic system assures a stable process reducing the non-axisymmetric instabilities due to the charge distribution, the aerodynamic interaction, and the bending

torque produced from jet dipole charge interaction with the external electric field and the repulsion of surface charges. In fact, this procedures operates in the regime of NFES (d< 1cm) but allows an improvement of the spatial resolution and a full-control of the spinning process. It is important to note that the pyro-electric field generated, in the range 2.7× 107 V m-1 < Epyro < 5.5× 107 V m-1 , has intrinsically, when compared to conventional ES, an optimum arrangement of the electric field lines[38]. In fact, the sharp-cone distribution of the electric field lines provides (color lines in Figure 4.1) a suitable electric field 3D distribution with higher selectivity for the attraction force on a single fiber thus improving the stability and resolution in the deposition process, that has never observed before. Tethering the spun fiber allows to stop the chaotic intrinsic nature of the ES jet and consequently the spiraling effect frequently appearing in the near field ES patterns is completely eliminated. The use of the pyro-ES leads to work at the boundary condition between the Ohmic and the conductive flow. Tethering the jet to the collector leads to choose an Ohmic working condition for a steady cone jet. In particular, referring to a relatively conductive liquid we can work moving around the neighborhood of point W (EM, QM) of plot[43] in **Figure 4.3**.

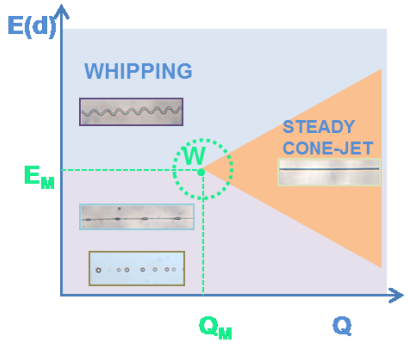


**Figure 4.3**: Plot of the working point W as function of the electric field E and the polymer flow Q.

In fact, once the optimal operational condition of flow (QM) has been determined, a stable cone jet can be produced for Q>QM only in a limited range of electric field around EM. Experimentally we can change the working-point W by changing the distance d because the electric field depends on the distance[39]. Specifically, at high field strength and flow rate we observe the origin of whipping instabilities (case 1) with smaller jet diameter due to the acceleration and stretching of the polymer prior the solidification or the impact on the collector. Conversely, for E~EM a stable cone jet for printing continuous polymer lines can be formed (case 2). In case of E≤EM, a pulsating cone jet opens the way to an instability complex regime (case 3) while at least if E<<EM a dripping condition takes place, analogously to hydrodynamic dripping (case 4) [44]. The versatility of the pyro-ES process

gives the possibility of switching from the condition of patterning ordered fibers to that of printing separate dots. Using the intrinsic viscoelasticity of the polymer we can perform the printing of regular but long wave forms of instability, such as whipping instabilities or printing of beads-on-a-string. Moreover, the fluid mechanics of the polymer affects the geometry of the jet[45] Figure 4.2. Tethering the jet to the collector introduces a tangential shear stress. The shear stress $\tau_v$ induced by the constrain in movement with a velocity of $v_v$ balances the component of velocity along the x-y axes and overcomes the tangential stress $\tau_p$ of the polymer putting straight the fiber deformed by the tangential electric stress. The fiber is tethered and stopped on the substrate by the external force $F_v$ induced by the constrain balancing the force responsible of the fiber motion in the Lagrange equation[46]:

$$m_i \frac{d^2 r_i}{dt^2} = F_{exi} + F_{ini} + F_{bi} + F_v$$

Fexi external forces on the i-elementary volume (gravity, aerodynamic, electric), Fini internal force (viscoelastic or Coulomb's force), $F_{bi}$ bending restoring force (to restore the rectilinear shape of the bending part of the jet), **Figure 4.4**.

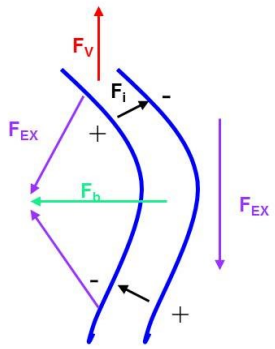


**Figure 4.4**: Schematic of the forces acting on the polymer jet in air before tethering the fiber to the substrate.

Once the polymer jet is tethered to the substrate of interest, it could be used to realize well-ordered patterns thus completely avoiding the whipping perturbations driven by the lateral electric force and the aerodynamic interactions. Moreover, the patterns realized by pyro-ES present a good spatial resolution reducing the deflection of the jet caused by the transiently charged nanofibers that, conversely, are deposited randomly in case of conventional ES. In fact, working under the aforementioned conditions permits to fabricate highly ordered and precise patterned structures using tethered fibers thus surpassing the bending force produced from dipole charge distribution within the jet and that interacts with the external electric field as well as bending caused by repulsion of surface charges[41,43].

### 4.3 Fabrication of well-ordered biocompatible and biodegradable patterns

The experiments performed here show the direct writing of the poly-co-glycolic acid (PLGA) ink overpassing the viscosity border of 10 cps of conventional inkjet systems. The PLGA 50:50 (PLGA RESOMER RG 504H), 3800-5400 Dalton, was obtained by Boeringer Ingelheim and the Dimethyl Carbonate (DMC) was used as solvent of the PLGA. High voltage is achieved by a very simple, electrodless, nozzless and cost-effective system. The substrate is conveniently chosen for various applications and no special requirements are needed as in case of conventional ES. Because of the intrinsic stability of the system it is possible to produce fiber patterns with uniform diameter and regular geometry, as shown in **Figures 4.5**.

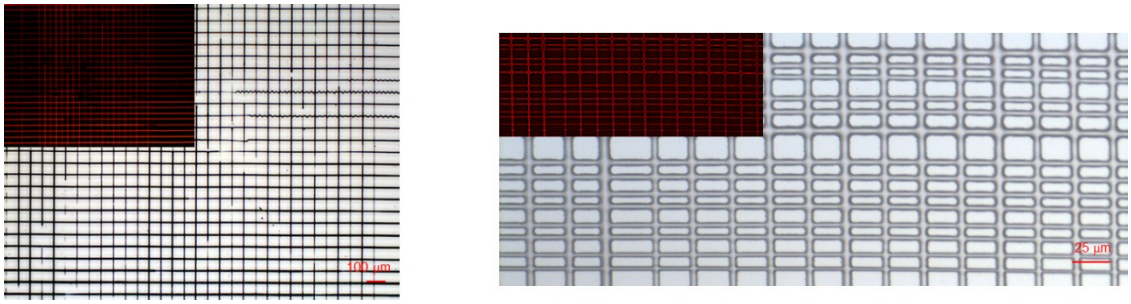


**Figure 4.5**: 2D full ordered polymer micro patterns: (a) Ordered square grid with period of 55 µm. (b) Ordered rectangular grid with period of 25µm.

Adjusting some experimental parameters such as the electric field, the concentration of the polymer ink and the flow rate we are able to reduce the jet diameter increasing the charge density on the surface but with a lower bound48. Controlling the bending instabilities we are able to define a stable condition for fabricating patterns of well-arranged and uniform lines at the nanoscale. As shown in Figure 4.6, PLGA patterns have lines with diameters ranging from 0.5 to 35 µm.

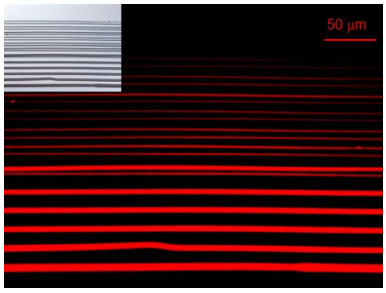


**Figure 4.6**: Uniform lines with diameters ranging from 1 to 10 µm.

It is important to note that starting from a drop reservoir of 500 µl it is possible to print a continuous fibre of about 200 µm length without interrupting the process and working in a stable condition printing also sharp angles with high resolution (**Figure 4.7**).

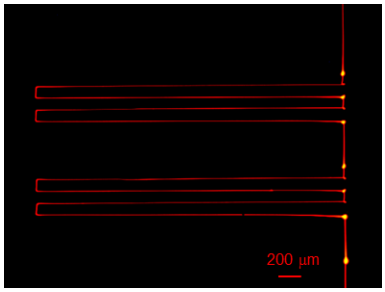


**Figure 4.7**: Sharp 90 degrees corners

Further experiments were conducted aimed at obtaining more intriguing patterns. Controlling the fluid relaxation and the elongation viscosity of the polymer (case 3) it is possible to print the capillary polymer break-up leading to the formation of knotted fibers. This kind of fibers could be useful for the incorporation of nanometer sized objects (drugs, dyes, enzymes) to produce functional fibers[49]. In others experiments, in order to fabricate more complex patterns the buckling phenomenon was induced on the tip of the liquid fibre in contact with the substrate by a slight approaching of the lower substrate to the collector substrate. In this case, the polymer jet works in oscillating mode under the action of the pyroelectrodynamic field, as depicted in **Figure 4.8 (a)-(b)**. Sinusoidal coiling and overlapping script-like "e" are observed and compared with a continuous fibre. The buckled patterns obtained are due to the jet compression at impingement on the collector used as substrate and moved in the direction shown by the blue arrow in the figures. The profiles are very regular and similar to those obtained in case of ES jets[50] but the substrate is slower than those reported for conventional ES experiments (0.01 m/s), which is a significant experimental advantage.

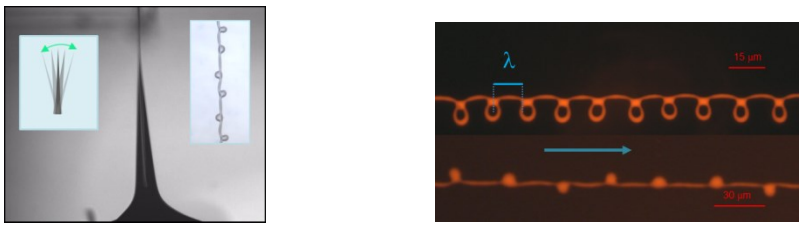


(a) (b)

**Figure 4.8**: Buckilng patterns at the microscale: (a) polymer jet works under the pyroelectric pressure. (b) Periodic (λ) buckling patterns.

Increasing the distance d the frequency decreases, while at shorter distances it becomes higher. Balancing the frequency and the velocity v we can control the type of profiles

produced. The results show that the buckling frequency and the wavelength varies as a function of experimental and rheological parameters. In particular different patterns with different wavelengths λ, ranging from 15 to 50 μm were realized after the impingement onto a microscope glass slide. A further experiment was performed in order to demonstrate the possibility of combining the use of the pyro-ES to design more complex geometries **Figures 4.9 (a-c)** and suspended fibers over a polymeric open channel. These results open the way to the fabrication of high-resolution three dimensional periodic microstructures with great potential.

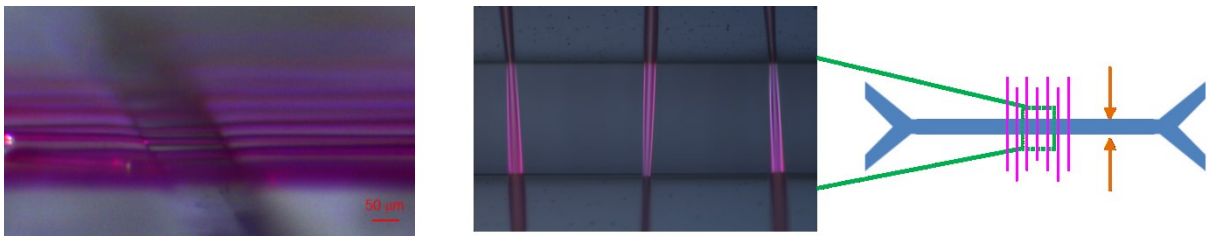


(a) (b) (c)

**Figure 4.9**: Perspective view (a) and top view (b) of suspended three dimensional fibers over a polymeric double y channel 150 μm width (c).

### 4.4 Cell contact guidance onto ordered fibers

Given the importance of the contact guidance and cell polarization in several tissue engineering and biotechnological applications, we analyzed the morphological features of human mesenchymal stem cells (hMSC) seeded on both linear and dot-like PLGA patterns. In order to limit cell adhesion only on the polymer, thus discouraging non-specific attachment on the supporting substrate, the polymer was electro-deposited on a PTFE coated glass slide. Human mesenchymal stem cells were purchased from Lonza. As specified by the company, hMSCS were harvested from normal human bone marrow. hMSCSs were cultured in αMEM (α modified Eagle's medium, Lonza) supplemented with 10% FBS (Fetal Bovine Serum), 1% L-glutamine and 1% penicillin and 1% streptomicyn. Cells were kept in the incubator at 37°C, 5% CO2, cells propagation was limited to passage 5. Cells were seeded onto the materials at 1x103 cell/cm2 and the medium was replaced every 3 days. To characterize cell-material interaction in terms of cell and nuclear morphology, cells were stained with TRITC-conjugated Phalloidin and 4',6-diamidino-2-phenylindole (DAPI). Briefly, the samples, fixed in PF 4% for 20 minutes, were washed with PBS and incubated with PBS-Tryton solution 0,1% for 10 minutes at RT. The samples were then rinsed twice with PBS and aspecific antigenic sites were saturated with PBS-BSA 0,5% for 10 minutes. Phalloidin solution was added (1:200 in PBS-BSA 0,5%) and after 30 min of incubation at RT, the samples were

rinsed with PBS. Subsequently, DAPI solution (1:1000) was added and the samples were incubated for 15 minutes at 37°C. Finally samples were washed in PBS and stored in PBS at 4°C. For the experiment of contact guidance over the ordered fibers hMSC were cultivated for 24 h and then fixed and stained for the visualization of cytoskeletal stress fibers and nuclei. Cell bodies were predominantly located within the inter-fibre gap and actin stress fibers were strongly coaligned with the pattern direction, **Figure 4.10**.

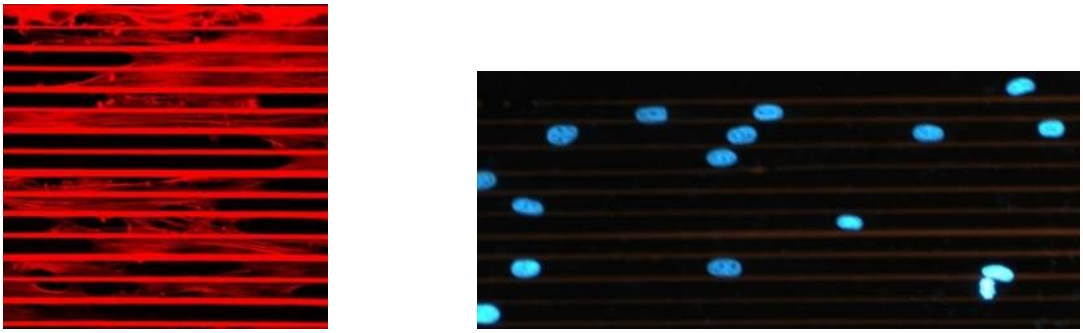

(a) (b)

**Figure 4.10**: (a) Cell body co-aligned with the pattern direction and (b) Nuclei patterning inter-fibre gap.

According to figure 4.10(b) the vast majority of nuclei were located between the fibers, displaying a prolate elliptical shape. Conversely, cells cultivated on dot-like patterns exhibited a multipolar morphology, with cell protrusions contacting the polymeric islets, **Figures 4.11 (a)-(b)**. Although a common cell orientation was not observed, hMSC acquired an elongated shape co-aligned with the direction of the polymer deposition in those zones of the substrate where the polymeric features were more closely packed. Cell nuclei displayed a more rounded shape respect to that observed on linear patterns. As expected, no direction of nuclear polarization was recorded.

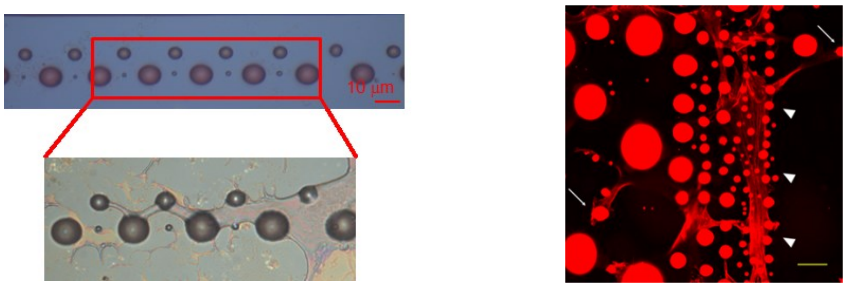


**Figure 4.11**: (a) Dots-like patterns in parallel lines and cell alignment with pattern direction. (b) Confocal micrograph of TRITC-Phalloidi stained hMSC on dot-like patterns. Cellular protrusions are mostly connected with polymeric spots (white arrows). hMSCs in contact with small, densely packed spots (white arrowheads), align with the direction of polymer deposition. Scalebar: 20 µm.

Digital holography made possible a phase-contrast imaging of the stem cells, as shown in **Figure 4.12**. The results show that the technique could open the route to a mould-free technology able to generate arbitrary and complex micro-architectures for controlling, aligning and modelling the cell distribution.

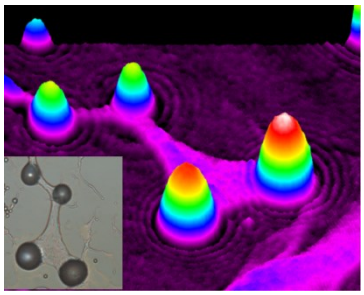

**Figure 4.12**: Triangular dots pattern (inset) and phase-contrast image obtained by digital holography.

In conclusion, the present study describes an approach that could be used to overcome the current limitations of conventional ES technique. In fact, pyro-ES allows the production of well-ordered fiber patterns with high resolution thus reaching a challenge goal that has been pursued since the development of ES. The advantages in terms of compactness, simplicity and cost of such system makes it a promising technology also for the direct printing of predefined and well-ordered structures. In particular, the results show that pyro-ES could be used for scaffolds for controlling cell adhesion and morphology. This opens new routes for arbitrary and controlled cell patterning on surfaces of synthetic materials for biomedical applications. New intriguing perspectives for patterning active organic materials for opto-genesis studies and for constituting integrated arrays of sensors in the human body can be foreseen.

**References**


[1] Badylak, S. F. & Nerem, R. M. *Proc. Nat. Acad. Sci*. 107, 3285-3286 (2010).

[2] Huang, L., Nagapudi, K., Apkarian, R. P. & Chaikof, E.L. *J Biomater Sci, Polym Ed* 12, 979–993 (2001).

[3] Kenawy E.-R. et al. *Biomaterials* 24, 907–913 (2003).

[4] Huang N. F. et al. *Nano Lett.* 6, 537–542 (2006).

[5] Xu, C. Y., Yang, F., Wang, S. & Ramakrishna, S. *J. Biomed. Mater. Res., Part A* 71, 154-161 (2004).

[6] Guarino, V., Alvarez-Perez, M., Cirillo, V. el al. *Bioact. Compat. Polym.* 26, 144-160 (2011).

[7] Chen, Z. G., Wang, P. W., Wei, B., Mo, X. M. & Cui, F. Z. *Acta Biomaterialia* 6, 372-382 (2010).

[8] Zhao, P. C., Jiang, H. L., Pan, H., Zhu, K. J. & Chen, W. *J. Biomed. Mater. Res., Part A* 83, 372-382 (2007).

[9] Yang, F., Xu, C. Y., Kotaki, M., Wang, S. & Ramakrishna, S. *J. Biomater. Sci., Polym. Ed.* 15, 1483-1497 (2004).

[10] Dvir, T., Timko, B. P., Kohane, D. S. & Langer, R. *Nat. Nanotech* 6, 13-22 (2011).

[11] Lutolf, M. P., Gilbert, P. M. & Blau, H. M. *Nature* 462, 433- 441 (2009).

[12] Hashi, C. K. et al. *Proc. Nat. Acad. Sci.* 104, 11915-11920 (2007).

[13] Schnell, E. et al. *Biomaterials* 28, 3012- 3025 (2007).

[14] Pagliara, S., Camposeo, A. Polini, A., Cingolani, R. & Pisignano D. *Lab on a Chip* 9, 2851- 2856 (2009).

[15] Camposeo, A., Persano L. & Pisignano D. *Macromol Mater. Eng*. DOI: 10.1002./mame.201200277 (2013).

[16] Favier, F., Walter, E. C., Zach, M. P., Benter, T. & Penner, R. M. *Science* 293, 2227-2231 (2001).

[17] Melosh, N. A. et al. *Science* 300, 112-115 (2003).

[18] Menard, E. et al. *Chem. Rev.* 107, 1117-1160 (2007).

[19] Carlson, A., Bowen, A. M., Huang, Y., Nuzzo R. G. & Rogers, J. A. *Adv. Mater.* 24, 5284-5318 (2012).

[20] Liu, H.Q., Edel, J. B., Bellan, L. M. & Craighead, H.G. *Small* 2, 495- 499 (2006).

[21] Meng, C. et al. *Adv. Mater*. 23, 3770 (2011).

[22] Vetsch, E. et al. *Phys. Rev. Lett.* 104, 203603 (2010).

[23] Rogers, J. A. *Nature* 468, 177-178 (2010).

[24] Kim, D.-H. et al. *Science* 333, 838-843 (2011).

[25] Kim, D.-H. et al. *Nat. Mater.* 10, 316-323 (2011).

[26] Kurpinski, K. T., Stephenson, J.T., Janairo, R. R. R., Lee, H. M. & Li, S. *Biomaterials* 31, 3536-3542 (2010).

[27] Lim, S. H. & Mao, H. Q. *Adv. Drug Deliv. Rev.* 61, 1084-1096 (2009).

[28] Boland, E. D., Wnek, G. E., Simpson, D. G., Pawlowski, K. J. & Bowlin, G. L. *Macromol Sci Part A: Pure Appl Chem* 38, 1231-1243 (2001).

[29] Katta, P., Alessandro, M., Ramsier, R. D. & Chase, G. G. *Nano Lett* 4, 2215-2218 (2004).

[30] Li, D., Ouyang, G., McCann, J.T. & Xia, Y. *Nano Lett* 5, 913-916 (2005).

[31] Li, D. & Xia, Y. *Adv Mater* 16, 1151-1170 (2004).

[32] Chang, G. Q. et al. *App. Phys. Lett.*101, 263505 (2012).

[33] Xie, J. W. et al. ACS *Nano* 4, 5027–5036 (2010).

[34] Kim, J. D., Choi, J. S., Kim, B. S., Choi, Y. C. & Cho, Y. W. *Polymer* 51, 2147-2154 (2010).

[35] Dalton, P. D., Joergensen, N.T., Groll, J. & Moller, M. *Biomed. Mater.* 3, 034109 (2008).

[36] Zheng, G. F., Li, W. W., Wang, X., Wu, D. Z., Sun, D. H.& Lin, L. W. J. *Phys. D: Appl. Phys.* 43, 415501 (2010).

[37] Sun, D. H., Chang, C., Li, S. & Lin, L. W. *Nano Lett.* 6, 839-842 (2006).

[38] Lee, J., Lee, S.Y., Jang, J., Jeong, Y.H. & Cho, D. -W. *Langmuir* 28, 7267-7275 (2012).

[39] Ferraro, P., Coppola, S., Grilli, S., Paturzo, M. & Vespini, V. *Nat. Nanotechnol*. 5, 429–435 (2010).

[40] Reneker, D.H., Yarin, A.L., Fong, H. & Koombhongse, S. *J. Appl. Phys* 87, 4531-4547 (2000).

[41] Yarin, A.L., Koombhongse, S. & Reneker, D.H. *J. Appl. Phys* 89, 3018-3026 (2001).

[42] Kiselev, P. & Rosell-Llompart, J. *J. Appl. Polym. Sci.* 125, 2433-2441 (2012).

[43] Shin, Y. M., Hohman, M. M., Brenner, M. P. & Rutledge, G. C. *Appl. Phys. Lett* 78, 1149-1151 (2001).

[44] C-H. Chen, Electrokinetics and electrohydrodynamics in microsystem, pp 177, Springer Wien New York, ed A. Ramos (2011).

[45] Bhat P. P.et al. *Nat. Phys.* 6, 625–631 (2010).

[46] Sun, Y. F., Zeng, Y. C. & Wang, X. H. *Ind. Eng. Chem. Res.* 50, 1099-1109 (2011).

[47] Grilli, S. et al. *Proc. Nat. Acad. Sci.*108, 15106 (2011).

[48] Wei, C. & Dong, J. J. *Micromech. Microeng.* 23, 025017-025026 (2013).

[49] Zhao, P. C., Jiang, H. L., Pan, H., Zhu, K. J. & Chen, W. *J. Biomed. Mater. Res., Part A* 83, 372-382 (2007).

[50] Yang, F., Xu, C. Y., Kotaki, M., Wang, S. & Ramakrishna, S. J. *Biomater. Sci., Polym. Ed.* 15, 1483-1497 (2004).

# Chapter 5

## 5.1 Biodegradable microneedles for drug delivery applications

In the final section of this thesis it is described an additional application regarding the manipulation of biomaterials by the pyro-EHD effect. In particular, the pyro-electric field is applied for the deformation of biomaterials into a conical tip that could be assimilated to the shape of a needle. The fabrication process is studied and characterized for different kind of polymers and the final 3D microstructures produced are tested for biomedical application. This structures are clearly assimilated to microneedles and the pyro-procedure used offers a lot of advantages compared to the conventional methods used. Overall, this technique works in a contact-free and mould-free method permitting the fabrication of biodegradable polymer microneedles into a ready-to-use configuration. Microneedles have attracted a lot of interest in the recent years both for researcher and industrial point of view. Microneedles are well known in the pharmaceutical field as effective and pain-free micro-scale devices employed for transdermal vaccination and drug delivery[1]. In particular, vaccine delivery via microneedles has attracted considerable attention since it elicits immune responses comparable to, or better than, traditional skin delivery via hypodermal injections[2]. In fact, drug delivery via hypodermal syringe injection is still commonplace, despite its numerous limitations and drawbacks such as pain, one-shot administration and risk of infection while microneedles could offer an appropriate alternative to this technique used all over the world. Microneedles have been studied in vitro, in animals and in humans for a variety of applications and there are also examples of clinical trials at advanced phases[3]. In addition, no significant adverse reactions to microneedles have been reported[4]. More in general, microneedles can be engineered and used for the transdermal delivery of several biomolecules, proteins, vaccines, DNA, antibodies, or genes[5-9]**.** Biologically stable microneedles with drug-coated surfaces and hollow microneedles[8-10] for drug injection were first developed and proposed as external devices to control drug administration, albeit their use was limited by the infection risks associated with the needle breakage. Dissolving or degradable microneedles were later developed to overcome this safety issue and proved able to release encapsulated pharmaceutical molecules into the skin after dermal insertion[7,11-13]. Unfortunately, the production technologies of the above delivery systems have proved quite difficult and their diffusion is therefore limited. Indeed, most dissolving microneedles are fabricated by micro-casting methods based typically on the following steps: fabrication of the master structure; fabrication of the three-dimensional (3D) mould; filling of the polymer with the drug to be

encapsulated; setting of the polymer; separation of the dissolving microneedle patch from the 3D mould[12,14-16]. Since microneedles must have appropriate mechanical properties and sufficient strength[12,17] to penetrate the skin, setting is crucial. Recently, a novel drawing lithography technique[18-20] has been proposed as a potential solution to some of the above issues. It creates 3D microstructures from two-dimensional (2D) thermosetting polymers but, even if free from replica moulding, such technique still requires the micro-fabrication of the stainless frame used for drawing the polymer. Moreover, since microneedle formation is due to the breakage of the drawn polymer, there is only little control of the final shape. Even if this technology has recently been improved[21] allowing better shape control, it still relies strongly on the dynamic interaction between frame and fluid, which leads to a poor reproducibility compared to the mould technology. In summary, all the techniques reported in literature are contact-dependent with potential cross-contamination deriving from mould cleaning and/or drug exchange and rely on pre-fabricated frames and on cumbersome multi-step processes that impair both mass production of pre-prepared patches and the possibility of a point of care approach.

In this final section it is described the non-contact and mild temperatures electro-drawing (ED) process for the direct and rapid fabrication of biodegradable microneedles by means of an electrohydrodynamic (EHD) process activated by the pyro-electric effect. The technique described consists of drawing the microneedles from a biopolymer reservoir as in the drawing lithography approach, but with the outstanding advantage of being contact-free. Moreover, the use of the EHD forces overcomes all the limitations deriving from the micro-casting and the drawing lithography approach, since no micro-moulding, no hazardous temperatures and no multi-step filling process are required. In fact, biopolymers are processed from solution at temperatures in the range of 20 ÷ 40 °C and are shaped directly into microneedles in a contact-free, single step process. The results show the possibility to form microneedles of variable shapes onto flexible polymer strips that could to be easily inserted in a cuff as a sort of disposable cartridge for transdermal drug delivery. In fact, they could be fabricated on a flexible substrate/holder by drawing them directly from drop reservoirs, at room temperature and using a controlled EHD force. The holder can be easily housed in an adjustable cuff in order to exert the correct amount of pressure to indent the skin and used for self-medicine administration. Tests of insertion are performed and discussed in order to demonstrate the capability of this method and the good geometric and mechanical properties of this microstructures and the effectiveness of the indentation process.

## 5.2 Pyro-Electric fabrication of dissolving microneedles

The set-up used for the experiment is the very similar to that used for the fabrication of the polymer microstructures of chapter 3. It is relatively easy to assemble and consists basically of a polar dielectric crystal (Lithium Tantalate - LT) facing the polymer reservoir deposited onto a PDMS strip in case of flexible arrays of microneedles, **Figure 5.1**. The deposition of multiple base drops allows the formation of microneedles under array-like configurations. The operation principle relies on the use of the pyroelectric effect generated onto the LT crystal that, consequently, operates as the driving plate (DP).[22-24]

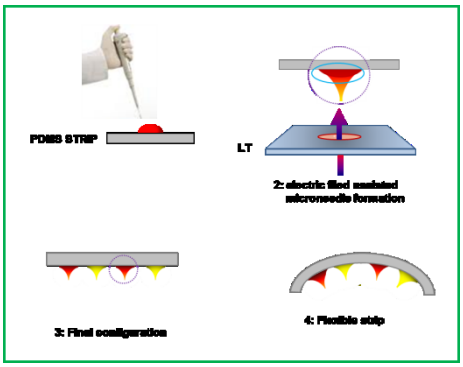


**Figure 5.1** : Schematic view of the microneedles formation procedure: starting form a reservoir polymer droplet, deposited onto a flexible PDMS strip, the pyro-EHD pressure deforms the droplet into a conical shape.

An appropriate thermal stimulus applied to the DP generates an electric field that induces an EHD force responsible for destabilizing and drawing the polymer into a microneedle shape. As a consequence of the external pyro-electric field the polymer reservoir deforms into the so-called Taylor cone[25,26] which, in this case, is assimilated to the form of a microneedle. During the drawing process, the liquid cone becomes solid due to evaporation, thus giving the desired shape to the microneedles. The geometry of the cone is governed by the ratio of the surface tension to the electrostatic attraction. The fabrication process can be controlled through the appropriate handling of the EHD process. The LT crystal was mounted onto a precision translation stage to appropriately control the distance from the drop reservoir and, consequently, the drawing force. A conventional side illumination was used to monitor the process in real time.

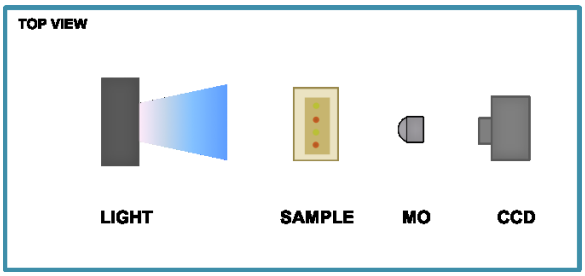


**Figure 5.2** : Top view of the imaging system, a 5x microscope objective (MO) and a digital CC camera (pixel size 12x12 $mm^2$, frame rate of 500 frames $s^{-1}$ with 1280(H) x 1024(V) spatial resolution) were used to capture side view pictures and videos during microneedle formation.

The microneedle fabrication was accomplished in three main steps, as shown in Figure 5.1: deposition of the drop reservoirs; activation of the pyro-EHD force; evaporation of the solvent. The final result is an array of microneedles formed onto a flexible strip.

The experiments were performed with different kinds of samples. The reservoir consisted basically of a biocompatible mixture of two main components: a biodegradable copolymer PLGA (poly(lactic-co-glycolic acid)), widely used for therapeutic devices and DMC (Dimethyl Carbonate). The polymer is dissolved in DMC in different mixing ratio and in order to define the better condition for the manipulation process different kinds of chromophores, as listed in Table 1, were used as "model drug" for the initial studies and characterization of the process. The polymer used for the pyro-manipulation, the PLGA 50 : 50 (PLGA RESOMER® RG 504H), 38000 - 54000 Dalton was obtained by Boeringer Ingelheim and used as received. Dimethyl Carbonate (DMC) was used as solvent of the PLGA, while the chromophores used as model drug are Nile Red, Rhodamine 6G and Fluorescein Isothiocyanate-Dextran.

| CHROMOPHORES | CONCENTRATION [mg/ml] |
|---|---|
| Rhodamine 6G | 0.25 - 0.5 – 1 |
| FITC-Dextran | 0.25 - 0.5 – 1 |
| Nile Red | 0.25 - 0.5 – 1 |

**Table 1**: List of chromophores used as typical sample drugs for microneedles fabrication.

We focused on PLGA which is widely used as a material for microneedles for its properties in terms of mechanical strength and biodegradation whose kinetics can also be tuned by embedding hydrogel microparticles[27]. A preliminary investigation was performed on the formation of single microneedles in order to characterize the main conditions that regulate the microneedle formation. Typically, the base drop was deposited onto a PDMS strip and had a volume of about 0.1 μl. The distance between the reservoir and the DP was crucial and depended on both the volume and the contact angle of the base drop. The DP was heated locally in correspondence of the base drop, while approaching the base reservoir. Since the pyro-EHD force depends on the viscosity of the fluid, the control of this parameter was crucial for the successful formation of microneedles with the necessary shape and strength to penetrate the skin. Therefore, the ED experiments were performed with PLGA samples dissolved in solvent with different mixing ratios for characterizing the drawing behaviour. A proper range of polymer concentrations was chosen, from 20 to 30 %, to guarantee suitable viscosities in the range of around 80 to 240 $mm^2/s$ (measured by using an Ubbelohde viscosimeter). Higher concentrations increase dramatically the solution viscosity, making the electric field unable to deform the drop. Conversely, at lower concentrations, the viscosity is too low and the polymer cone is not permanent. In particular, the results show that the best operation condition is defined by 25 % w/v PLGA/solvent. **Figure 5.3** shows the side view of a typical microneedle fabrication process. The PLGA reservoir appears clearly to deform into a shape consisting of a base preserving the diameter of the starting drop and of a sharp conical tip very similar to a needle.

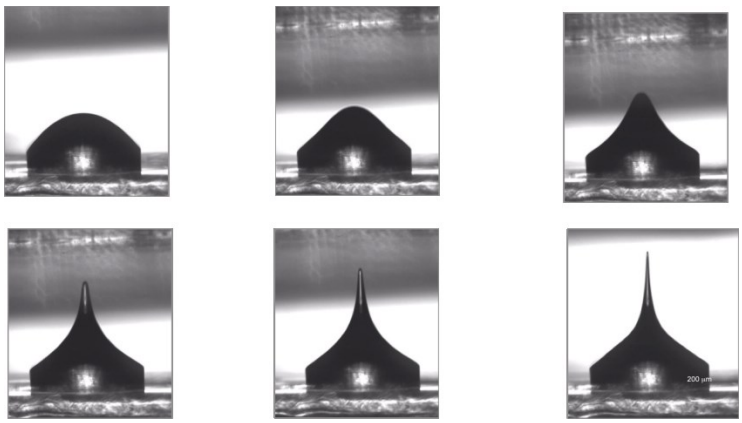

**Figure 5.3** : Side view of the evolution in time of the microneedles formation, the first frame show the starting biopolymer droplet while the following ones represent it deformation under the action of the pyro-electric field until the deformation reached in the final frame.

The reliability of these microneedles for transdermal drug delivery was investigated by using different kinds of chromophores as sample drugs (Table 1). The chromophore embedded into the dissolving structures made the visualization of the structure easier under UV illumination. **Figure 5.4** shows the side view of four different microneedles enriched with FITC-Dextran, (0.25 mg/ml; higher concentrations were not soluble), Rhodamine 6G (0.5 mg/ml; higher concentrations hindered microneedle formation), and Nile Red (0.5 mg/ml) respectively under white lamp and fluorescence illumination. The images were captured by a conventional CCD camera while illuminating each needle with an appropriate laser source. The intensity and the uniformity of the fluorescence signal appear rather poor especially in case of Dextran.

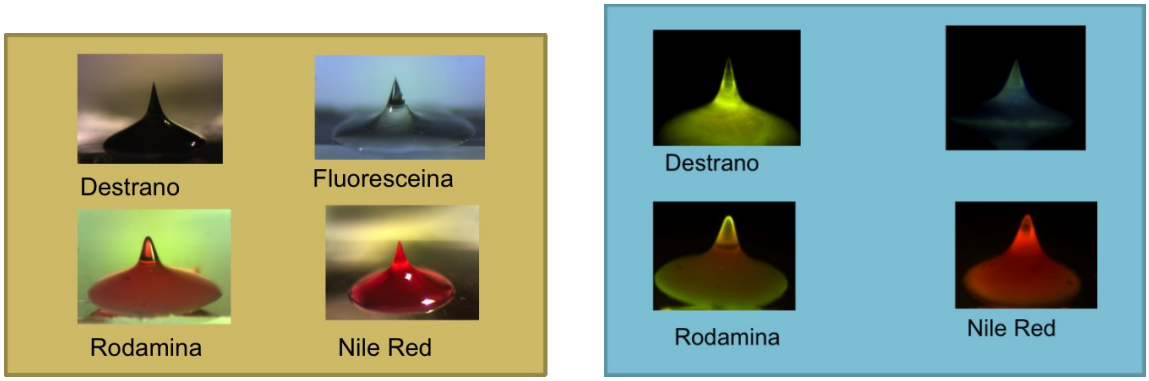


**Figure 5.4**: Side view of microneedles embedded with different kind of chromophores investigated

The distribution of the Nile Red appears notably more uniform inside the microneedles, due to its molecular polarity and therefore to its solubility in PLGA, as expected. **Figure 5.5** shows a sequence of side views of a single Nile Red microneedle acquired during the vertical scan of the needle by the beam of the laser used as illumination source.

**Figure 5.5**: Fluorescence scan of a typical microneedle along different vertical planes, the laser beam is moved from the base to the tip of the cone in order to show the photoluminescence emission of the microstructure: all this information is summarized in the last frame where a fluorescence image of the needle in total is obtained using a different angle for the incident laser beam.

These starting experimental results demonstrate the capability of the pyro process to embed some bioactive moieties into the polymer microneedle during the drawing process. The optimal working conditions in terms of manipulation, stability and geometry of the structures were obtained with the Nile Red based mixture (0.25 - 0.5 mg/ml).

It is important to note that this method provides remarkable degrees of freedom in moulding the shape of the microneedles. The polymer microneedle was formed in a single step by controlling the distance *d* between the base and the LT crystal. For base drops of 0.05 μl < V < 0.1 μl , the typical height *h* of a microneedle was 300 μm < *h* < 500 μm, which falls within the range used for indentation applications[10-13]. In **Figure 5.6** it is presented a typical side view of microneedle after formation.

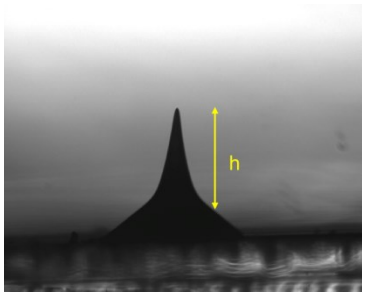


**Figure 5.6**: PLGA microneedle: side view under white lamp illumination.

We also describe how is possible to control the needle's height and the aspect ratio as a function of the droplets. In fact, the needle height increases with the volume of the drop reservoir, thus allowing some tuning the aspect ratio *h/b*, **Figure 5.7 (a)-(b)**. For instance, aspect ratios of 1.3 were obtained starting from a 0.1 μl drop reservoir. The increase of the aspect ratio with the droplet volume is most probably due to the fast consolidation of the walls with respect to the inner core that feeds the increase of the height under the persistent electric field.

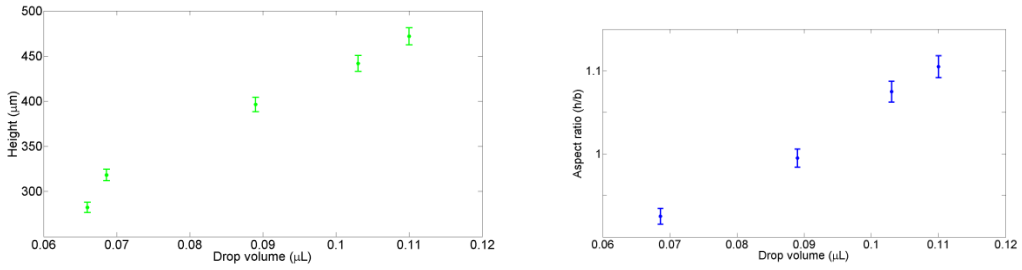


**Figure 5.7**: (a) Plot of microneedle height and (b) aspect ratio as a function of volume of the corresponding reservoir drops directly deposited onto a flat microscope substrate and obtained by thermal post fabrication treatment.

It was also seen that a mild thermal treatment (40 °C for 10 min) before complete solvent removal from microneedle induces a shrinkage that leads to an improvement of the aspect

ratio. In **Figure 5.8** the post-treatment needle profile (black) is overlapped to the original one (light gray).


**Figure 5.8**: Schematic of the thermal treatment and side view of needle before (light gray) and after the thermal treatment.

An alternative configuration was implemented in order to obtain a more controlled fabrication of arrays of microneedles by the pyro approach. An array of micropillars in PDMS was used as a multiple base to improve the uniformity of the base drops and consequently that of the microneedles. **Figure 5.9** shows the side view of the microneedle while being drawn from the micropillar-based reservoir. In this case the microneedles had heights in the range of 400 µm < $h$ < 800 µm, for base drops of 0.3 µl < V < 1.8 µl. Thanks to the use of PDMS pillars, the density of microneedles per area can be dictated by the distance between pillars; therefore, it can be easily controlled. Alternatively, using the this method it would be possible to control the period of spacing controlling the self-assembly of a highly viscous polymer[22] leading to the fabrication of a tightly spaced microneedle array.

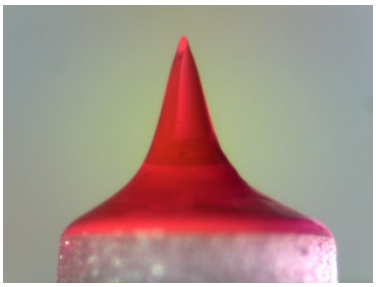

**Figure 5.9**: magnified and fluorescence image of one electro-drawn microneedle onto a polymer micropillar.

Since most of the therapeutics of interest are hydrophilic, we have adapted our technique to encapsulate any kind of hydrophilic compound in the microneedle. To this end, the PLGA solution was mixed with a water solution containing HSA labeled with Rhodamine 6G used as probe, to create a water in oil emulsion. The emulsion was then successfully electro-drawn to generate a needle with embossed protein loaded microcavities (**Figure 5.10**).

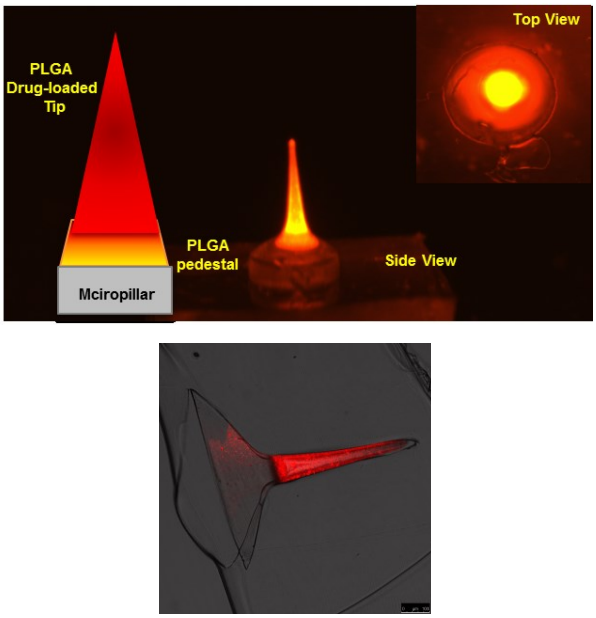


**Figure 5.10**: Fluorescence optical microscopy image of a microneedle produced by overlapping an emulsion drop loaded with rhodamine labeled HAS onto a first drop of pure PLGA solution. The fluorescene image of the side view is compared with a schematic to better explain the needle composition. The pure PLGA solution is used for the fabrication of the pedestal, while the cone is formed from the emulsion drop deposited in a second step over the pure PLGA reservoir; Optical confocal image of a slice of the microneedle produced using an emulsion drop loaded with rhodamine labeled HAS onto a first drop of pure PLGA solution.

Microneedle structure and dye distribution are clearly shown by the optical stereo microscope analysis. The dimension and the extension of these hydrophilic compartments appearing as insulated micrometric pores can be tuned by the composition and distribution of water droplet within the original emulsion. Micrometric porosity within the needle structure also affects PLGA degradation rate and thus the drug release kinetics. Therefore, it may be possible to tune the drug release profile by tailoring the porous microstructure by adapting the emulsification conditions[28].

The microneedles described so far present a not optimal distribution of bioactive agent. To improve the drug distribution within the needle regions, we succeeded in loading only the cone of the microneedle by using a two-stage dispensing procedure. A small drug-containg water-in-oil emulsion drop, corresponding to the volume of the needle's cone, was dispensed on the top of a drop of drug-free PLGA solution. The resulting composite drop was successfully electro-drawn to obtain a needle with drug-encapsulated porous cone and a compact drug free pedestal. The separation of the two regions, cone and pedestal, is even more evident by the confocal optical analysis reported in Figure 10.

A slight evolution of the two-stage dispensing procedure could also allow for the implanting the microneedle cones in the tissue with possible immediate patch removal by introducing a

separating and fast degradable layer between the two drops; the microneedle could then be inserted into the skin layer with rapid degradation of the interface layer[28]. Doing so, the pedestal may be separated from the drug-loaded microneedle cone leaving it inserted in the skin when a long dissolving time is required.

### 5.3 Skin indentation by PLGA electro-drawn microneedles

To serve as substitute for a hypodermic needle, a microneedle should penetrate the 10 ÷ 20 μm thick stratum corneum without breakage. A special cuff was designed, able to accommodate the flexible strip of microneedles, as shown in **Figure 5.11**. Preliminary indentation experiments were performed into model materials, such as wax and agarose gel in order to test the hardness of the microneedles[29]. **Figure 5.12** a-b show the microneedles while penetrating the agarose and just after ejection, respectively, where the transparency of agarose allows one to view the integrity of the microneedles in both cases. The results show that they can penetrate agarose at a depth of about 400 μm. Then, indentation experiments were performed into real skin by inserting the Nile Red-loaded microneedles, with an aspect-ratio of 1.25 obtained with post-thermal treatment, into pig cadaver skin and by removing them after 15 min. The indentation was performed by tightening the microneedle-loaded cuff onto the skin previously stretched onto a cylindrical support for the pig skin to emulate real conditions of use.

**Figure 5.11** : Tightening the microneedle-loaded cuff onto the skin.

The pressure exerted by tightening the cuff was measured by introducing a pressure sensor (CZN-CP1, TME electronic components) between the cuff and the flexible layer supporting microneedles. Specifically, the necessary pressure to produce the indentation was of around 0.01 N per microneedle which is lower than reported in literature (~0.04 N) maybe due to the high aspect-ratio of our post-thermal treated needles. The effectiveness of the indentation is confirmed by the cross sectional image of the stained skin at the site of microneedle

penetration, **Figure 5.13**. The dermis was clearly reached by the microneedle, thus confirming the potential use for drug delivery[28].

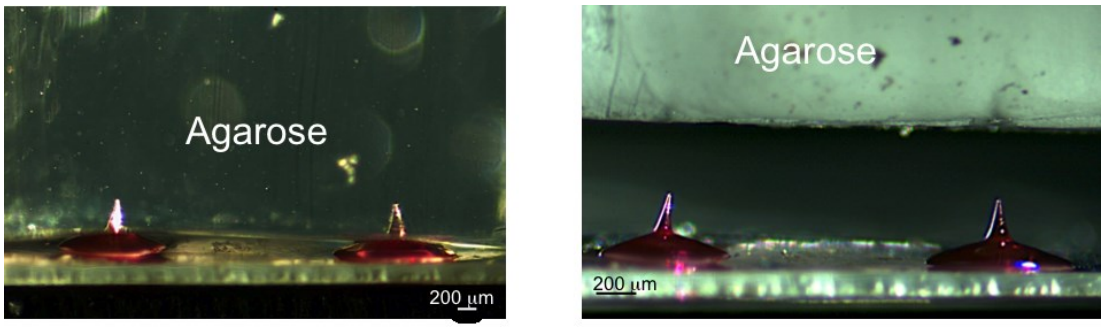


**Figure** 5.**12** : (a) Indentation test of microneedles in the agarose gel used as model material and (b) visualization of the integrity of the microneedles just after penetration, the microneedle on the left side appears as slightly bending with respect to the central axis before and after insertion.

Microneedle insertion depth was approximately 400 µm, which is in agreement with the dimensions of the microneedles. After indentation, microneedles were removed and the skin was fixed in a solution of 10 % neutral buffered formaline for 24 h, dehydrated in an incremental series of alcohol (75 %, 85 %, 95 % and 100 %, and 100 % again, each step 20 min at room temperature) treated with xylene and then embedded in paraffin. Successively, samples were sectioned at thickness of 6 µm, and stained with hematoxylin and eosin, and finally the sections were mounted with Histomount Mounting Solution (INVITROGEN) on coverslips and the morphological features of constructs were observed with a light microscope (BX53; Olympus).

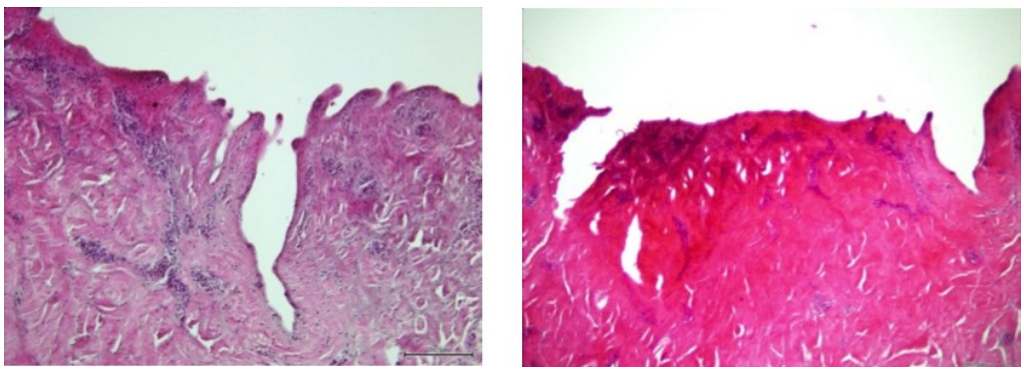

**Figure 5.13** : Cross-sectional image of the skin after microneedle removal and skin fixing in formaline at 10 % wt for evidencing the indented areas (scale bar 200 µm).

It is important to note here that the technological simplicity of the technique would provide a significant breakthrough in the clinical development of the biodegradable microneedles.

In summary, this section presents an electro-drawing (ED) approach based on the pyro-electric effect for the fabrication of sharp, dissolving microneedles directly from a liquid polymer reservoir, in a moulding-free and contact-free modality. Model drugs can be embedded at room temperature in drop reservoirs, drawn to form microneedles at no more than 40 °C and successfully delivered via indentation into the skin. In principle, nanoparticles of hydrogel could be previously dispersed in the polymer solution thus creating hydrophilic compartments and controlling the microneedle biodegradation kinetics.

Microneedle patches are formed directly onto a flexible, disposable strip that is inserted into a cuff, overcoming the technological limitations of both micro-casting and drawing lithography and opening new frontiers in the field of transdermal delivery.

## References


[1] A. Arora, M. R. Prausnitz, S. Mitragotri, *Int J Pharm,* **2008,** *364*(2), 227-236.

[2] W. C. Weldon, M. P. Martin, V. Zarnitsyn, B. Wang, D. Koutsonanos, I. Skountzou, M. R. Prausnitz and R. W. Compans, *Clin. Vaccine Immunol*., **2011**, *18*, 647-654.

[3] S. H. Bariya, M. C. Gohel, T. A. Mehta and O. P. Sharma, *J. Pharm. Pharmacol.*, **2012**, *64*, 11-29.

[4] G. Widera, J. Johnson, L. Kim, L. Libiran, K. Nyam, P. E. Daddona, M. Cormier, *Vaccine*, **2006**, *24*, 1653-1664.

[5] J. Hadgraft, M. E. Lane, *Phys. Chem. Chem. Phys.*, **2011**, *13*, 5215-5222.

[6] Q. Zhu, V. G. Zarnitsyn, L. Ye, Z. Wen, Y. Gao, L. Pan, I. Skountzou, H. S. Gill, M. R. Prausnitz, C. Yang and R. W. Compans, *PNAS*, **2009** 12, *106*(19), 7968-7973.

[7] G. Li, A. Badkar, S. Nema, C. S. Kolli, A. K. Banga, *Int J Pharm*, **2009**, *368*, 109-115.

[8] Y. C. Kim, F. S. Quan, R. W. Compans, S. M. Kang, M. R. Prausnitz, *Pharm. Res.*, **2011**, *28*, 135-144.

[9] J. Gupta, H. S. Gill, S. N. Andrews, M. R. Prausnitz, *J. Controlled Release, **2011**, 154*, 148-155.

[10] M. R. Prausnitz, *Adv. Drug Delivery Rev.,* **2004**, *56*, 581-587.

[11] C. Baek, M. R. Han, J. Min, M. R. Prausnitz, J-H. Park, J. H. Park, *J. Controlled Release* **2011**, *154*, 138-147.

[12] J-H. Park, M. G. Allen, M. R. Prausnitz, *J. Controlled Release,* **2005***, 104*, 51-66.

[13] J. W. Lee, J-H. Park, M. R. Prausnitz, *Biomaterials*, **2008**, *29*, 2113-2124.

[14] S. P. Sullivan, N. Murthy, M. R. Prausnitz, *Adv. Mat*., **2008**, *20*, 933-938.

[15] L. Y. Chu, M. R. Prausnitz, *J. Controlled Release,* **2011**, *149*, 242-249.

[16] S. D. Gittard, A. Ovsianikov, N. A. Monteiro-Riviere, J. Lusk, P. Morel, P. Minghetti, C. Lenardi, B. N. Chichkov and R. J. Narayan, *J. Diabetes Sci. Tec.,* **2009**, *3*, 304-311.

[17] S. P. Davis, B. J. Landis, Z. H. Adams, M. G. Allen, M. R. Prausnitz, *J. Biomec.* **2004,** *37*(8), 1155-1163.

[18] K. Lee, H. Jung, *Biomaterials*, **2012**, *33*, 7309-7326.

[19] K. Lee, H. C. Lee, D-S. Lee, H. Jung, *Adv. Mater.,* **2010**, *22*, 483-486.

[20] K. Lee, J. D. Kim, C. Y. Lee, S. Her, H. Jung, *Biomaterials,* **2011**, *32*, 7705-7710.

[21] C. K. Choi, J. B. Kim, E. H. Jang, Y-N. Youn, W. H. Ryu, *Small*, **2012**, *8*, 2483-2488.

[22] P. Ferraro, S. Coppola, S. Grilli, M. Paturzo, V. Vespini, *Nat. Nanotechnol.,* **2010**, *5*, 429-435.

[23] S. Grilli, S. Coppola, V. Vespini, F. Merola, A. Finizio, and P. Ferraro, *PNAS,* **2011**, *108*(37), 15106-15111.

[24] S. Coppola, V. Vespini, S. Grilli and P. Ferraro, *Lab Chip,* **2011**, *11*, 3294-3298.

[25] J. U. Park, M. Hardy, S. J. Kang, K. Barton, K. Adair, D. K. Mukhopadhyay, C. Y. Lee, M. S. Strano, A. G. Alleyne, J. G. Georgiadis, P. M. Ferreira, and J. A. Rogers, *Nat. Mater.,* **2007**, *6*, 781-789.

[26] B. de Heij, M. Daub, O. Gutmann, R. Niekrawietz, H. Sandmaier, R. Zengerle, *Anal. Bioanal. Chem.,* **2004**, *378*, 119-122.

[27] M. Y. Kim, B. Jung, J.- H. Park, *Biomaterials*, **2012**, *33*, 668-678.

[28] L. Y. Chu, S-O. Choi, M. R. Prausnitz, *J. Pharm. Sci.,* **2010***, 99*(10), 4228-4238.

[29] A. Arora, I. Hakim, J. Baxter, R. Rathnasingham, R. Srinivasan, D. A. Fletcher, S. Mitragotri, *PNAS,* **2007**, *104*, 4255-4260.

## Conclusion and perspectives

In summary, the work and the experiments described in this thesis are related to the description of an unusual and smart way for the manipulation of liquid and polymeric materials. In fact, the term "pyro-fluidic platform" would express the ability of working on fluids (liquid and/or polymer) exploiting the pyro-electric effect activated onto a ferroelectric crystal. A wide variety of functionalities of the pyro-electrohydrodynamic platform, such as droplet self -assembling and dispensing, have been described for manipulating multiphase liquids at micro as well as nanoscale.

The ability of manipulating materials is deeply described in the different chapters. We start describing the no-contact self-assembling of liquids in plane (1D), using a micro engineered crystal. Then additional degrees of freedom are added improving the dispensing capability and the smart transfer of material between two different planes (2D). Finally the controlling and fabrication of three-dimensional structures (3D) is presented. In every chapter the description of the properties of interest is exanimated and experimental characterizations are presented. In the recent years in many biological and biotechnological applications much research activity has been directed towards the development of miniaturized instrumentations with the aim at fabricating highly integrated and automated '*lab-on-a-chip*' systems based on microfluidics. This pyro-platform offers the great advantage of make possible the actuation of liquids in contact with a polar dielectric crystal through an electrode-less configuration. In particular, the method exploits the pyroelectric effect induced onto Lithium Niobate (LN) or Lithium Tantalate (LT) crystals. Pyro-self-assembling of polymer material for patterning single or array of microlenses (1D) appears to exhibit various differences and advantages compared to the conventional lithography techniques. In fact, the simplicity of the method proposed associated with the flexibility of the process for fabricating 3D polymer microstructures demonstrates the great potentiality of the pyro-platform functionalities exploitable in many fields, from optics to biosensing. In particular, the manipulation of polymer in combination with the high resolution of the pyro dispensing (2D) at nanoscale suggests different innovative and potential uses for in situ and non-invasive instruments, potentially useful for different kinds of lab-on-chip applications. The versatility of the pyroelectric approach could be also addressed to system of ink-jet printing, in fact, the simplicity afforded by the absence of nozzles, electrodes or high-voltage power supplies, and the potential for high-speed printing collectively make the method very attractive for many applications. Opportunities for future work seem to lie in developing methods for optimizing

the thermal diffusion and related processes that determine the upper limits in patterning. As an alternative to pyroelectrics for generating local fields, one could also consider programmable arrays of patterned electrodes or scanning metal probes as routes to virtual nozzles. Pursuing these possibilities, exploring advanced inks and exploiting the capabilities for applications in biology, printed electronics and related areas represent promising directions for further research. In particular, adding the possibility of manipulating polymers, different examples and fabrication of micro-structures are described in this thesis work. In fact, the pyro-platform could be applied to different kind of materials: from liquid to high viscous materials with a lot of possible applications in different fields of interest from photonics to biomedical ones. In fact, nanoliquid instabilities could be "fluidynamically" designed a priori with the aim of fabricating even complex shapes exploitable in many fields of technology. In particular, the fabrication of optically active elements, such as nanodroplets, microlenses and microstructures is described with different fields of application in photonics.

Moreover the possibility of manipulating the samples of interest in a touch-less modality is very attractive in the field of biological and chemical assays. In fact, when compared to traditional batch reactions, such system could offer many advantages. In fact, at present, most microfluidic technologies consist of micro-channels where liquids are manipulated by changing pressures or electrode voltages but such systems suffer from different drawbacks such as complex fabrication, sample cross-contamination, high voltage or pressure requirements. In this framework, the pyro-platform could be used also as a pioneering portable instrument for biosensing application.

Furthermore the fabrication of smart and personalized materials for biomedical applications requires the ability of high precision "on-demand" material dispensing. In order to satisfy this claim the multi purposed properties of the pyrofluidic platform are described and applied for processing biomaterials. We could move behind the studies developed about the manipulation of polymer for the fabrication of three-dimensional structures and apply the properties of the pyro-platform in case of polymer biocompatible and biodegradable. In fact, the design and fabrication of micro and nanostructures is of crucial importance in different areas of tissue engineering because of their inherent biodegradability, biocompatibility and biofunctionality. Controlling the structures and making possible the functionalization of biomaterials could allow their application for controlling cell adhesion and morphology on surfaces of synthetic materials for scaffold for tissue engineering.

All the properties described for the pyro-platform could open new routes for high resolution printing and patterning application from nanotechnology, sensing, biomedical and

biophotonics applications. In fact, manipulating polymers could allow the fabrication of micro-elements for lab-on-chip devices. Overall this micro components could be optically functionalized representing a cutting hedge technology for nanobiotechnology studies. In fact, besides controlling cells growth and fate, smart micro-elements could deliver optical stimuli from and to cells monitoring their growth in real time. All the characteristics described for the proposed platform open interesting perspectives for the realization of optically active scaffolds made of nanoengineered functional elements. The innovative aspect of this study suggests itself as an alternative powerful tool for the fabrication of active and smart materials opening the way to fascinating optogenesys studies.

**Annex #1**

We simulated the temperature variation in a Lithium Niobate crystal (LN) by a finite element method, considering two different kind of heat source.

The heat equation used in the numerical model is:

$$\rho C \frac{\partial T}{\partial t} - \nabla \bullet K \nabla T = S(r,t) \tag{1}$$

where ρ is the mass density, C the specific heat, K the thermal conductivity and S is the heat source.

In the first studied case the LN crystal is warmed using an heated tip which temperature is T=373,15 K and assumed to be constant.

For this configuration we apply the following boundary condition:

$\vec{n} \bullet K \nabla T = 0$ (Neumann condition on the upper and the lower LN boundaries)

where **n** is the inward normal to the boundary.

T = 298,15 K (Dirichlet initial condition on the LN boundaries)

T = 373,15K (Dirichlet condition on all the tip boundaries that we assume to have a constant temperature).

As to the source term S, we calculated the black body radiation produced by the iron tip at T=373.15K that resulted to be negligible. Therefore the heating of the LN crystal takes place only by contact with the heated-tip.

In Figure 1 is shown the surface temperature map at time T=10 s.

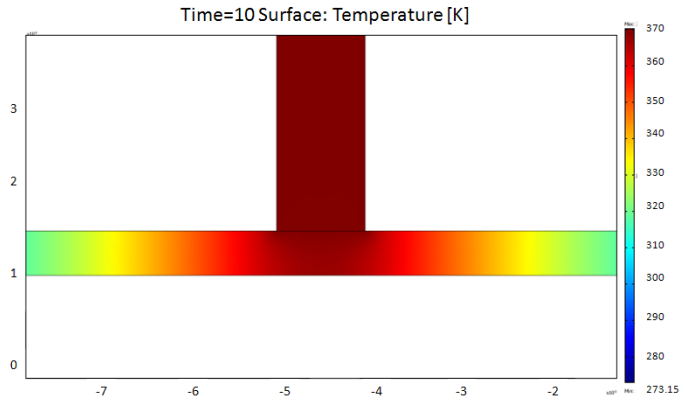


**Figure 1**

In the second configuration we heated the LN crystal by means of a $CO_2$ laser beam.

In this case the source term is $S(r,t)=\frac{P(1-R)\alpha}{\pi\omega^2}\exp\left[-\frac{2x^2}{\omega^2}\right]\exp[-\alpha y]$

where P is the incident optical power, ω is the beam waist and R is the intensity reflectivity and $\alpha = 6.3 \times 10^4\ m^{-1}$ is the absorption coefficient at wavelength λ=10microns.

Moreover, we impose the Neumann boundary condition $\vec{n} \bullet K\nabla T = 0$ on all LN boundaries.

We simulate the heat propagation in the LN substrate and in Figure 2 we show the surface temperature map obtained.

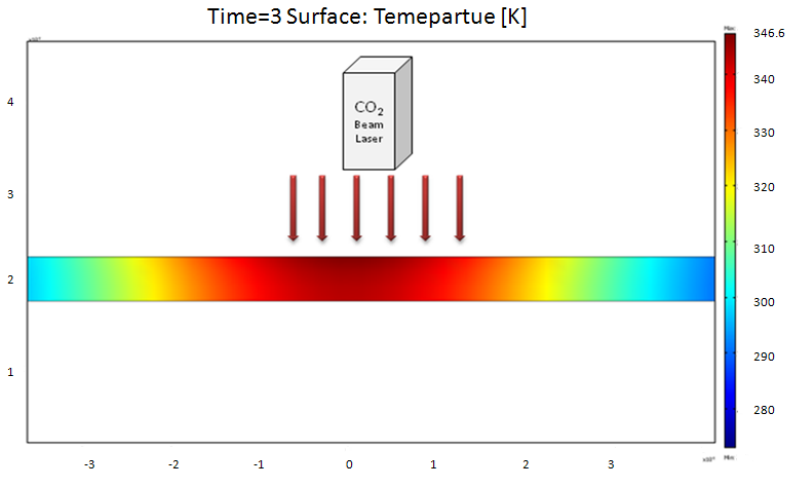


**Figure 2**

The use of a laser beam as heating source involves some advantages. The system is more flexible, rapid scan and remote supplying of energy in non-contact mode favours more efficient and non-invasive heat-transfer. In fact, we can finely control its beam waist and its power and therefore the heated area of the sample and the temperature value. Moreover this kind of source allows a no-contact heating avoiding eventual sample damages.

Using a laser beam as heating source we also simulated the electric potential and the electric field norm plots.

In figure 3 is shown the electric potential, the maximum value reached is $1{,}016*10^4$ V.

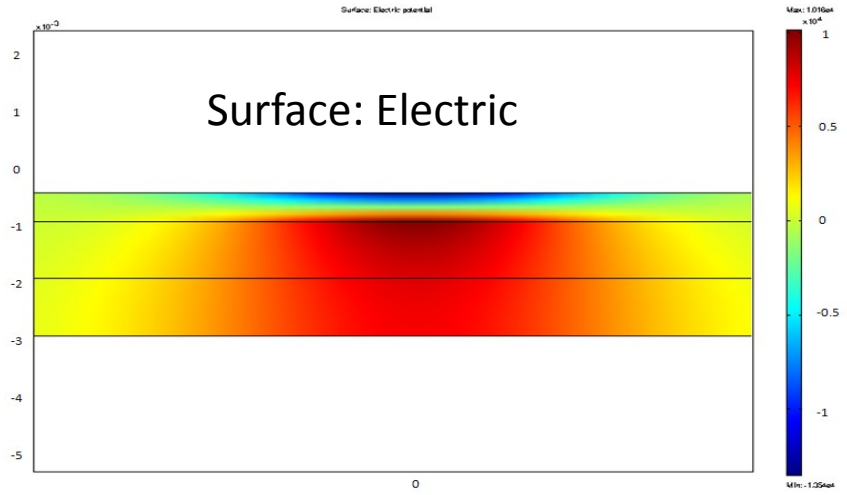


**Figure 3**

In figure 4 is shown the electric field norm, the maximum value reached in this case in the centre of the crystal is $4.01*10^7$ V/m.

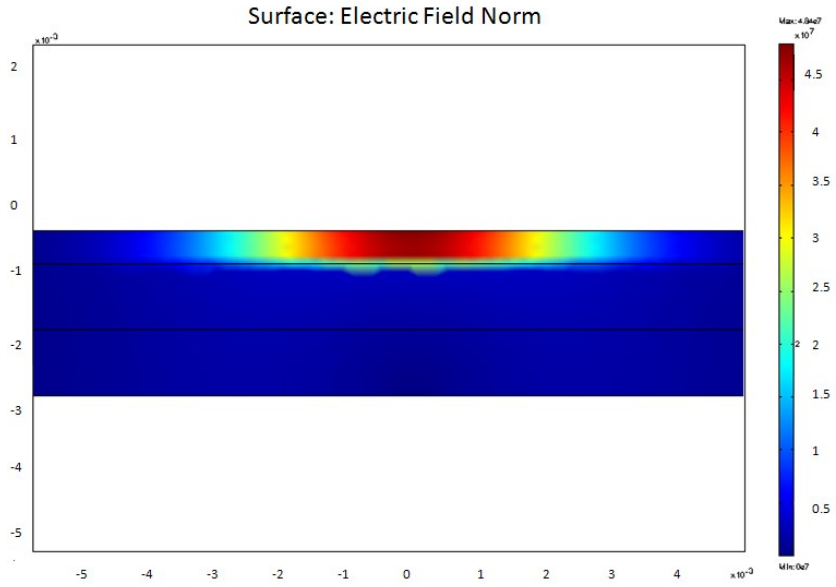


**Figure 4**

The value of the electric field measured in our case is comparable with those obtained in other experiments in which an electrostatic field induces inkjet printing based on an electrohydrodynamic process (see table below).

Of course more sophisticated theoretical modelling would be necessary to afford the non-stationary dynamic in the thermal process.

| METHOD | ELECTRIC FIELD |
|---|---|
| Drop-on-demand printing (ref.1) | 1.05 kV/mm |
| Electrohydrodynamic jet printing (ref.2) | 9 kV/mm |
| Drop formation in electric field (ref.3) | 24 kV (thickness is not specified) |

[1] Choi, J. et al. Drop-on-demand printing of conductive ink by electrostatic field induced inkjet head. *Appl. Phys. Lett.* **93**, 193508 (2008).

[2] Park, J.U. et al. High-resolution electrohydrodynamic jet printing. *Nat. Mater*. **6**, 782-789 (2007).

[3] Notz, P.K. & Basaran, O.A. Dynamics of drop formation in an electric field. *Journal of Colloid and Interface Science* **213**, 218-237 (1999).

**Anne#2: Characterization of the pyroelectrodynamic dispenser for different liquids**

The characterization of the shooting process was performed by using the following test fluids giving significant variation in contact angle $\theta$ and viscosity $\eta$: carboxyl acid, almond oil, paraffin oil, water, cell cultivation medium**.** Table 1 shows the values of the measured contact angles $\theta$ and of the corresponding viscosities $\eta$ for the different test liquids.

| test liquid | $\theta$ (°) | $\eta$ (cP) |
|---|---|---|
| PDMS | 22 | 3900 |
| carboxyl acid | 26 | 8.2 |
| paraffin oil | 37 | 1.9 |
| almond oil | 40 | 1.4 |
| cell cultivation medium | 63 | N.A. |
| water | 75 | 1 |

Table 1

First of all the activation and deactivation *base-substrate* distances were evaluated for the different fluids by measuring the minimum value $D_{min}$ (activation) required to break the liquid bridge and therefore to switch on the shooting process and the maximum value $D_{max}$ (deactivation) over which the PEHD dispenser is off. The heating energy was kept constant. Fig.1a shows the resulting values as a function of the contact angle $\theta$, together with the operating range of distances $\Delta D = D_{max}$-$D_{min}$.

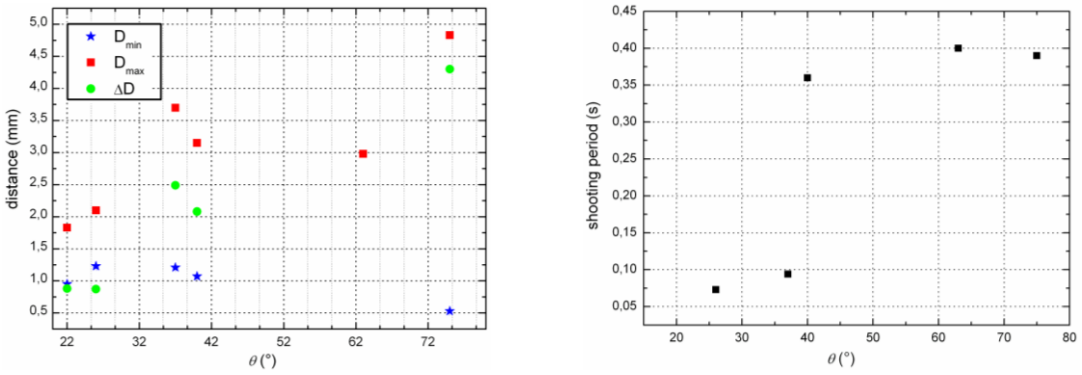


(a) (b)

Figure 1

The results show that basically the deactivation $D_{max}$ and the range distance $\Delta D$ increase with the contact angle. Conversely, the activation distance $D_{min}$ clearly appears to not

vary significantly for the different test liquids. These results show that the PEHD dispenser exhibits a reduced range of operation distances in case of fluids with higher viscosities. Another important feature of the PEHD dispenser is represented by the shooting period and Fig.1b shows the experimental results. The dispenser delivers droplets with higher frequency in case of fluids with higher viscosities. The scaling of the dispensed volume with the viscosity of the liquid was also measured for the three oils and Table 2 shows the corresponding experimental data.

| Test liquid | η (cP) | dispensed volume (nL) |
|---|---|---|
| Almond oil | 1,4 | 0,34 |
| Paraffin oil | 1,9 | 0,06 |
| Carboxyl acid | 8,2 | 0,02 |

Table 2

The volume of the drop reservoir was around 100 nL for each test oil and the volume of the dispensed droplet clearly decreases with increasing viscosity. For the sake of clarity, the different dynamics of the PEHD shooting for the three test liquids, captured by the CMOS camera, are shown in the Supplementary Movies 9, 10 and 11. It is important to note that EHD based liquid emissions have been deeply investigated theoretically for a wide variety of configurations (liquids flowing in capillary tubes or nozzles; tip streaming from liquid films; steady cone jets; coflowing liquids; etc.) [1-6] and different scaling laws have been proposed, even with reciprocal discrepancies. The dispenser proposed here is still based on EHD forces but it works under a completely different configuration based fundamentally on liquid emission from sessile drops through pyroelectric fields, so that a well established theory is currently not available.

**References**


1. Jaworeket, A. et al. Viscosity effect on Electrohydrodynamic (EHD) spraying of liquids. *Inst. Phys. Conf.* **163**, 109 (1999).

2. Calvo, A.M.G. On the general scaling theory for electrospraying. *J. Fluid. Mech.* **507**, 203 (2004).

3. Park, J-U. et al., High resolution electrohydrodynamic jet printing. *Nat. Mater.* **6**, 781 (2007).

4. Collins, R.T. et al., Electrohydrodynamic tip streaming and emission of charged drops from liquid cones. *Nature Physics* **4**, 149 (2008).

5. de la Mora, J.F. The fluid dynamics of Taylor cones. *Annu. Rev. Fluid. Mech*. **39**, 217 (2007).

6. Castro-Hernandez, E. et al., Scaling the drop size in coflow experiments. *New J. of Physics* **11**, 075021 (2009).